energies

MDPI

Review

Supercritical CO_2 Flow and Heat Transfer in Compact Thermal Systems: A Critical Review of Mechanisms, Geometries, and Enhancement Strategies

Abdulrahman Alenezi [1,*], Mohammad Ismail [2] and Jafar Masri [3]

[1] Department of Materials Science and Engineering, Abdullah Al Salem University, Khaldiya 72303, Kuwait
[2] Department of Renewable Energy Engineering, Amman Arab University, Amman P.O. Box 2234, Jordan; m.ismail@aau.edu.jo
[3] Department of Automotive Engineering, Palestine Technical University-Kadoorie, Tulkarm P.O. Box 7, Palestine; j.masri@ptuk.edu.ps
* Correspondence: abdulrahman.obaid@aasu.edu.kw

Abstract

Supercritical CO_2 (sCO_2) is a promising working fluid for compact thermal systems owing to its high heat transfer capability and advantageous thermophysical properties close to the pseudocritical region. However, strong property gradients in this regime give rise to complex thermo–hydraulic phenomena, comprising heat transfer deterioration (HTD), buoyancy-driven stratification, thermal acceleration, and flow instability, which restrict performance and predictive accuracy. This review provides a mechanism-based and design-oriented overview of sCO_2 transport behaviour in compact configurations, for example, straight and curved tubes, micro/minichannels, printed circuit heat exchangers and enhanced passages. The analysis shows HTD results from the coupled effects of pseudo-boiling-like behaviour, buoyancy, and thermal acceleration, with their relative importance determined by geometry, heating distribution, and operating conditions. Comparative evaluation reveals that no single configuration is consistently optimal. Conversely, performance is defined by trade-offs between heat transfer enhancement, pressure-drop penalty, and thermal uniformity. Advanced geometries and passive enhancement techniques improve mixing and suppress stratification, whilst often increasing hydraulic resistance and sensitivity to flow maldistribution. Moreover, the review identifies limitations in the transferability of predictive correlations across fluids, geometries and heating conditions, emphasising the need to respect their calibration ranges. The findings underline the need for geometry-aware, heating-aware, and mechanism-based predictive models, in conjunction with integrated design approaches that combine local enhancement, flow distribution, and system-level stability. The results provide an integrated framework connecting transport mechanisms, compact-channel design, and system performance, proposing guidance for the development of efficient and stable sCO_2 thermal systems.

Keywords: supercritical carbon dioxide (sCO_2); mini/microchannels; printed circuit heat exchangers (PCHEs); heat transfer deterioration; pseudo-boiling; flow instability

Academic Editor: Jan Taler

Received: 30 September 2026
Revised: 2 November 2026
Accepted: 6 November 2026
Published: 9 November 2026

Copyright: © 2026 by the authors. Licensee MDPI, Basel, Switzerland. This article is an open access article distributed under the terms and conditions of the Creative Commons Attribution (CC BY) license.

1. Introduction

In advanced thermal systems, supercritical carbon dioxide (sCO_2) is considered one of the most effective working fluids owing to its advantageous thermophysical properties near and above the critical point (31.1 °C and 7.38 MPa). In the supercritical region, CO_2 exhibits liquid-like density and gas-like diffusivity and viscosity, whereas its specific heat, density, thermal conductivity, and expansivity experience significant changes close to the pseudo-critical temperature. These properties enable high heat transfer coefficients (h) and significant reductions in component size, leading to the increased use of sCO_2 in compact and high-performance thermal systems [1,2]. Moreover, CO_2 is non-flammable, non-toxic, abundant, relatively inexpensive, and environmentally friendly compared with most conventional working fluids, which makes it even more suitable for sustainable energy and cooling solutions [3]. Recent studies discuss urban energy resilience and national pathways toward energy transition and emissions reduction [4,5]. Within compact thermal systems, including mini/microchannels and printed circuit heat exchangers (PCHEs), steep property gradients and geometric confinement complicate sCO_2 flow, heat transfer, and stability.

In recent years, sCO_2 has become increasingly important in various engineering fields. It forms the basis of high-efficiency sCO_2 Brayton cycles that can achieve high thermal efficiencies with smaller turbomachinery and a smaller system footprint compared with conventional steam-based systems in power generation systems [6]. In addition to power cycles, sCO_2 has been extensively studied in nuclear energy systems, concentrated solar thermal systems, waste heat recovery facilities, and geothermal applications, where its advantageous thermophysical properties and size can deliver significant performance benefits [7]. Regenerative cooling has also been proposed for aerospace and propulsion applications under high heat flux conditions (q″), owing to the high specific heat capacity of sCO_2 near the pseudo-critical region [8]. At smaller scales, sCO_2-based mini and microchannel heat exchangers, compact coolers, and heat sinks provide new opportunities for electronics cooling and other q″ cooling applications, where a balance between thermal performance and geometric size is essential [9].

Nonetheless, the flow and heat transfer behaviour of sCO_2 are extremely complex and significantly influenced by operating conditions, heating mode, and channel geometry. The same steep property gradients that increase heat transfer can also induce undesirable transport processes to occur when the bulk or wall temperature is close to the pseudo-critical region. The most significant of these is heat transfer deterioration (HTD), traditionally associated with a sudden increase in wall temperature, suppression of near-wall turbulence, buoyancy-induced stratification, and the effects of thermal acceleration [10,11]. These mechanisms are of particular concern in upward and horizontal flows, as well as in non-uniformly heated channels, where local variations in density and specific heat can significantly alter the velocity and temperature fields. Moreover, pseudo-boiling-like behaviour, flow oscillations, etc., can also adversely impact thermal performance and operational reliability. This denotes that predictive correlations that are established at simpler conditions tend to be inaccurate when used on compact passages, non-uniform heating, or improved channel shapes. Consequently, there is a need for more robust mechanistic and data-based tools that can predict the effects of buoyancy, acceleration, and pseudo-critical behaviour [12–14].

These challenges have prompted a sizable body of both experimental and numerical simulation and, more recently, the development of machine-learning-assisted predictive work. Current research investigates the effect of channel size, cross-sectional shape, wall-heating configuration, flow direction, inserts, ribs, pin fins, lattice structures, and manifold design on heat transfer, temperature uniformity, and flow stability. Particular focus has been on mini/microchannel heat sinks and PCHEs, where compactness, thermal resistance,

and pressure drop (ΔP) requirements must be carefully considered. At the same time, new geometries, including zigzag, wavy, airfoil-shaped, tapered, ribbed, and additively manufactured passages have been suggested to enhance mixing, suppress thermal stratification and HTD, and improve temperature uniformity under challenging operating conditions [15–17].

Previous reviews have established substantial knowledge of HTD, pseudo-boiling, flow instability, and PCHE performance [18–23]. In this respect, the current review addresses a specialised research gap by focusing specifically on sCO_2 in compact thermal systems, straight and curved tubes, mini and microchannels, PCHE passages, passive enhancement structures, and related compact thermal structures. The review not only provides a summary of the recent experimental and numerical results, but also links pseudo-boiling, buoyancy, thermal acceleration, geometry-induced secondary flow, and non-uniform heating to their effects on wall temperature excursion, ΔP penalty, HTD, and flow instability. Similarly, it critically evaluates the applicability and shortcomings of current correlations and identifies the relationships between channel geometry, heating conditions, and enhancement strategies in determining practical thermo–hydraulic performance. Table 1 summarises this positioning, and Figure 1 outlines the review's scope.

Two questions organise the review: How do operating conditions and passage features modify the mechanisms governing local heat transfer and HTD, and what evidence supports transferring performance results and predictive models between configurations? Geometry, enhancement, and instability studies are examined through these questions, with design implications restricted to the conditions supported by the reviewed evidence.

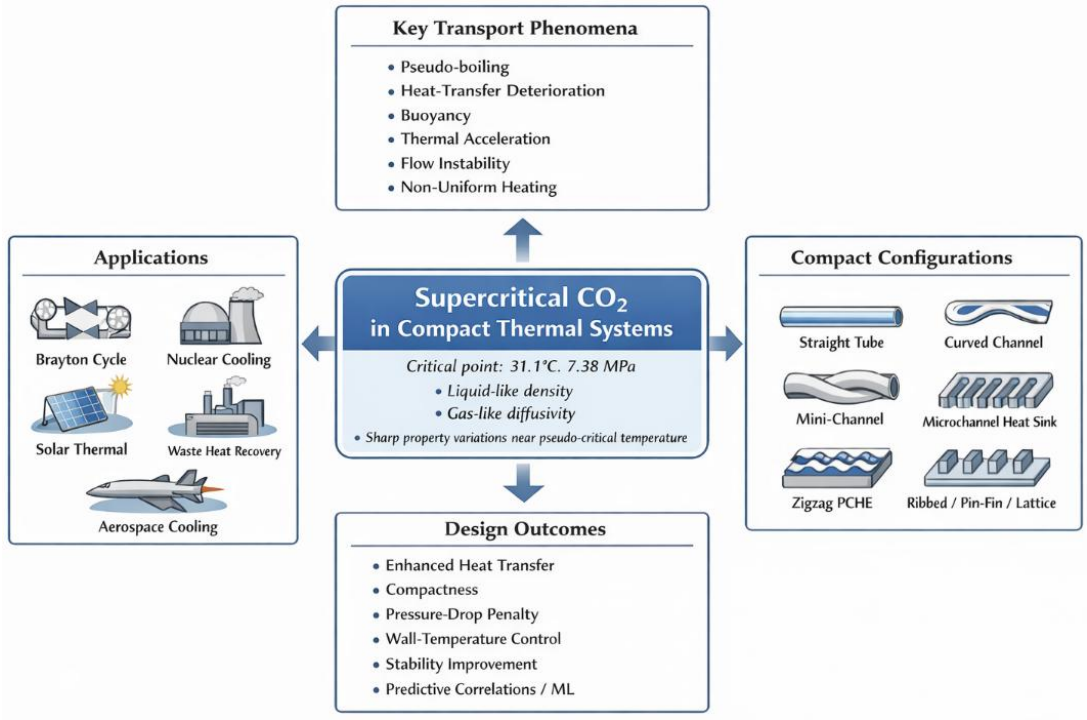


Figure 1. Compact thermal systems for sCO_2: applications, transport mechanisms, challenges, and design strategies.

Table 1. Positioning of the present review relative to previous review papers.

Review Paper	Main Focus	CO_2-Specific	Compact Geometries/Scales Considered	Hydraulic-Scale or Compactness Taxonomy	Mechanism Treatment	Quantitative Synthesis/Design Metrics	Correlation Benchmarking	Gap Addressed by the Current Review
[18]	HTD mechanisms and mitigation strategies in sCO_2	Yes	Mainly tubes; limited compact-channel comparison	Limited	Comprehensive assessment of HTD, buoyancy, acceleration, and mitigation	Limited coverage; predominantly mechanism- and condition-based discussion	Limited coverage; fails to provide a broad compact-geometry correlation assessment	Extends HTD discussion from mainly tube-based behaviour to compact passages, micro/minichannels, PCHEs, and passive enhancement structures
[19]	Flow-instability mechanisms, instability types, methods and future directions at supercritical pressure	No	Broad supercritical-fluid systems; limited focus on compact sCO_2 geometries	No	Extensive coverage of flow instability, but not specific to compact sCO_2 heat exchangers	Limited coverage for geometry-level thermal–hydraulic design	Limited coverage of compact sCO_2 heat transfer correlations	Links instability to compact sCO_2 passage design, HTD, geometry-induced maldistribution, and thermo–hydraulic stability
[20]	Multiscale thermodynamics, pseudo-boiling, DNS, instability, and modelling in supercritical fluids	No	Moderate coverage of channels; limited PCHE and engineering design	Partial coverage, primarily physics-driven rather than compactness-driven	Detailed discussion of pseudo-boiling and supercritical-fluid physics	Limited design-oriented comparison among compact geometries	Limited coverage of engineering correlation ranges and compact-passage applicability	Separates pseudo-boiling-like interpretation from variable-property single-phase convection. Connects both to compact-channel design constraints
[21]	Thermal–hydraulic and dynamic behaviour of PCHEs in sCO_2 systems	Yes	Focus on PCHE; limited coverage of tubes, micro/minichannels and passive enhancement at different scales	Partial coverage; predominantly PCHE topology-based	Moderate-to-strong treatment of PCHE thermal–hydraulic behaviour	Partial coverage; mainly PCHE-specific performance comparison	Partial coverage; not a general compact-system correlation database	Positions PCHEs within a wider compact-system framework and compares them with tubes, micro/minichannels and enhanced passages
[22]	Thermal–hydraulic performance and optimisation of PCHEs in advanced nuclear systems	Yes	Considerable focus on PCHEs; application-specific to	Partial coverage; primarily PCHE design variables	Limited coverage of recent pseudo-boiling, HTD and passive	Partial coverage; mainly optimisation-oriented for a	Limited coverage of broad sCO_2 compact-system correlations	Broadens the discussion beyond nuclear PCHEs to multi-application compact systems, including electronics cooling, aerospace cooling, waste heat

			advanced nuclear systems		enhancement mechanisms	specific application		recovery, and Brayton-cycle components
[23]	PCHE fundamentals, passages, optimisation, and design for helium and sCO_2 Brayton cycles	No	In-depth focus on PCHEs and Brayton-cycle; limited discussion of mini/microchannels and HTD	Limited	Limited treatment of HTD, pseudo-boiling and instability	Partial coverage of PCHE design, limited for cross-geometry comparison	Limited coverage of recent compact sCO_2 correlation failures	Expands PCHE-focused knowledge with recent sCO_2-specific compact-passage studies, passive enhancement methods, HTD mechanisms and predictive-correlation limitations
Current review	sCO_2 flow, heat transfer, HTD, pseudo-boiling debate, instability, compact geometries, passive enhancement, and correlation limitations	Yes	Straight/curved tubes, tapered/profiled passages, micro/minichannels, PCHEs, heat sinks, ribs, pin fins, twisted tapes, lattice, and roughened passages	Yes; organises studies by hydraulic diameter, compactness and application domain	Mechanism-based; describes HTD as the coupled effects of property variation, pseudo-boiling-like behaviour, buoyancy, thermal acceleration, near-wall turbulence suppression, and non-uniform heating	Yes; uses heat transfer enhancement, ΔP penalty, f, thermal performance factor, pumping-power implications, compactness, and thermal uniformity	Evaluates correlation errors and applicability reported in published studies; no new benchmarking is performed.	Provides a design-oriented framework connecting hydraulic scale, geometry, transport mechanisms, operating conditions, correlation reliability, and application-specific design boundaries

The overlap shown in Table 1 reflects the shared physical foundations of these reviews. The present synthesis emphasises the conditions governing the transfer of evidence between passage configurations and applications. Quantitative results are interpreted against their original baselines and operating ranges, and correlation errors are treated as source-reported assessments. The review does not provide a new common-dataset correlation benchmark or establish universal performance rankings across heterogeneous studies.

2. Methodology and Literature Selection

The review was conducted using a structured literature identification, screening, eligibility assessment, and knowledge integration process. The aim was not only to obtain published studies related to sCO_2 heat transfer, but also to categorise existing knowledge with respect to hydraulic scale, compactness, geometry, predominant transport mechanism, application field, and thermo–hydraulic performance indicators. This was undertaken to avoid a conventional paper-by-paper review and to enable a more critical comparison of heat transfer enhancement, ΔP penalty, HTD, thermal uniformity, flow instability and predictive-correlation reliability for compact sCO_2 thermal systems.

The methodology was developed to address three main requirements. First, the search strategy, screening criteria, and limitations of the available screening records were described explicitly. Second, the retained studies were categorised in accordance with engineering-relevant parameters, for example D_h, compactness, mass flux (G), q″, operating pressure, heating mode, and application domain. Third, an integration process was required to enable subsequent quantitative comparisons of heat transfer enhancement, frictional losses or ΔP penalties, thermal performance factors, compactness-related metrics, pumping-power implications, and correlation error ranges.

2.1. Search Strategy and Databases

The reviewed literature includes publications from 2005–2026, together with earlier studies providing foundational correlations, benchmark experiments and theoretical interpretations relevant to sCO_2 heat transfer.

The search strategy combined terms related to working fluid, transport mechanisms, compact geometry, passive enhancement, predictive correlations and data-driven modelling. The main keyword groups consisted of "supercritical carbon dioxide," "sCO_2," "heat transfer," "convective heat transfer," "thermal transport," "heat-transfer deterioration," "HTD," "pseudo-critical," "pseudocritical," "pseudo-boiling," "buoyancy," "thermal acceleration," "mixed convection," "microchannel," "mini-channel," "compact channel," "printed circuit heat exchanger," "PCHE," "compact heat exchanger," "heat sink," "straight tube," "curved tube," "serpentine channel," "wavy channel," "zigzag channel," "airfoil channel," "ribbed channel," "pin fin," "twisted tape," "lattice," "roughness," "Nusselt number," "friction factor," "pressure drop," "correlation," "machine learning," "data-driven model," "hybrid modelling," and "surrogate model." These keyword groups were combined using Boolean operators such as AND and OR to identify studies related to sCO_2 heat transfer, HTD, compact passages, PCHEs, passive enhancement structures, predictive correlations, and ML-assisted modelling.

Citation tracking from recent reviews and key primary studies was also conducted to identify additional foundational or highly relevant papers that were not retrieved using the keyword search.

2.2. Screening and Eligibility Process

The literature identification process and screening are summarised in Figure 2. A preliminary search retrieved 520 records from Scopus, Web of Science, ScienceDirect, Google Scholar, and citation tracking. To begin with, these 520 records were screened by title and abstract to identify relevant studies relating to compact sCO_2 thermal systems, near-pseudocritical heat transfer, HTD, PCHEs, micro/minichannel transport, passive enhancement, predictive correlations, and machine-learning-based modelling.

After screening titles and abstracts, 270 records were excluded. The main reasons for exclusion were a lack of direct relevance to compact sCO_2 thermal systems, a focus on thermodynamic cycle-level analysis, subcritical-only CO_2 conditions, duplicate records,

or insufficient relevance to heat transfer and flow behaviour. This resulted in 250 full-text articles for detailed eligibility assessment.

The full-text eligibility assessment focused on articles that provided suitable thermo–hydraulic content, clearly defined geometries, properly documented operating conditions, mechanistic relevance, and quantitative transport results. A total of 72 articles were excluded at this stage owing to a lack of quantitative information, inadequate experimental or numerical validation, non-compact geometries, duplicate or incomplete reporting, or limited relevance to the mechanism–geometry–performance framework established in this review. The revised manuscript cites 177 references, including primary studies, reviews, and foundational sources.

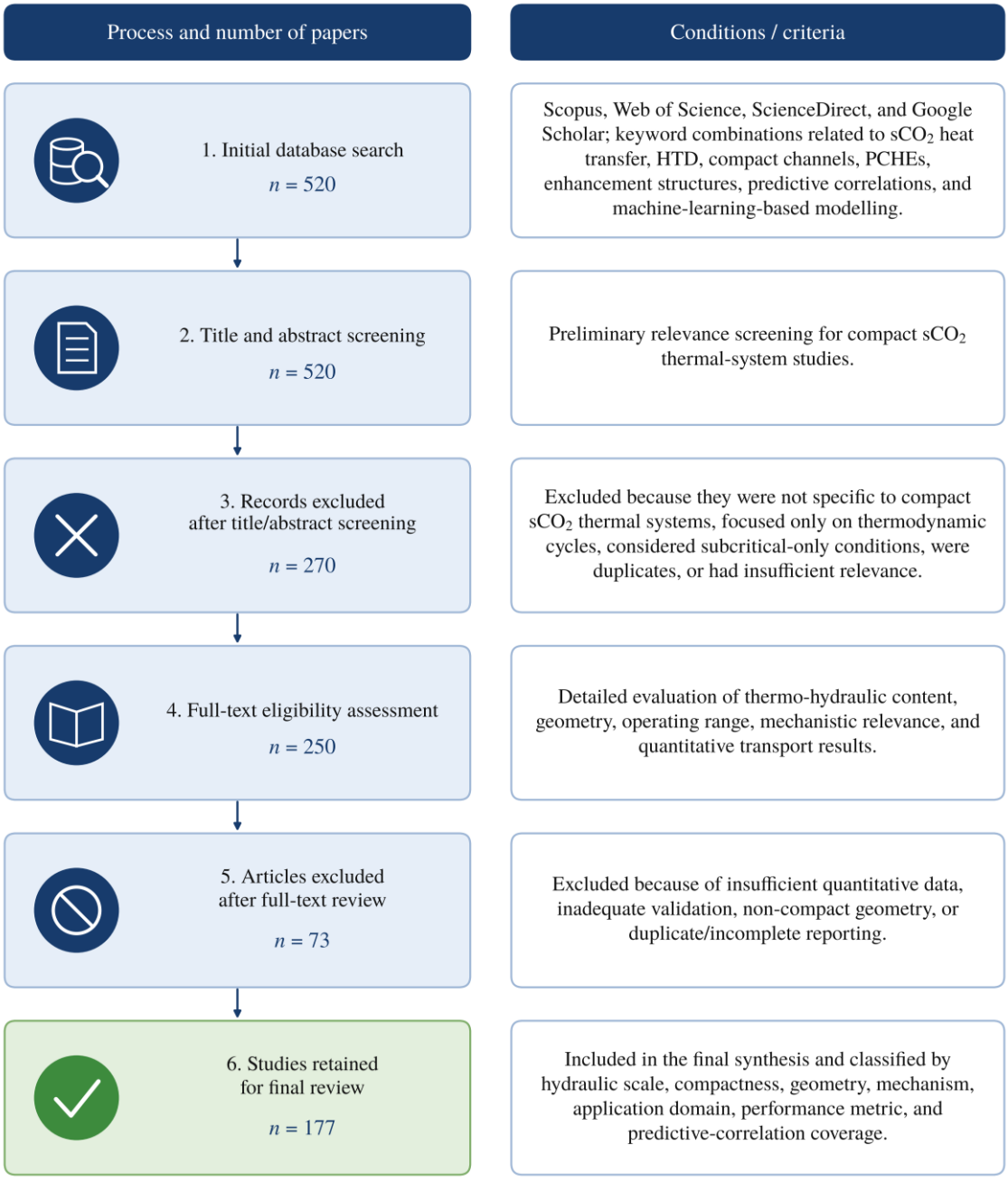


Figure 2. Literature identification, screening, eligibility assessment, and final study selection process employed in this review.

Although the review followed a structured literature selection process, complete historical database-specific search logs and separate exclusion counts for each reason could not be reconstructed. This limits the reproducibility of the search and screening process. The revised manuscript therefore distinguishes the 177 cited references from the studies contributing to quantitative comparisons and identifies the operating conditions and applicability limits of the evidence used.

2.3. Inclusion and Exclusion Criteria

The following criteria guided relevance screening. Studies used for quantitative comparisons also required clearly reported geometry, operating conditions, quantitative results, and adequate validation. Sources retained for background or mechanistic discussion were distinguished from those supporting quantitative comparisons. The exclusion criteria were applied according to the intended use of each source.

1. The study was conducted on heat transfer, ΔP, flow instability, pseudo-critical property effects, and HTD in sCO_2.

2. The study focused on compact or confined geometries, such as straight tubes, curved tubes, tapered passages, minichannels, microchannels, PCHEs, heat sinks, ribbed channels, pin-fin passages, twisted-tape inserts, lattice structures, roughened surfaces, or additively manufactured passages.

3. The study reported quantitative thermo–hydraulic information, such as the h, Nusselt number (Nu), f, ΔP, wall temperature distribution, thermal performance factor, pumping-power penalty, flow-instability threshold, or prediction error.

4. The study included experimental measurements, validated numerical simulations, semi-empirical correlations, or data-driven models relevant to sCO_2 transport.

5. The study contributed to the understanding of pseudo-critical property variation, pseudo-boiling-like behaviour, variable-property single-phase convection, buoyancy-induced stratification, thermal acceleration, near-wall turbulence suppression, secondary flows, flow maldistribution, and the effects of non-uniform heating.

Studies were excluded for the following reasons.

1. They investigated only subcritical CO_2 conditions;

2. Only system-level thermodynamic cycle analysis was considered (no discussion of transport processes);

3. They lacked quantitative heat transfer, ΔP, or instability data;

4. They failed to provide adequate information on geometry, operating conditions, and/or validation data;

5. They did not focus on compact thermal systems;

6. They contained data that had already been published in another, more comprehensive source;

7. They made general comments without making a technical or mechanistic contribution.

2.4. Quality Assessment and Bias Reduction

The methodological quality, relevance of the retained studies to compact sCO_2 thermal systems, and their suitability for comparative analysis were evaluated. Experimental studies were assessed based on test-section geometry definition, pressure and temperature control, G and q″ specification, wall temperature measurement, uncertainty analysis, repeatability, and reporting of local or average heat transfer data. The numerical studies were evaluated using mesh-independence analysis, justification of the turbulence model, treatment of thermophysical properties, definition of boundary conditions, comparison with experimental data, and reporting of prediction errors. The evaluation of correlation-development studies included the following: calibration

database, validity range, geometry type, pressure range, Reynolds number range (Re), G, q″, heating or cooling mode, and the reported deviation and applicability to compact or enhanced passages.

To reduce selection bias, the review did not depend on a single database, keyword, or geometry class. Moreover, citation tracking was employed, as it can uncover influential studies that might not be located using keyword-based searches. Studies were organised not by author or chronology but by hydraulic scale, geometry, mechanism, and application domain. To retain the original context of each study, differences in ΔP, G, q″, D_h, channel orientation, heating condition, and modelling method were retained. Consequently, this enabled the review to identify findings that are transferable throughout the physical space, from those that are specific to particular operating windows or application domains.

An attempt was made to avoid overgeneralisation. For instance, the superiority of any particular channel geometry, such as triangular, zigzag or airfoil-shaped channels, was determined only within the reported operating range and design objective. Likewise, pseudo-boiling-like behaviour was not considered the only explanation for HTD. Conversely, it was investigated in conjunction with variable-property single-phase convection, buoyancy-induced stratification, thermal acceleration and near-wall turbulence modification, and non-uniform heating.

The assessment informed how each study was used in the synthesis. Quantitative comparisons relied on studies with sufficiently reported geometry, operating conditions, validation, and performance definitions. Where these details were incomplete, findings were discussed qualitatively and were not used to establish numerical rankings or general design limits. Correlation calibration results were distinguished from independent validation, and steady-state results were not treated as evidence of dynamic stability.

2.5. Classification and Synthesis Framework

The reviewed literature was classified using separate descriptors for hydraulic scale, component architecture, passage geometry, and enhancement features. Hydraulic scale was defined using $D_h = 4\ Ac/Pw$, where Ac is the flow cross-sectional area, and Pw is the wetted perimeter. Following Kandlikar and Grande, microchannels have $10\ \mu m < D_h \leq 200\ \mu m$, minichannels have $200\ \mu m < D_h \leq 3$ mm, and conventional channels have $D_h > 3$ mm. These limits provide a consistent reporting convention rather than boundaries between dominant heat transfer mechanisms. Where an original study uses different terminology, its reported dimensions govern the classification adopted here [24].

Component architecture was recorded separately, including individual tubes, multichannel heat sinks and PCHEs. Passage geometry describes cross-sectional shape, curvature, and area variation, while enhancement features include ribs, pin fins, twisted tapes, lattices, and surface roughness. These descriptors can coexist: a PCHE may contain minichannels with zigzag geometry or enhanced surfaces. Flow orientation and heating distribution were recorded as operating descriptors.

Compactness was assessed separately through heat transfer surface area density, Aht/Vcore, with the fluid side and core-volume basis specified wherever available. When the source does not report sufficient geometric information, compactness remains unquantified rather than inferred from the component name. Large-diameter tubes and non-compact configurations were retained as mechanistic reference cases; their inclusion does not classify them as compact devices.

The studies were categorised into pseudo-critical property variation, pseudo-boiling-like behaviour, variable-property single-phase convection, buoyancy effects, thermal acceleration, secondary flow, near-wall turbulence suppression, thermal stratification, flow maldistribution, wall temperature rise, and instability.

The studies were classified based on their different operating conditions, such as pressure, inlet temperature, wall and bulk temperatures relative to the pseudo-critical temperature, G, q″, Re, flow orientation, heating distribution, and boundary conditions. Where possible, reported parameters were normalised and/or converted to consistent SI units, specifically G (kg/m^2 s), q″ (W/m^2 or W/cm^2), ΔP (MPa), and h (W/m^2 K).

The studies were organised according to performance metrics, for example h, Nu, heat transfer enhancement ratio, f, ΔP penalty, pumping-power implications, thermal performance factor, performance evaluation criterion (PEC), temperature uniformity, wall temperature reduction, HTD tendency, instability threshold, and correlation prediction error.

Sixth, the studies were categorised with respect to application domain, such as Brayton cycle heat exchangers, PCHE recuperators and precoolers, electronics cooling, aerospace regenerative cooling, nuclear thermal systems, waste heat recovery, compact heat sinks, and special high-q″ devices. This differentiation was established because the results from one application domain may not be generally extrapolated to another owing to significant differences in ΔP, q″, channel scale, and heating mode.

The scope and synthesis activities produced the following outputs.

The selected literature was synthesised according to hydraulic scale, geometry, heat transfer mechanisms, operating conditions, applications and predictive-modelling approaches. Four analysis levels were supported by the retained literature. The first level focuses on the physical mechanisms underlying near-pseudocritical heat transfer, such as property variation, pseudo-boiling-like behaviour, variable-property convection, buoyancy, thermal acceleration, and turbulence modification. The second level compares the behaviour of tubes, micro/minichannels, PCHEs, and enhanced passages, using their channel geometries. The third level analyses thermo–hydraulic trade-offs based on frequently adopted performance parameters, specifically heat transfer enhancement, ΔP penalty, thermal performance factor, pumping-power implications, compactness, and temperature uniformity. The fourth level considers predictive correlations and models, focusing on their applicable ranges, reported errors, assumptions, and applicability to compact or non-uniformly heated geometries.

The methodology underpins the revised structure of the review. In the following sections, the retained evidence is evaluated not just to summarise the literature, but to detect common mechanisms, to explain conflicting results, and to suggest practical limits for engineering applications.

3. Flow and Heat Transfer Characteristics in Compact sCO$_2$ Passages

The geometry comparisons in this section are interpreted through the mechanism framework developed in Section 4. Near the pseudo-critical region, variations in density, specific heat, viscosity, and thermal conductivity alter the local transport balance. Depending on flow orientation, heating conditions, and operating state, buoyancy and thermal acceleration can modify velocity profiles, turbulence production, and wall-normal heat transport. HTD may develop when these changes impair heat removal from the heated wall. This framework describes interacting processes whose relative importance must be established for each configuration.

Geometry influences these processes through several routes. Curvature generates secondary flow; area variation modifies local acceleration; ribs, fins, and inserts redistribute flow and renew the near-wall fluid; and headers govern the distribution of coolant between parallel passages. Their thermal benefit therefore depends on whether the induced flow changes counteract the mechanism limiting heat transfer under the investigated conditions.

Accordingly, the following comparisons address three questions: Which mechanism limits performance, how the geometry modifies that mechanism, and whether the resulting thermal improvement justifies its hydraulic cost. Reported h, ΔP, and PEC values are interpreted within their original operating conditions and comparison baselines. Tube studies provide mechanistic reference cases, followed by micro/minichannels, PCHEs, and enhanced passages.

3.1. Straight, Curved, and Profiled Tubes: The Effects of Geometry, Orientation, and Heating

Tube-based configurations are crucial for the interpretation of sCO_2 heat transfer in compact thermal systems. They enable the effects of buoyancy, thermal acceleration, thermophysical-property variation, flow direction, and heat distribution to be isolated. However, the examined studies indicate that tube-based configurations should not be viewed as straightforward baseline cases. Even in geometrically simple passages, the local thermodynamic state, wall heating, D_h, inlet conditions, and ΔP interact to control heat transfer. Consequently, tube studies are important not only to provide reference data; they also define the conditions under which near-pseudocritical heat transfer enhancement can give rise to HTD.

The studies discussed in this section are divided into four groups in line with the main design aspect under investigation: straight round tubes, curved/serpentine passages, tapered/profiled tubes, together with uniform/non-uniform heating cases. These studies reveal that geometry is not the only factor dictating performance. In practice, geometry also modifies the interaction between buoyancy, thermal acceleration, secondary flow, and wall temperature non-uniformity under specific G, q″, ΔP, and inlet thermodynamic conditions. Therefore, the results presented in Figures 3–7 and in Table 2 underline the need for a conditional rather than universal interpretation of tube-scale sCO_2 performance.

3.1.1. Straight Round Tubes Under Horizontal and Vertical Operation

Straight round tubes provide the clearest basis for differentiating buoyancy-dominated, acceleration-dominated, and property-variation-dominated behaviour. Regarding horizontal tubes, the fundamental concern is not only whether HTD occurs, but where and why it develops around the circumference. Wang et al. [25], Pu et al. [26], and Kim et al. [27] found that the combination of q″, buoyancy-induced density redistribution, and proximity to the pseudo-critical region are important drivers of circumferential asymmetry. Wang et al. [25] illustrated the effects of increasing q″ on circumferential thermal non-uniformity and reducing pressure below the critical pressure on the maximum h, as shown in Figure 3a. In Figure 3b, Pu et al. [26] evaluated the mixed-convection contribution using a Petukhov buoyancy number of approximately 6.0, suggesting that the natural-convection effects are significant under turbulent forced-convection conditions. Moreover, Kim et al. [27] explained the local wall response by demonstrating that deterioration occurs earlier at the upper wall owing to the upward migration of the heated, low density fluid, as shown in Figure 3c.

Collectively, these studies indicate that q″ and buoyancy do not independently determine the occurrence of HTD in horizontal tubes. More specifically, this is due to buoyancy redistributing the low-density fluid, thermal acceleration modifying the near-wall velocity field, and the wall state or bulk fluid state entering the pseudo-critical region. This interpretation is important because it explains why average h may conceal deterioration locally. A tube can demonstrate good average thermal performance while being subjected to early thermal degradation at the upper wall. Consequently, regarding horizontal tubes, local circumferential wall temperature data are required when employing these configurations as validation cases for compact heat exchangers.

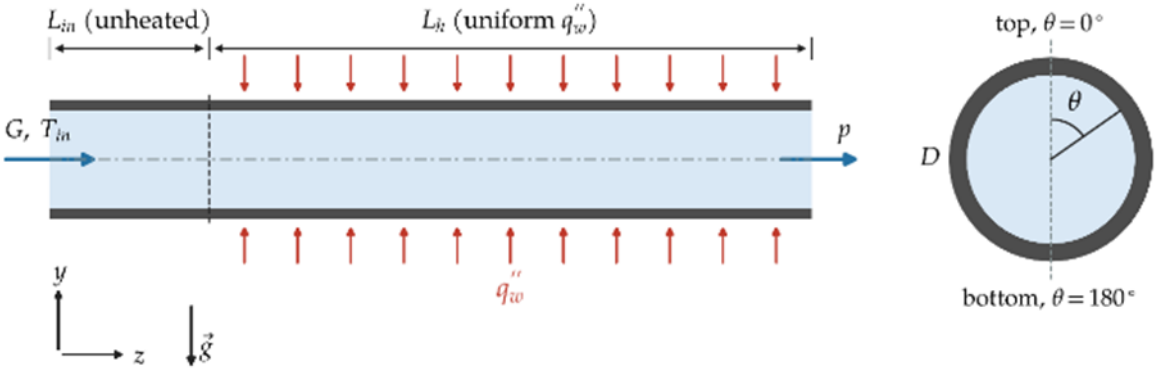
These studies reveal a modelling issue because the predicted onset of deterioration depends significantly on the buoyancy criterion applied. Pu et al. [26] used the Petukhov buoyancy parameter, while Kim et al. [27] used an alternative buoyancy parameter to better demonstrate the deterioration trend. This does not imply that a universal buoyancy parameter is applicable to all sCO_2 tube flows. The findings suggest that deterioration thresholds are sensitive to how density variation, property gradients, and flow direction are assimilated into the criterion. This recognises the fact that a correlation which performs well for one dataset may not be suitable for another dataset when the pressure, q″, or orientation ranges vary.

This is confirmed by studies of small-diameter tubes. For a horizontal 2 mm tube, Wahl et al. [28] created a Dittus–Boelter-type correlation for G = 400–1300 kg/m^2 s and p = 77–85 bar, with a prediction error of about 20%, as depicted in Figure 3d. Guo et al. [29] analysed heat transfer deterioration in a 2 mm microtube under conditions of p = 7.6–8.4 MPa and q″/G = 250–500 J/kg. They established that the degree of deterioration increases, whereas the h decreases with decreasing G and increasing q″. These results show that near-pseudocritical heat transfer complexity persists in small-diameter tubes. However, the observed behaviour depends jointly on hydraulic diameter, pressure, q″/G, inlet state, and local wall conditions. The findings therefore do not isolate channel size as the cause of stronger property gradients or reduced predictive accuracy.

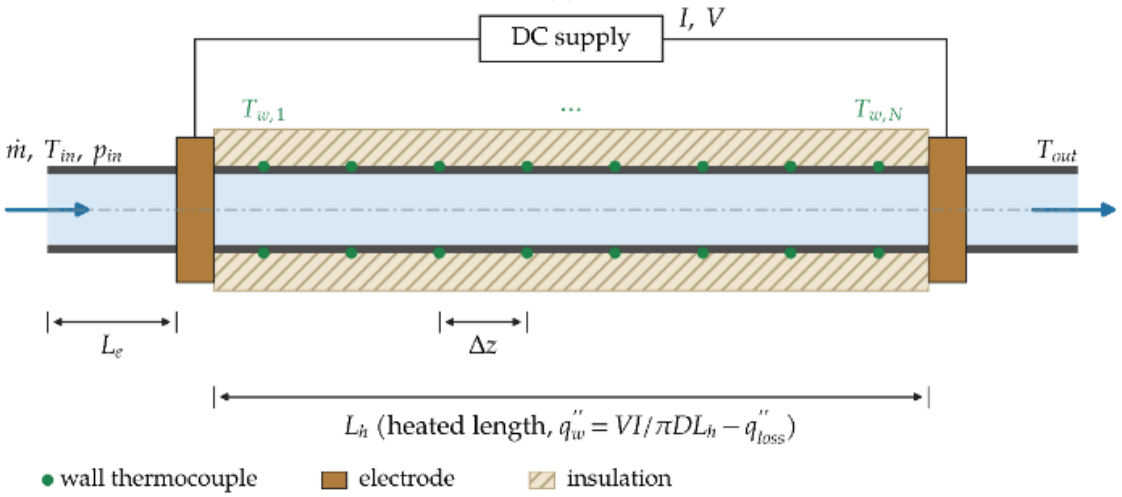
The relationship between buoyancy, ΔP, and thermal acceleration varies with flow direction, adding an additional layer of complexity to the vertical-flow experiments. Under relatively low G and low q″, Kim and Kim [30] demonstrated that wall temperature peaks can appear in the 4.5 mm upward-flow tube, where buoyancy and thermal acceleration can promote instead of mitigate the deterioration, as shown in Figure 4a. According to Chen et al. [31], the h increases with pressure and G, while the wall temperature decreases. However, the turbulence behaviour can become more complicated as the Reynolds-stress shear decreases, as shown in Figure 4b. Their proposed correlation was able to predict 79.3% of the data within ±10% and all data within ±20%. The results suggest that integrating property-ratio and turbulence-related terms is essential to enhance predictive performance.

Theologou et al. [32] and Wang et al. [33] demonstrate the importance of considering heat transfer in conjunction with ΔP partitioning and the inlet thermodynamic condition. Theologou et al. [32] concluded that the friction component of ΔP continues to be dominant, while the hydrostatic and acceleration components amount to 4–24% and 12–30%, respectively (Figure 4c). Despite the dominance of the frictional component, the total ΔP for downward flow was around 6–7% higher than that for upward flow. Wang et al. [33] observed that the inlet condition affects the local and average h and ΔP. With and without the inclusion of wall temperature information, they reported average absolute deviations (AADs) for heat transfer of 4.79% and 4.44%, respectively, along with flow-correlation errors of 14.61% and 9.39%, respectively (Figure 4d).

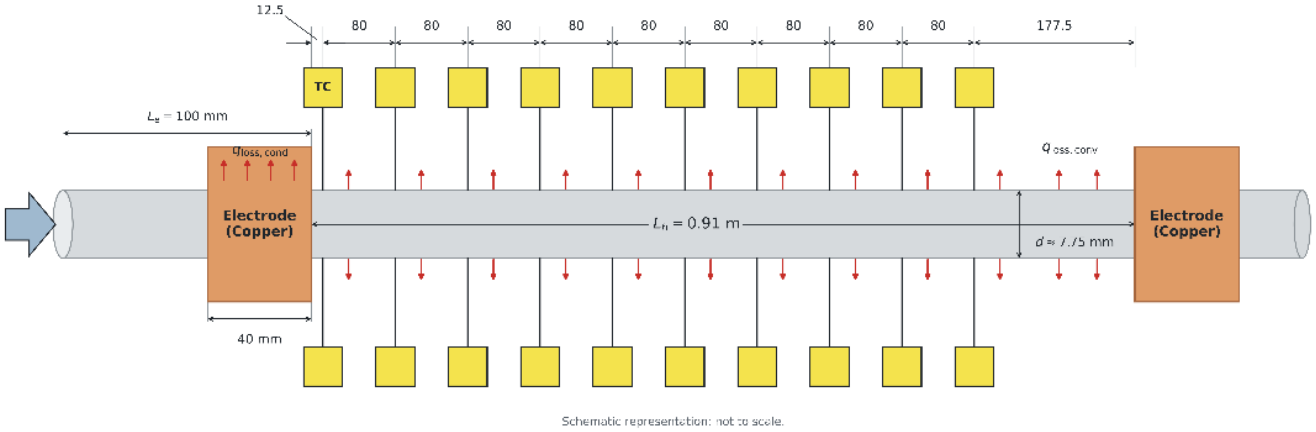
The results presented here indicate that correlations developed for straight tubes should be used with caution. They should not be transferred from one inlet configuration to another or from one flow orientation to another without careful consideration. Flow in the same tube can reveal different characteristics depending on the flow direction (horizontal, upward, and downward) and the inlet condition (liquid-like, pseudo-critical, and gas-like). As a result, a straight tube should not be regarded as a universally scalable model, but as a mechanical standard.


L_{in} (unheated)
L_h (uniform q''_w)
G, T_{in}
p
q''_w
y
z
$\vec{g}$
top, $\theta = 0°$
θ
D
bottom, $\theta = 180°$

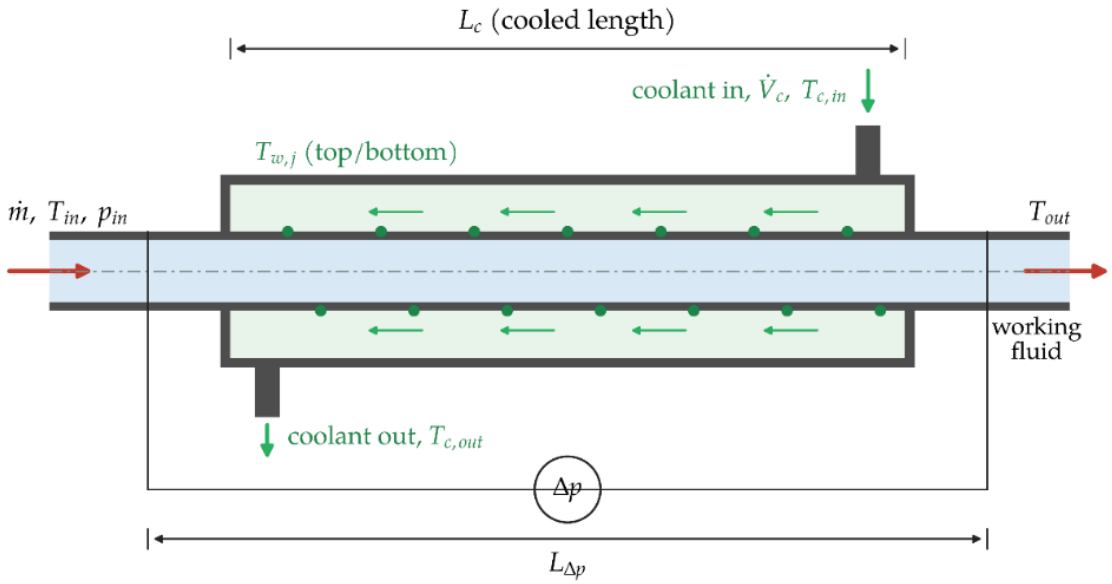
(**a**)


DC supply
I, V
$T_{w,1}$
...
$T_{w,N}$
$\dot{m}$, T_{in}, p_{in}
T_{out}
L_e
Δz
L_h (heated length, $q''_w = VI/\pi DL_h - q''_{loss}$)
wall thermocouple
electrode
insulation

(**b**)

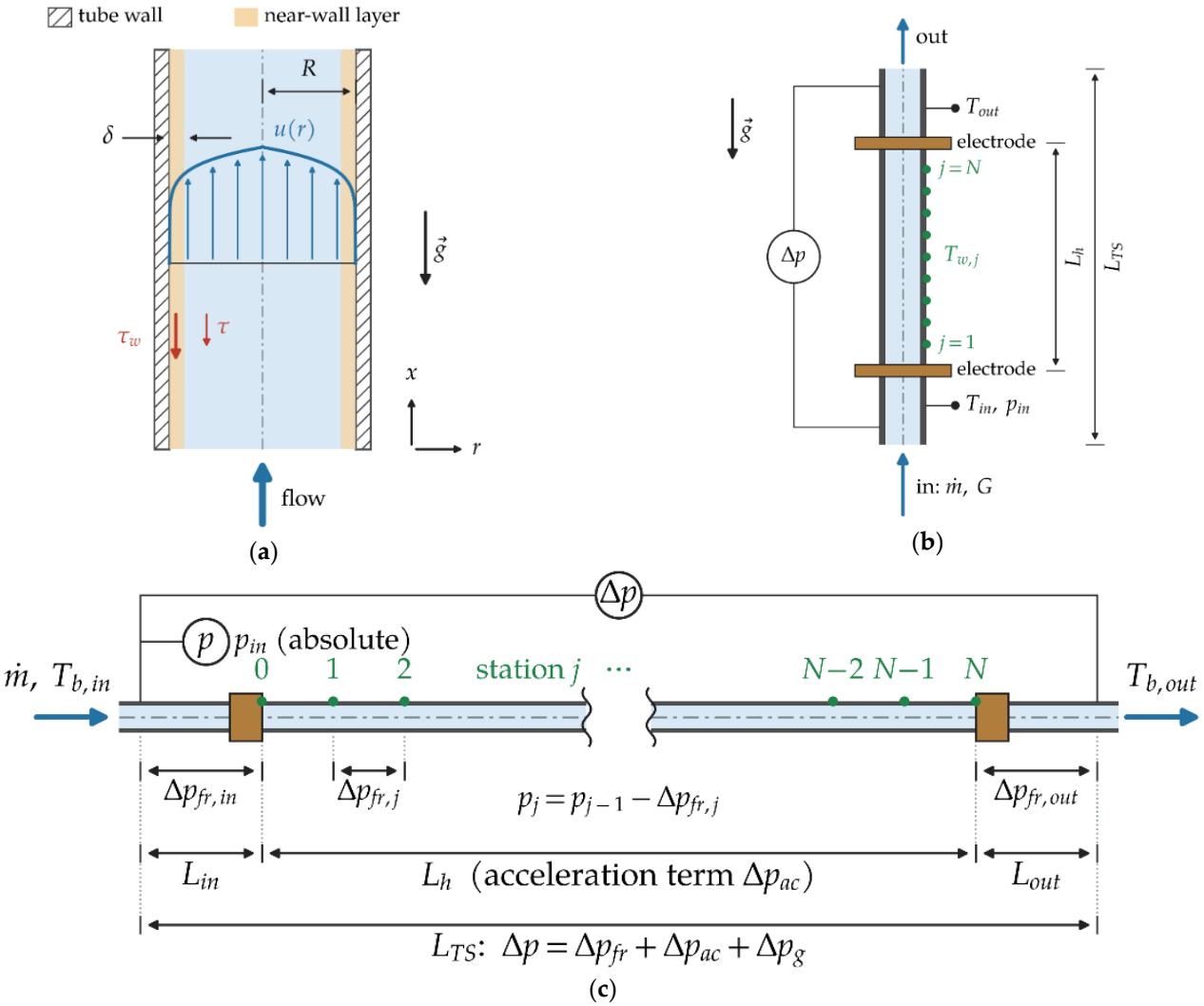

12.5
80
80
80
80
80
80
80
80
80
177.5
TC
L_e = 100 mm
$q_{loss,cond}$
$q_{loss,conv}$
Electrode (Copper)
L_h = 0.91 m
Electrode (Copper)
40 mm
Schematic representation: not to scale.

(**c**)

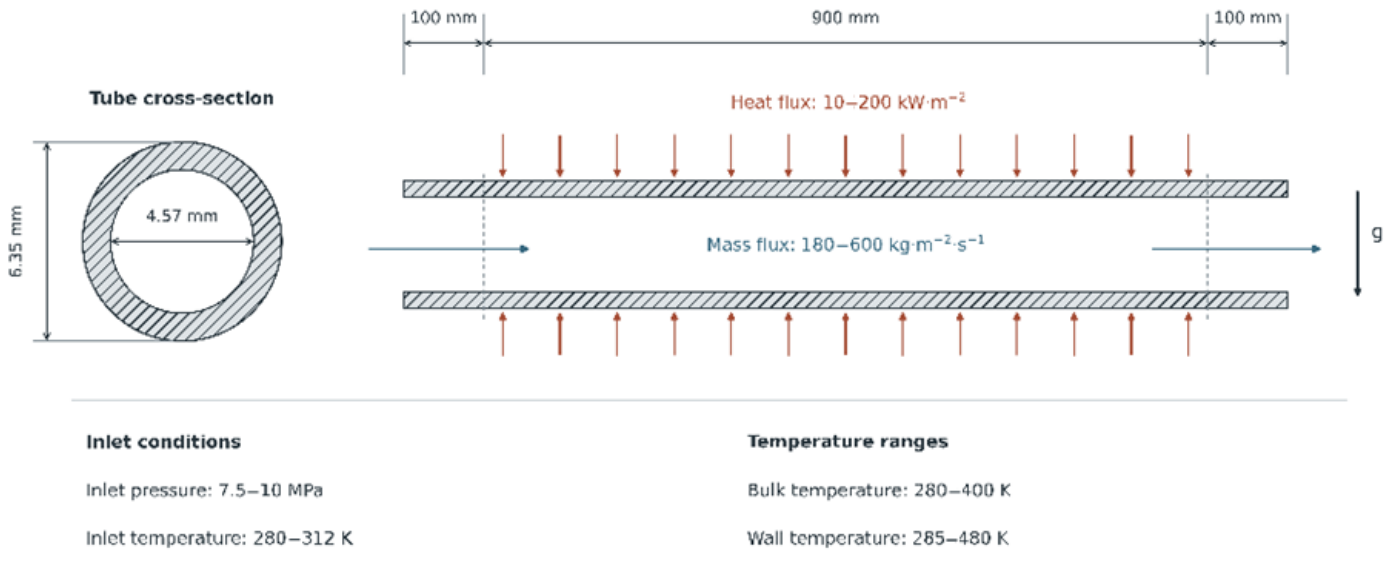


(**d**)

Figure 3. Straight Round Tubes: (**a**) Wang et al. [25]; (**b**) Pu et al. [26]; (**c**) Kim et al. [27]; and (**d**) Wahl et al. [28].



https://doi.org/10.3390/en19215380



(**d**)

Figure 4. Straight round tubes: (**a**) Kim and Kim [30]; (**b**) Chen et al. [31]; (**c**) Theologou et al. [32]; (**d**) Wang et al. [33].

3.1.2. Curved, U-Bend, and Serpentine Passages

Curved, U-bend, and serpentine passages produce centrifugal forces and secondary vortices within the fluid, which may modify the near-wall flow distribution and reduce buoyancy-induced stratification. Therefore, their benefit over straight tubes is predominantly mechanical because they promote cross-sectional mixing and disrupt the layer of low-density, gas-like fluid that can develop close to the wall. Nonetheless, the reviewed studies indicate that curvature does not automatically enhance heat transfer performance. To be effective, it depends on the flow direction, radius of curvature, heating asymmetry, and its ability to redistribute hot spots in a uniform direction to generate a more uniform flow.

At 9 MPa, Wu et al. [34] reported signed heating-section pressure differences of −104.73 Pa for down–up flow and 1023.88 Pa for up–down flow. Using up–down flow as the reference gives [1023.88 − (−104.73)]/1023.88 × 100 = 110.23%. This comparison includes gravitational and acceleration effects alongside flow resistance; the source does not separately quantify these contributions. It therefore does not establish an equivalent reduction in frictional resistance or pumping power. Consequently, both the geometric curvature and the distribution of the buoyancy body force resulting from density gradients must be taken into consideration.

In an inclined mini-channel, Su So et al. [35] studied a 2 mm serpentine mini-channel. They concluded that inclination is limited when the radius of curvature is kept constant because the centrifugal effect dominates, as illustrated in Figure 5a. As the radius of curvature changes, buoyancy intensifies and stratification is more noticeable, specifically in the gas-like regions. For compact systems, this difference is significant because it demonstrates that stratification can prevent curvature only when the resulting secondary flow is sufficiently developed and stable throughout the passage.

Wang et al. [36] also emphasise the trade-off between heat transfer enhancement and thermal uniformity, as depicted in Figure 5b. For the semi-circumferentially heated serpentine tube, an 8% improvement in the Colburn (j) factor and a 9% improvement in the Fanning f were reported, with a PEC of 1.045–1.049. Similarly, the local h reached up to 1.285 times the value for the straight tube. However, the same study reported axial temperature differences greater than 500 K and cross-sectional differences exceeding 180

K. The results reveal that improved thermal performance does not lead to enhanced local performance.

Under asymmetric heating, severe thermal non-uniformity can be realised in curved passages despite increased heat transfer. Consequently, the use of curved and serpentine passages as heat transfer enhancement strategies is not universal. They are useful when the secondary flow moderates stratification and if the ΔP penalty is not excessive. Their advantage diminishes when the geometry generates large local temperature differences or when the additional flow resistance offsets the heat transfer benefit.

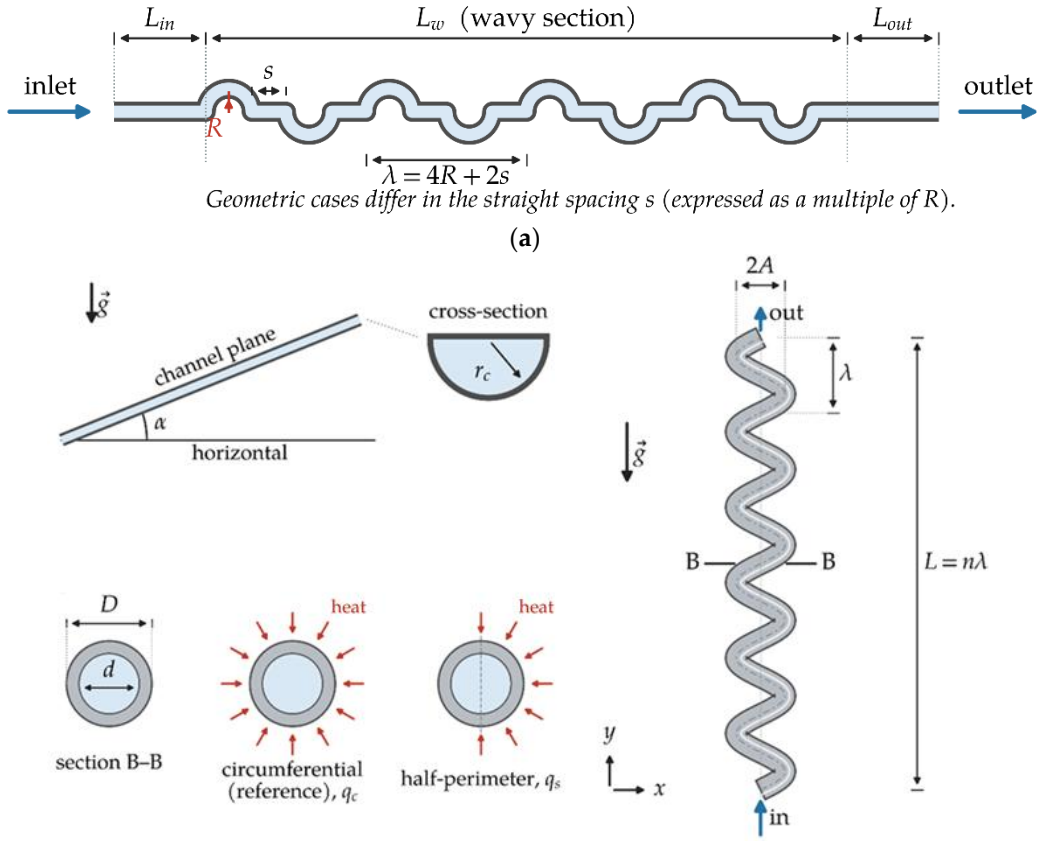


Figure 5. Curved designs: (**a**) Su So et al. [35]; (**b**) Wang et al. [36].

3.1.3. Tapered and Profiled Tubes: Enhancement Versus ΔP Trade-Offs

The use of tapered and profiled tubes modifies the local flow area, boundary-layer development, acceleration field, and wall contact behaviour. In contrast to the straight or uniformly curved passage, the primary design advantage is the ability to precisely modify the balance between heat transfer and ΔP. However, the evidence reviewed implies that they should be evaluated in terms of design objective as opposed to an individual enhancement measure.

The performance of mini-tubes was investigated by Ghodrati and Khoshvaght-Aliabadi [9], as shown in Figure 6a. The results confirmed that increasing the divergence angle improved heat transfer by 5.2–28.6% while reducing the ΔP by 52.1–68.5%. This is significant given that it contradicts the widespread view that increasing the size of a system component gives rise to efficiency losses. Hydraulic resistance can be reduced in diverging passages without compromising heat transfer. However, the divergence must be controlled to prevent adverse flow separation and poor near-wall renewal.

Conversely, Khoshvaght-Aliabadi et al. [37] observed that flattened tubes with alternating flow demonstrated heat transfer improvements of around 64–65% for

downflow and 44% for upflow. Under transcritical conditions, the subsequent improvements were approximately 48% and 38%, respectively (Figure 6b). The benefits are associated with a higher ΔP penalty, which suggests that flattened or non-circular passages are more appropriate if the aim is to maximise heat transfer as opposed to hydraulic economy.

Both studies provide a good contrast to define the boundaries of the design space. Regarding systems where reducing ΔP or pumping power is the main concern, diverging tubes are more appropriate, while flattened or profiled tubes are more appropriate for high q″ applications where heat transfer enhancement is the principal objective. Accordingly, profiled tubes cannot be regarded as universally superior. Their practicality depends on whether the system is heat transfer limited or ΔP limited.

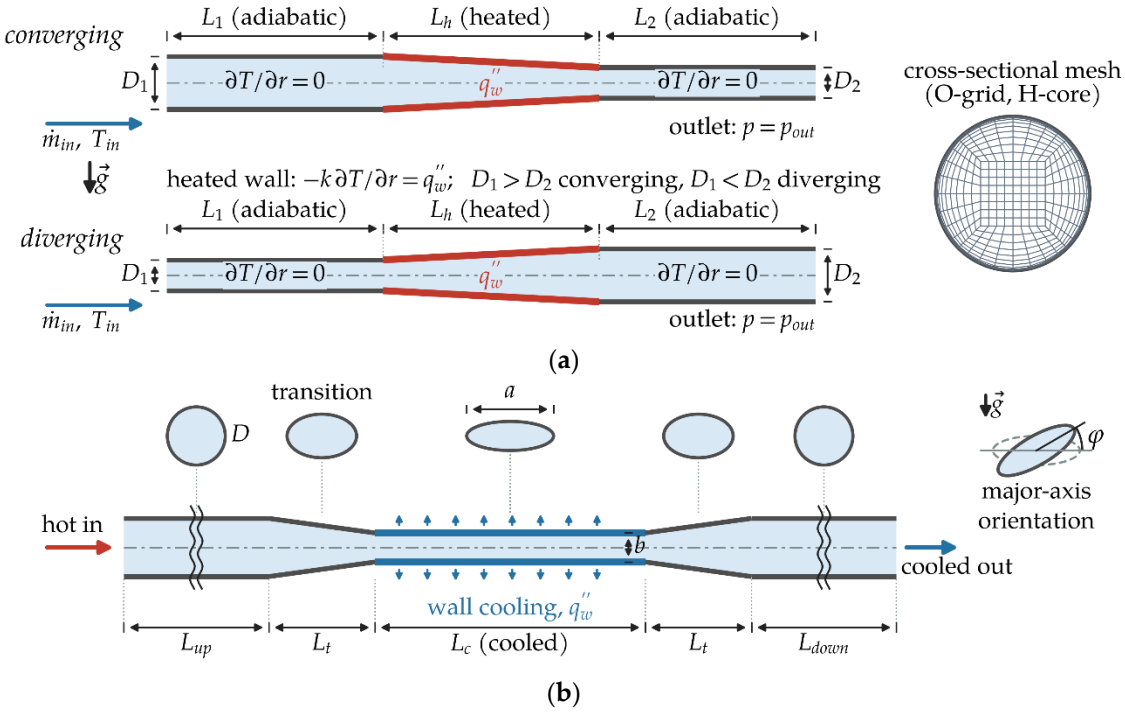


Figure 6. Tapered and non-circular tubes: (**a**) Ghodrati and Khoshvaght-Aliabadi [9]; (**b**) Khoshvaght-Aliabadi et al. [37].

3.1.4. Influence of Uniform and Non-Uniform Heating on Tube Performance

In sCO_2 tube flow, the heating distribution should not be regarded as a second boundary condition, given that it controls local phenomena near the pseudo-critical region, consisting of wall temperature, buoyancy, turbulence suppression, and property variations. The reviewed studies demonstrate that non-uniform heating can change the position of the maximum heat transfer, increase circumferential heat transfer asymmetry, and reduce the reliability of the correlations developed under uniform heating conditions.

Under high q″ conditions, Yu et al. [38] established that using a turbulent Prandtl number of 0.55 to 0.60 reduced the prediction error of the inner-wall temperature and h of approximately 13% and 27%, respectively, compared with Prt = 1, as shown in Figure 7a. This finding denotes the sensitivity of numerical predictions to the modelling of near-wall turbulent q″. The conventional turbulence closure could describe the bulk trends in sCO_2, but was unable to predict the local wall temperature response when steep property gradients were depicted.

Zhang et al. [39] found that circumferential non-uniformity typically has a negative effect on convective heat transfer performance. However, when the heat source is located

on the lower wall, non-uniform heating can have a positive effect on performance under high q″, as described in Figure 7b. This is because the location of the heated wall can either enhance or disrupt stratification. Therefore, it is possible to achieve different results from the same q″, depending on the circumferential location of the tube.

Yang et al. [40] showed that non-uniform heating can significantly reduce the average heat transfer performance. Depending on the heat-source position and operating conditions, reductions of 13–68% were observed (Figure 7c). The wide range implies that non-uniform heating not only causes local wall temperature variations, but also affects confidence in average design correlations. Consequently, for a compact thermal system with one-sided, circumferentially asymmetric or localised heat loading, heat transfer data from uniform heating must be used with caution.

Heat distribution should be considered a fundamental design and modelling variable. Non-uniform heating promotes local stratification, high model sensitivity, and the potential for hidden wall temperature peaks, while uniform heating provides more stable and transferable reference behaviour.

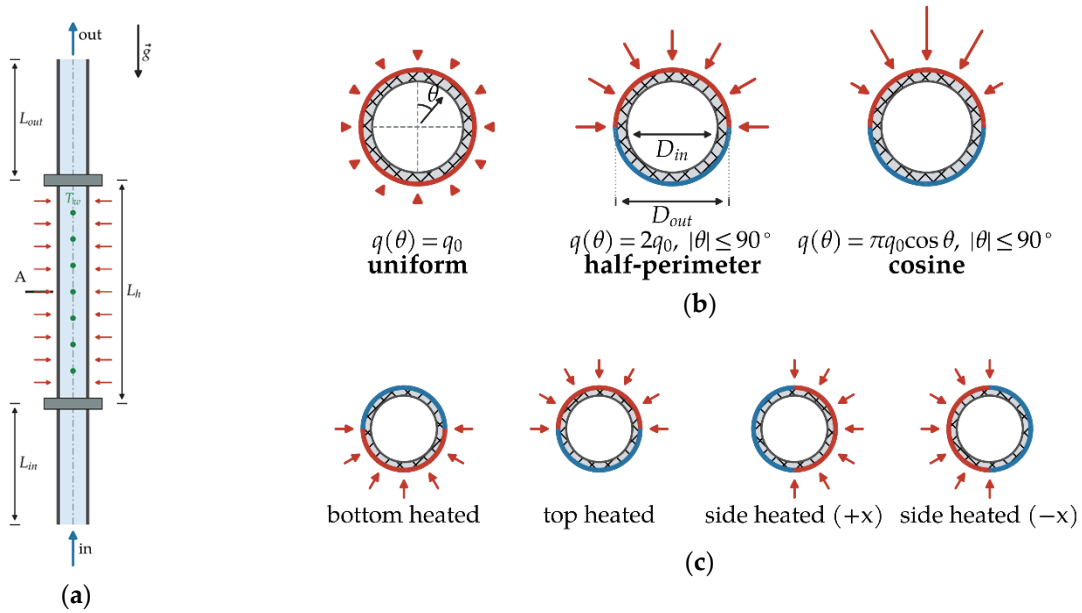


Figure 7. Comparison of uniform and non-uniform heating: (**a**) Yu et al. [38]; (**b**) Zhang et al. [39]; (**c**) Yang et al. [40].

Table 2. Comparison of thermo–hydraulic trends in straight, curved, profiled, and non-uniformly heated sCO_2 tubes.

Category	Main Studies	Hydraulic Scale/Operating Condition	Dominant Mechanisms	Main Quantitative Findings	Design Boundary and Implications
Straight horizontal tubes	Wang et al. [25], Pu et al. [26] and Kim et al. [27]	Horizontal tubes near the pseudo-critical region q″ and pressure-sensitive operation	Circumferential density redistribution, buoyancy, thermal acceleration, upper-wall deterioration	Petukhov buoyancy threshold ≈ 6.0; higher q″ intensifies circumferential non-uniformity; top-wall deterioration occurring earlier	Average h is insufficient for design. Local wall temperature and circumferential asymmetry must be considered, specifically under low-G/high q″ conditions.
Straight mini/microtubes	Wahl et al. [28] and Guo et al. [29]	2 mm tubes; G = 400–1300 kg/m² s and P = 77–85 bar Wahl et al. [28]; P = 7.6–8.4 MPa and q″/G = 250–500 J/kg	Intensified property gradients, q″/G sensitivity, reduced D_h effects	Prediction accuracy about 20%; higher q″ and lower G reduce h and increase tendency to deteriorate	Mini/micro scaling does not eliminate near-critical complexity; compact channels require correlations that consider local-property and heating conditions.
Straight vertical tubes	Kim and Kim [30], Chen et al. [31], Theologou et al. [32] and Wang et al. [33]	Vertical upward/downward flows; 4.5 mm upward tube in Kim and Kim [30]; inlet state relative to Tpc is important	Flow-direction effects, buoyancy-acceleration coupling, ΔP partitioning, inlet-state sensitivity	Chen et al. [31]: 79.3% of data within ±10% and 100% within ±20%; hydrostatic and acceleration contributions of 4–24% and 12–30%; downward flow increases ΔP by ~6–7%. Wang et al. [33]: heat transfer AADs of 4.79% and 4.44%, flow-correlation errors of 14.61% and 9.39%	Heat transfer, ΔP, inlet state, and flow direction must be evaluated concurrently. Correlations calibrated for one orientation or inlet regime may not transfer reliably.
Curved/serpentine tubes	Wu et al. [34], Su So et al. [35] and Wang et al. [36]	U-bend and serpentine passages; 2 mm serpentine mini-channel in Su So et al. [35]; semi-circumferential heating in Wang et al. [36]	Centrifugal secondary flow, curvature-induced mixing, suppression, or re-emergence of buoyancy effects	Wu et al. [34]: average h +9.00–10.60% for down–up versus up–down flow. At 9 MPa, signed pressure differences were −104.73 Pa and 1023.88 Pa, respectively; the reported 110.23% comparison does not	Curvature can improve mixing, but benefits are configuration-specific. Local thermal non-uniformity may persist even when average performance improves.

				represent a frictional-loss reduction. Wang et al. [36]: j +8%, f +9%, PEC = 1.045–1.049, local h up to 1.285×; axial ΔT > 500 K and cross-sectional ΔT > 180 K	
Tapered/profiled tubes	Ghodrati and Khoshvaght-Aliabadi [9], and Khoshvaght-Aliabadi et al. [37]	Diverging mini-tubes and alternating flattened tubes near pseudo-critical/transcritical conditions	Local area variation, boundary-layer redevelopment, acceleration/deceleration effects	Diverging tubes: heat transfer +5.2–28.6% and ΔP −52.1 to −68.5%; flattened tubes: heat transfer gains of ~64–65% in downflow and ~44% in upflow; transcritical gains of ~48% and ~38%	Diverging tubes are suitable for low-ΔP objectives; flattened/profiled tubes are better suited to high-h objectives but require acceptance of hydraulic penalty.
Uniform vs. non-uniform heating	Yu et al. [38], Zhang et al. [39], and Yang et al. [40]	Uniform, circumferentially non-uniform, and localised heating; high-q″ sensitivity	Heating asymmetry, turbulence-model sensitivity, buoyancy–wall-location interaction	Adjusted Prt = 0.55–0.60 reduced wall temperature and h errors by ~13% and ~27%; non-uniform heating caused average performance loss of ~13–68%	Heating pattern is a primary design variable. Uniform-heating correlations should be applied cautiously to one-sided or asymmetric heating cases.

3.2. Micro/Minichannels and Heat-Sink Architectures for High-q" Cooling

The effects of miniaturisation depend on pressure, mass flux, heat flux, heating distribution, and proximity to the pseudo-critical temperature. Reduced D_h alone does not establish stronger property gradients or greater sensitivity to non-uniform heating. Comparisons with larger tubes therefore require compatible operating conditions and consideration of buoyancy, inertia, and thermal acceleration.

The results presented in Figures 8–10 and Table 3 show that the three coupled effects influence the performance of the sCO_2 micro/minichannels. First, the pseudo-critical region is crossed locally, thus determining the location and magnitude of the peak heat transfer. Second, flow redevelopment prompted by geometry, such as ribs, baffles, constrictions, and wavy passages, can enhance mixing and thermal uniformity, but typically at the cost of increased hydraulic cost. Third, non-uniform heating and mixed convection can alter the location of maximum heat transfer and reduce the reliability of standard correlations. Accordingly, the main design question is not whether micro/minichannels are useful to improve heat transfer in sCO_2, but when, where, and how they can do so without experiencing too much additional ΔP or local thermal non-uniformity.

3.2.1. Flow Regimes and Near-Critical Transitions in Microchannels

A fundamental characteristic of sCO_2 microchannel heat transfer is the development of the flow regime around the pseudo-critical region. In contrast to traditional single-phase fluids, the thermal response of sCO_2 does not simply depend on Re or q". It is extremely dependent on the approach to or crossing of the pseudo-critical temperature by the wall and bulk temperatures. In microchannels, the effect is intensified by the small D_h, which produces steep wall-normal temperature and density gradients. Hence, regime transitions are not global phenomena, but take place locally and are ongoing.

Employing a 500 μm square microchannel, Whitaker et al. [41] identified three q"-driven regimes at Pr = 1.05, as illustrated in Figure 8a. Peak heat transfer was achieved as the bulk fluid passed through Tpc. Subsequently, heat transfer performance decreased as the core fluid became gas-like. It is important to note here that the favourable effect of the Cp peak is only temporary and location-dependent. If the core enters the gaseous phase, the h may decrease owing to changes in near-wall transport properties, even when the system remains in the vicinity of the pseudo-critical region.

Whitaker and Rao [42] extended this interpretation over G = 100–1000 kg/m² s and q" = 2–100 W/cm², as shown in Figure 8b. Consistent with their results, heat transfer behaviour similar to that observed at supercritical pressure can develop even at slightly subcritical or near-critical pressures when the local thermodynamic path passes through a region of steep property gradients.

Consequently, the classification of the transport regime using only nominal system pressure is inadequate. The local temperature–pressure path in relation to the pseudo-critical line is more applicable for predicting peak heat transfer, deterioration, and correlation failure.

The sensitivity of this regime's behaviour is supported by local property measurements and simulations. Chen et al. [43] showed that a small temperature change of 0.01 K is accompanied by a density variation of about 1 kg/m³, as depicted in Figure 8c. In microchannels, a small thermal perturbation can affect the near-wall density field, alter local acceleration, and influence wall-normal transport. Bayrak and Ahn [44] reported peaks in the h of a 0.5 mm microtube at approximately 8 MPa, with peaks around x/L = 0.33 and 0.65, as illustrated in Figure 8d. The peaks were associated with thermal acceleration in the near-wall region and the subsequent crossing of the pseudo-critical

temperature by the core fluid. The occurrence of several local peaks, as observed in this case, indicates that heat transfer enhancement can occur at different axial positions depending on how the wall and core regions pass through the pseudo-critical zone.

With respect to modelling, Jajja and Fronk [45] established an important boundary. Conventional correlations underestimated the h in a 923 μm rectangular microchannel with one-sided heating. This emphasises the need for predictive approaches specifically designed for compact channels. Correlations based on bulk properties or on symmetric heating may provide a realistic estimate of the global response, although they may not produce a reliable local response under asymmetric heating. Therefore, modelling microchannel sCO_2 heat transfer should incorporate local property variations, heating distribution, and axial regime evolution, instead of being based on average bulk quantities.

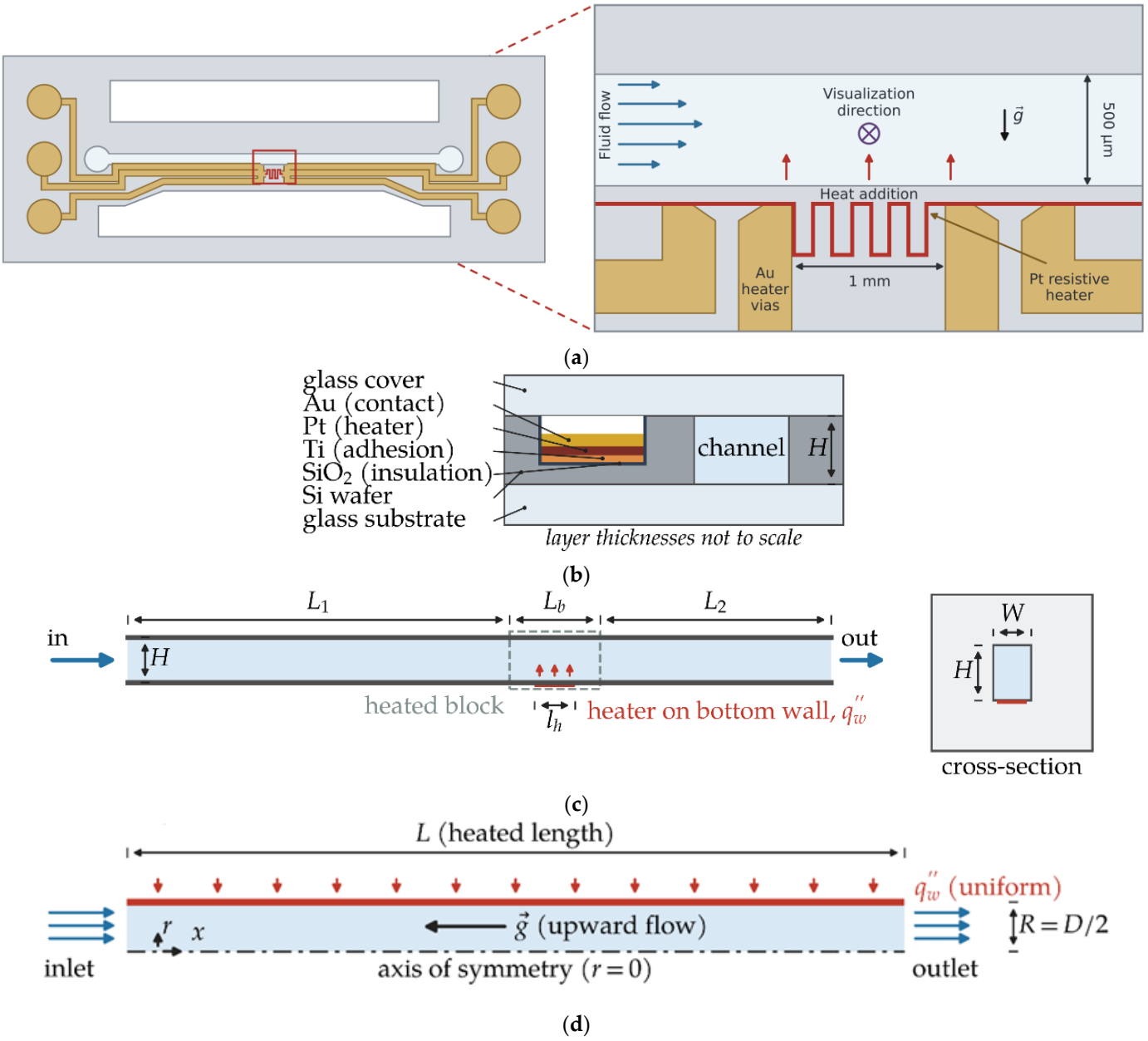


Figure 8. Flow regime studies: (**a**) Whitaker et al. [41]; (**b**) Whitaker and Rao [42]; (**c**) Chen et al. [43]; and (**d**) Bayrak and Ahn [44].

3.2.2. Geometry Optimisation of Microchannel Heat Sinks and Compact Cooling Modules

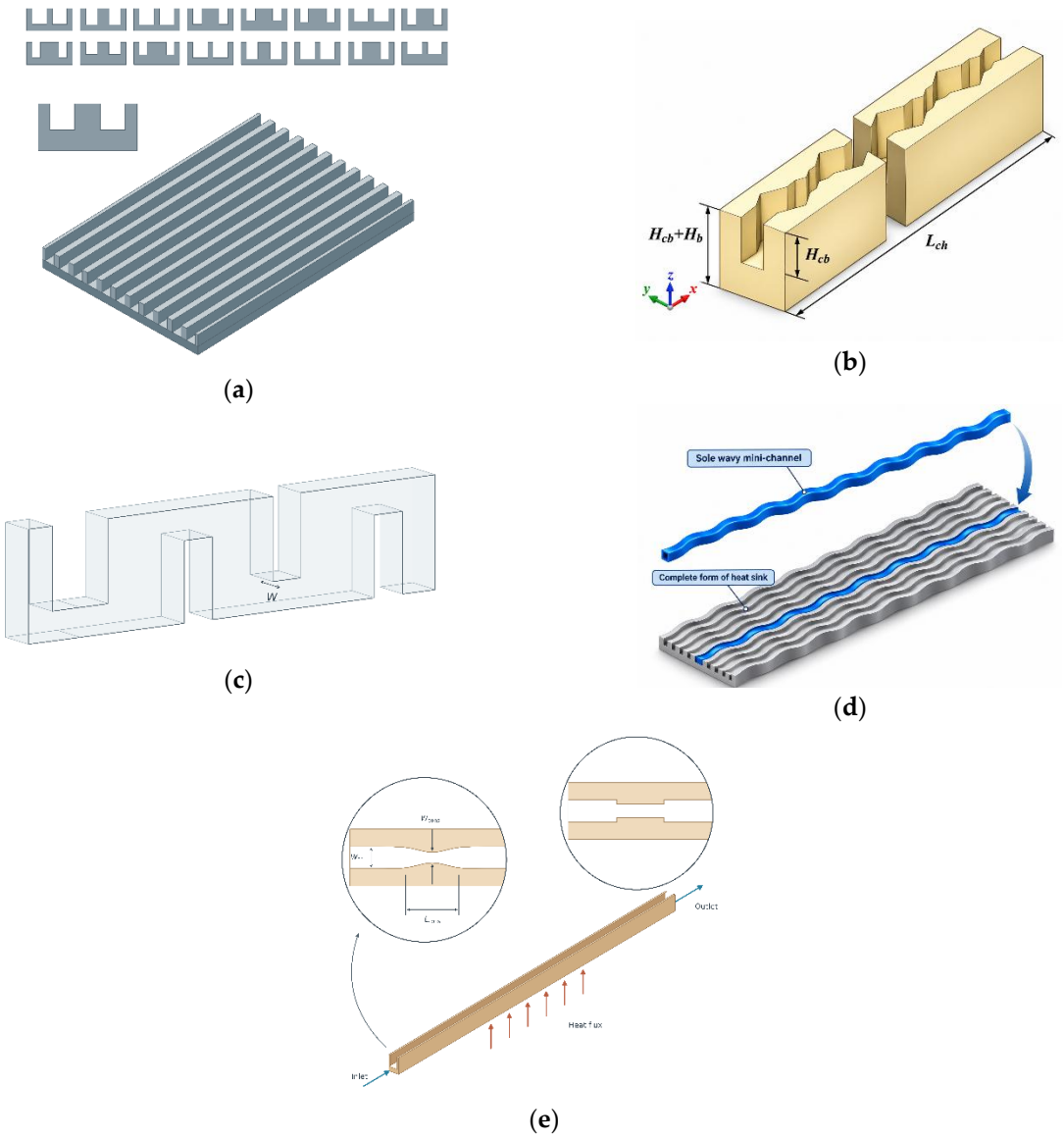
The principal challenge in the geometric optimisation of sCO_2 micro heat sinks is balancing heat transfer enhancement, ΔP penalty, and temperature uniformity. The reviewed studies demonstrate that different geometrical approaches provide specific performance advantages. Area variation can help to balance heat transfer enhancement in contrast to ΔP, whereas ribs or cavities can enhance uniformity. Additionally, wavy or constricted passages can lead to greater heat transfer enhancement, but at a higher hydraulic cost. Accordingly, the h is inadequate to compare the performance of microchannel geometries.

The results obtained by Khoshvaght-Aliabadi et al. [46] indicated that convergent minichannels can improve heat transfer by up to 2.37×, whereas divergent minichannels can reduce ΔP by approximately 0.31 of the baseline value, as depicted in Figure 9a. The dual-direction convergent design also reduced the base temperature by 27.2%, resulting in a performance index of 1.56. The results show that area variation can be useful when decreasing base temperature and hydraulic resistance is taken into account together with heat transfer. The design implication is conditional because converging layouts improve heat transfer while diverging layouts reduce ΔP. As a result, area variation offers design flexibility without being the optimum geometry.

Two other challenges, specifically local mixing and temperature regulation, were investigated by Huang et al. [47] and Kumar and Basu [48], respectively. Huang et al. [47] reduced temperature non-uniformity to 1.8 K in a 0.133 mm microchannel using ribs and cavities, as shown in Figure 9b. This is important because temperature uniformity is occasionally more critical than the maximum h in electronic cooling and compact heat-sink applications. Kumar and Basu [48] investigated the effect of three pairs of baffles with a height of 0.35 mm, thickness of 0.2 mm, and an inclination angle of 60°. Their study found that this configuration achieved the maximum COP with a slight increase in ΔP, as shown in Figure 9c. Both studies demonstrate that the use of mixed structures is valuable for thermal uniformity or controlling base temperature, instead of reducing pumping power.

Wavy and constricted channels generate greater heat transfer enhancement but entail a higher hydraulic penalty. The study conducted by Khoshvaght-Aliabadi et al. [49] revealed a 1.86× increase in thermal performance, in conjunction with a 1.58× increase in ΔP, as shown in Figure 9d. Majmader and Hasan [50] demonstrated that triangular constrictions provide approximately 1.5 times the thermal performance and reduce the base temperature by around 43 K under optimum conditions. Nonetheless, rectangular constrictions led to an increase in h at high G, although this resulted in a higher ΔP. The results indicate that greater mixing and boundary layer disruption enhance cooling capacity. However, they also increase hydraulic resistance and may alter the optimum geometry depending on the G.

In general, the results denote that microchannel geometry should be determined based on which criterion is the most dominant in the design considerations. Converging and diverging layouts are suitable for thermo–hydraulic balancing, while ribbed, cavity, and baffle structures are suitable for temperature uniformity. Wavy and constricted passages are suitable for greater heat transfer enhancement, although they sustain a higher ΔP. These findings corroborate that no single geometry is ideal for all compact sCO_2 heat sink applications.



(**a**) (**b**) (**c**) (**d**) (**e**)

Figure 9. Heat sink geometries: (**a**) Khoshvaght-Aliabadi et al. [46]; (**b**) Huang et al. [47]; (**c**) Kumar and Basu [48]; (**d**) Khoshvaght-Aliabadi et al. [49]; and (**e**) Majmader and Hasan [50].

3.2.3. The Effects of Non-Uniform Heating, Orientation, and Mixed-Convection

When used in practice, compact heat sinks often experience non-uniform heat loads. Localised heat sources, chip-level heat generation, asymmetric wall heating, and non-uniform thermal contact can shift the location where the wall or bulk flow reaches Tpc. This is particularly relevant for sCO_2, because thermophysical properties, such as Cp, density, viscosity, and thermal acceleration, can change significantly with changes in local temperature. Thus, the magnitude of heat transfer and the location of peak performance in the axial and transverse directions can vary for non-uniform heating.

Jajja et al. [51] investigated a 0.75 mm square microchannel. They observed that the maximum h occurs when the bulk temperature is close to Tpc and subsequently decreases as the fluid becomes more gas-like, as indicated in Figure 10a. As q″ increases, the peak h decreases, whereas increasing the G improves the average h. This result suggests that effective heat transfer enhancement near Tpc requires balancing residence time, heating rate, and near-wall property redistribution. If q″ is too high, the wall region can heat too rapidly to a pseudo-critical state, reducing the effectiveness of the pseudo-critical Cp peak.

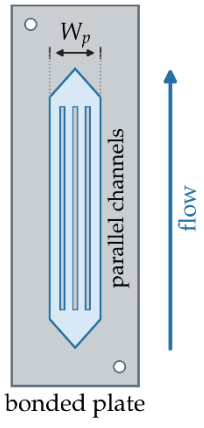
This interpretation is confirmed by the LES results reported by Nabil and Rattner [52], which also provide a modelling implication, as presented in Figure 10b. Their study demonstrated that standard correlations tend to underestimate h at high flux. Their study also observed that h reaches a maximum at an intermediate G and is lowest at low and high G, demonstrating competition between buoyancy and inertial effects. This non-monotonic behaviour is significant because it does not inevitably improve heat transfer. The optimal G is dependent on how effectively inertial forces mitigate stratification, while enabling adequate residence time for the fluid to pass through the pseudo-critical region.

Additionally, these mixed convection effects are modified by geometry and orientation. Jajja et al. [17] reported the minimal effect of orientation in square channels. However, larger-aspect-ratio channels and 525 μm micro-pin-fin arrays improved heat transfer at the cost of increased ΔP, as shown in Figure 10c. This implies that orientation effects are scale- and geometry-dependent. Buoyancy may be less of a consideration in nearly symmetric square passages, whereas local secondary motion and form drag can become more important in high-aspect-ratio or interrupted-flow passages.

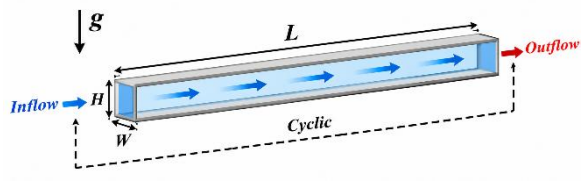
For horizontal minichannels under unilateral heating, Zhang et al. [53] found that buoyancy enhanced circumferentially averaged heat transfer while causing local deterioration at the top wall, whereas thermal acceleration impaired heat transfer, as shown in Figure 10d. Buoyancy and acceleration effects were negligible for $Ri \leq 2.7 \times 10^{-3}$ and $Ac \leq 7.8 \times 10^{-8}$, respectively, using the study's parameter definitions. These thresholds apply to the investigated configuration and heating conditions.

At the device level, the results obtained by Awais et al. [54] reported that the sCO_2 minichannel heat sink delivered a higher h of 42.13% and a lower ΔP of 55.79% at 8.0 MPa and 34 °C, as presented in Figure 10e. Nonetheless, these advantages decreased as pressure and temperature increased. The comparison in this figure demonstrates that sCO_2 can outperform water when operating near the pseudo-critical region, although this advantage depends on the operating window. Accordingly, adequate pressure and temperature control must be maintained to ensure that sCO_2 heat sinks deliver the preferred compact cooling performance. Furthermore, deviations from the optimal operating window may reduce the cooling advantage.

In general, non-uniform heating and mixed convection cause the performance of micro/minichannel sCO_2 to be substantially localised. Peak heat transfer occurs at the point where the wall and bulk states coincide with the pseudo-critical region, while the resulting ΔP and thermal uniformity depend on how the geometry redistributes the flow through this particular region. Consequently, micro/minichannel designs should not be chosen simply on the basis of maximum h. The choice should consider ΔP, base-temperature reduction, thermal uniformity, q″/G, Ri, as well as the operating distance from Tpc.



(**a**)



(**b**)

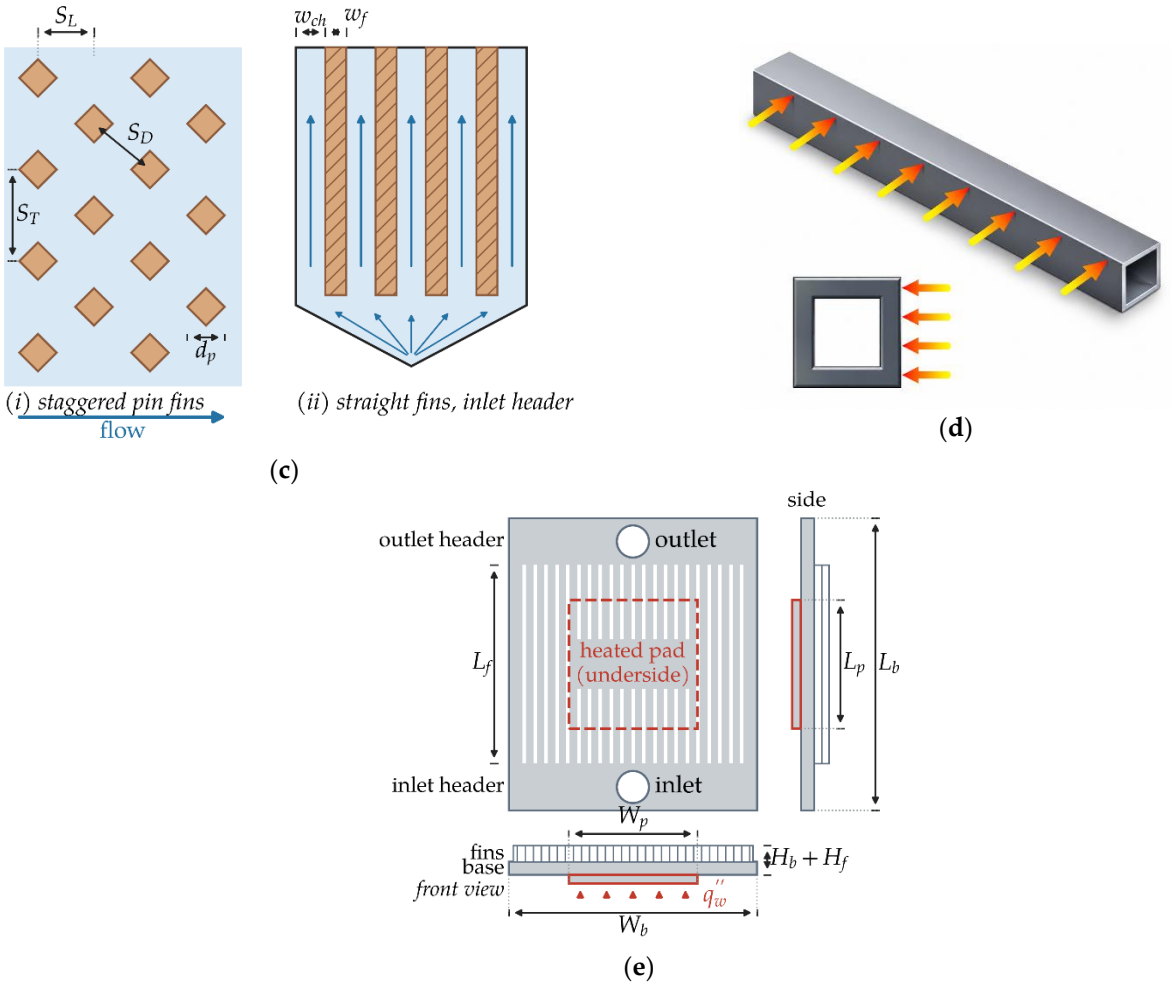


Figure 10. Non-uniform heating investigations: (**a**) Jajja et al. [51]; (**b**) Nabil and Rattner [52]; (**c**) Jajja et al. [17]; (**d**) Zhang et al. [53]; and (**e**) Awais et al. [54].

Table 3. Comparative thermo–hydraulic trends in sCO_2 micro/minichannels and heat sinks.

Category	Main Studies	Hydraulic Scale/Operating Condition	Dominant Mechanisms	Main Quantitative Findings	Design Boundary and Implications
Near-critical flow transitions	Whitaker et al. [41], Whitaker and Rao [42], Chen et al. [43], Bayrak and Ahn [44], and Jajja and Fronk [45]	500 μm square microchannel; 0.5 mm microtube; 923 μm rectangular microchannel; G = 100–1000 kg/m² s; q″ = 2–100 W/cm²; near-critical and slightly subcritical conditions	Local crossing of Tpc, density redistribution, near-wall thermal acceleration, wall-normal property gradients	Three q″-driven regimes in 500 μm channel; continuous transition at G = 100–1000 kg/m² s and q″ = 2–100 W/cm²; 0.01 K perturbation produces an ≈1 kg/m³ density variation; h peaks at x/L ≈ 0.33 and 0.65 in 0.5 mm tube	Peak heat transfer is governed by local thermodynamic state rather than pressure. Conventional correlations are unreliable when wall-normal property gradients and asymmetric heating dominate.
Geometry optimisation	Khoshvaght-Aliabadi et al. [46], Huang et al. [47], and Kumar and Basu [48],	Convergent/divergent minichannels; 0.133 mm ribbed/cavity microchannel; baffles with 0.35 mm height, 0.2 mm thickness and 60° inclination	Area variation, flow redevelopment, local mixing, temperature redistribution	Convergent layout: h increased up to 2.37×; divergent layout: ΔP reduced to ≈0.31 of baseline; base temperature reduced by 27.2%; performance index = 1.56; ribs/cavities reduced temperature non-uniformity to 1.8 K	Geometry should be selected according to the target metric: converging channels for h enhancement, diverging channels for ΔP reduction, and ribs/cavities/baffles for temperature uniformity.
High-enhancement structures	Khoshvaght-Aliabadi et al. [49], and Majmader and Hasan [50].	Wavy and constricted microchannel heat sinks; high q″ compact cooling modules	Boundary-layer disruption, stronger mixing, increased flow resistance	Wavy channels: thermal performance 1.86× and ΔP 1.58×; triangular constrictions: thermal performance ≈ 1.5×; base-temperature reduction ≈43 K	Intensified enhancement improves cooling capacity but increases hydraulic penalty. Suitable when heat transfer gain is preferred over minimum pumping power.
Non-uniform heating and mixed convection	Jajja et al. [51], Nabil and Rattner [52], and Zhang et al. [53]	0.75 mm square microchannel; q″ = 20–40 W/cm²; unilateral heating; mixed-convection conditions	Heating asymmetry, buoyancy–inertia interaction, thermal acceleration, local wall temperature imbalance	Peak h occurs at bulk temperatures slightly above Tpc; higher q″ reduces peak h; standard correlations underpredict h at high q″; Negligible buoyancy for $Ri \leq 2.7 \times 10^{-3}$; negligible acceleration for $Ac \leq 7.8 \times 10^{-8}$.	Heating distribution and Ri explain whether buoyancy and acceleration must be included. Uniform-heating correlations should be used cautiously under localised or one-sided heating.
Orientation and aspect-ratio effects	Jajja et al. [17]	Square and high-aspect-ratio microchannels; 525 μm micro-pin-fin array	Geometry-dependent buoyancy response, secondary flow, form drag	Orientation effect limited in square channels; higher-aspect-ratio channels and micro-pin arrays enhanced heat transfer but increased ΔP	Orientation effects depend on geometry. They are more conspicuous when geometry promotes asymmetric stratification or flow interruption.
Device-level comparison	Awais et al. [54].	sCO_2 minichannel heat sink compared with water at 8.0 MPa and 34 °C	Near-pseudo-critical property advantage, compact heat-sink performance	sCO_2 provided 42.13% higher h and 55.79% lower ΔP than water; performance advantage decreases with increasing pressure and temperature	sCO_2 is most effective when the operating window is maintained close to the pseudo-critical region. Thermal benefits decrease when operating conditions move away from this window.

3.3. Baseline PCHE Configurations and Compact Passage Concepts

PCHEs are one of the most important compact heat exchanger platforms for sCO_2 systems, because they provide small D_h, high surface-area density, high pressure tolerance, and considerable thermal integration potential. These attributes are important in Brayton-cycle recuperators, precoolers, nuclear systems, and high-flux thermal devices. The compactness, which increases heat transfer density, also makes PCHE performance sensitive to channel topology, cross-sectional geometry, flow distribution, local hot spots, and ΔP penalty. Consequently, PCHEs should not be evaluated specifically on their ability to enhance heat transfer. Practical assessment should also consider whether the selected channel concept can support an acceptable thermal duty, hydraulic resistance, manufacturability, and system-level compatibility.

The studies summarised in Figures 11–13 and in Table 4 demonstrate that the baseline PCHE performance is controlled by three inter-related design levels. The first relates to the cooling concept, which describes the interaction between the heated wall or porous interface and the coolant. The second addresses the overall topology that affects compactness, thermal penetration, flow redistribution, and flow stability. The third involves the local passage shape, which defines the trade-off between the improvement in the Nu, f, wall temperature uniformity, and ΔP. Accordingly, this section considers PCHE design as a coupled thermal–hydraulic problem, as opposed to a simple comparison of individual channel shapes.

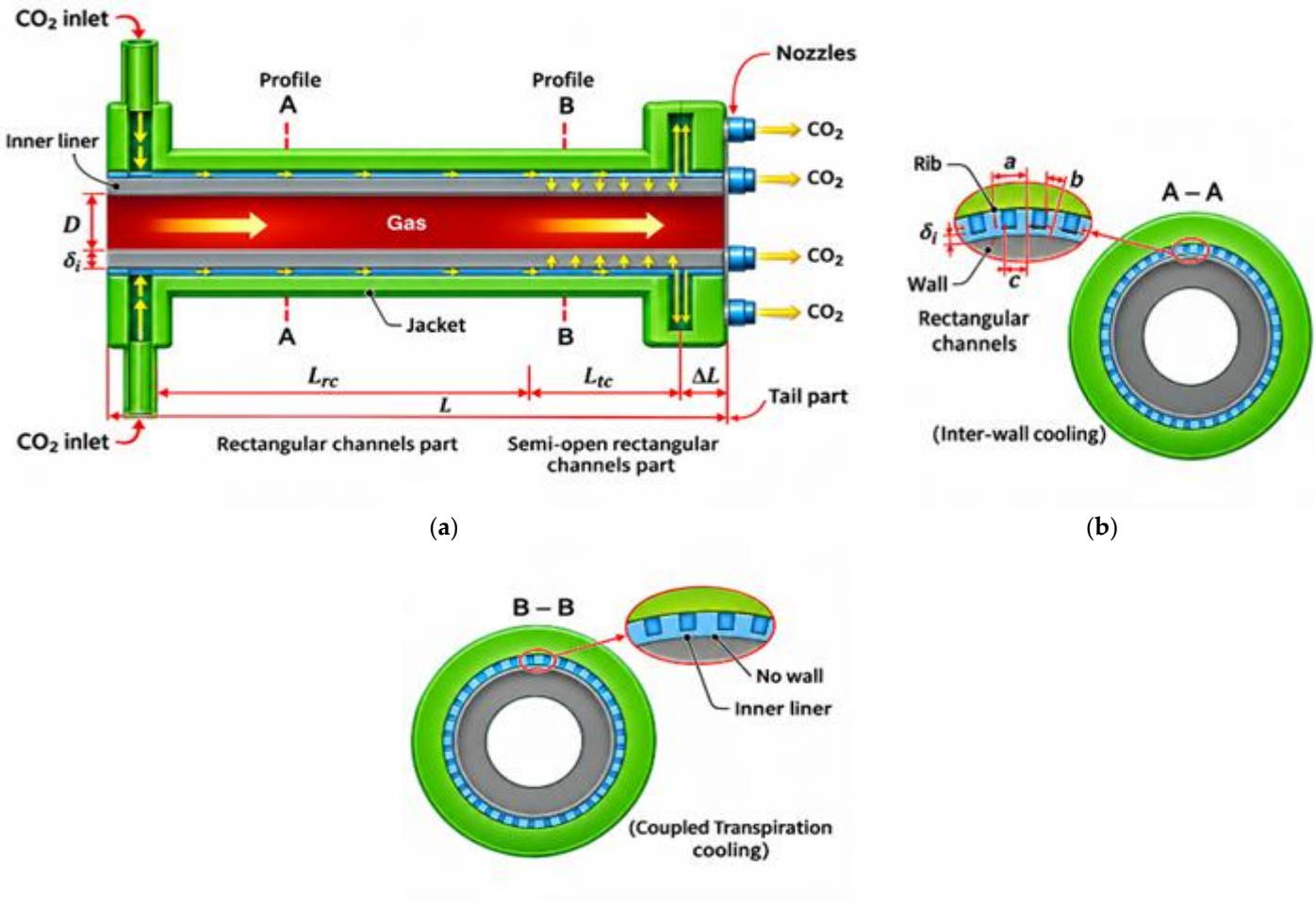


Figure 11. CO_2-cooled chamber: (**a**) longitudinal section; (**b**) section A–A, inter-wall cooling; (**c**) section B–B, coupled transpiration cooling.

3.3.1. Channel Concepts and Baseline Cooling Strategies in PCHE-Type Passages

The baseline cooling strategy is crucial given that it determines how heat is transferred through enhanced convective mixing, coolant redistribution, reduced wall thermal resistance, or through boundary layer modification. Notwithstanding that PCHEs use closed, etched channels instead of porous transpiration concepts, research pertaining to other PCH cooling concepts can provide valuable information on coolant distribution and wall/coolant interactions on thermal protection.

Yuan et al. [55] compared convective and transpiration cooling of sCO_2 in parallel rectangular channels equipped with porous liners, with the mainstream gas flowing at Mach 1–1.5 and temperatures exceeding 2000 K, as shown in Figure 11. The study revealed that coupled transpiration cooling significantly enhanced thermal protection even at lower coolant mass flow rates, while thinner and more porous liners also improved cooling performance. This result should not be taken as direct evidence of the applicability of transpiration cooling to conventional PCHE recuperators or precoolers, as the operating environment is more typical of aerospace thermal protection than of conventional compact heat-exchanger service. Nonetheless, the study is worth mentioning because it demonstrates that, under severe thermal loads, coolant-distribution strategy may be as important as channel geometry.

The design implication for PCHE-type compact passages is that local channel geometry should be evaluated not only by shape, but also by its ability to distribute coolant along the heated surface. The same concept is apparent in practical PCHEs, where flow maldistribution, manifold design, channel blockage, and bends can cause secondary flow and local hot spots. Therefore, local heat transfer enhancement and exchanger-level flow distribution should be considered in the baseline PCHE (B-PCHE) design.

3.3.2. PCHE Topologies for Precoolers and Specialised Compact Thermal Devices

The relationship between compactness, thermal duty, and hydraulic penalty is dependent on PCHE topology. In contrast to simple microchannels, PCHE passages result in other requirements, such as high-pressure integrity, manufacturability, diffusion bonding, flow distribution, and system integration. Accordingly, a topology with better local heat transfer may not be required if it gives rise to high ΔP, non-uniform flow distribution, or if it is too difficult to fabricate.

Ma and Hu [7] demonstrated that a sandwiched zigzag geometry can be superior to a dual-straight geometry, as explained in Figure 12a. The reported design resulted in an increase in heat transfer of 66.7%, a reduction in ΔP of 74.7%, and a decrease in exchanger size of 38.7%. The same arrangement resulted in an 84.6% improvement in thermal capacity and a 68% reduction in size under precooler conditions. The results suggest that the use of contoured compact topologies can enhance thermal duty and compactness, provided that the channel configuration achieves high heat transfer while simultaneously maintaining low flow resistance. It is important to note, however, that the result should be understood in the context of the reported topology and operating window. Zigzag and contoured passages do not necessarily lead to lower ΔP, given that sharper bending angles can increase friction in other topologies and blockage can increase ΔP.

New compact devices demonstrate that topology influences not only steady heat transfer but also dynamic stability and predictability. When the channel size increased from the thermal penetration depth to approximately three to four times the thermal penetration depth, the pressure amplitude rose from 0.419 to 0.455 MPa, whereas the onset-temperature spread decreased from 14.8 °C to 11.2 °C, as reported by Hu and Wang [56] (Figure 12b). This finding implies that the stability of compact devices can vary depending on passage scale, specifically when the thermal penetration length approaches

the channel dimension. Therefore, hydraulic scale must be considered as a design parameter as opposed to geometric detail.

For semi-circular PCHE-like passages, Park and Kim [57] measured mean absolute deviations between 10.5% at the top wall and 17.8% at the bottom wall, as illustrated in Figure 12c. It is significant that the prediction accuracy for the top and bottom walls differs slightly. This suggests that even relatively simple cross-sections, for example, those employed in PCHEs, can generate an asymmetrical response under strong property gradients. As a result, topology selection also affects model reliability and wall temperature prediction.

Together, these studies demonstrate that topology in PCHEs has an influence on more than heat transfer enhancement, as it also regulates compactness, flow stability, wall temperature asymmetry, and predictive model reliability. In engineering design, the optimum topology should be selected based on the dominant design constraint, including thermal duty, ΔP, size reduction, local hot-spot avoidance, or system stability.

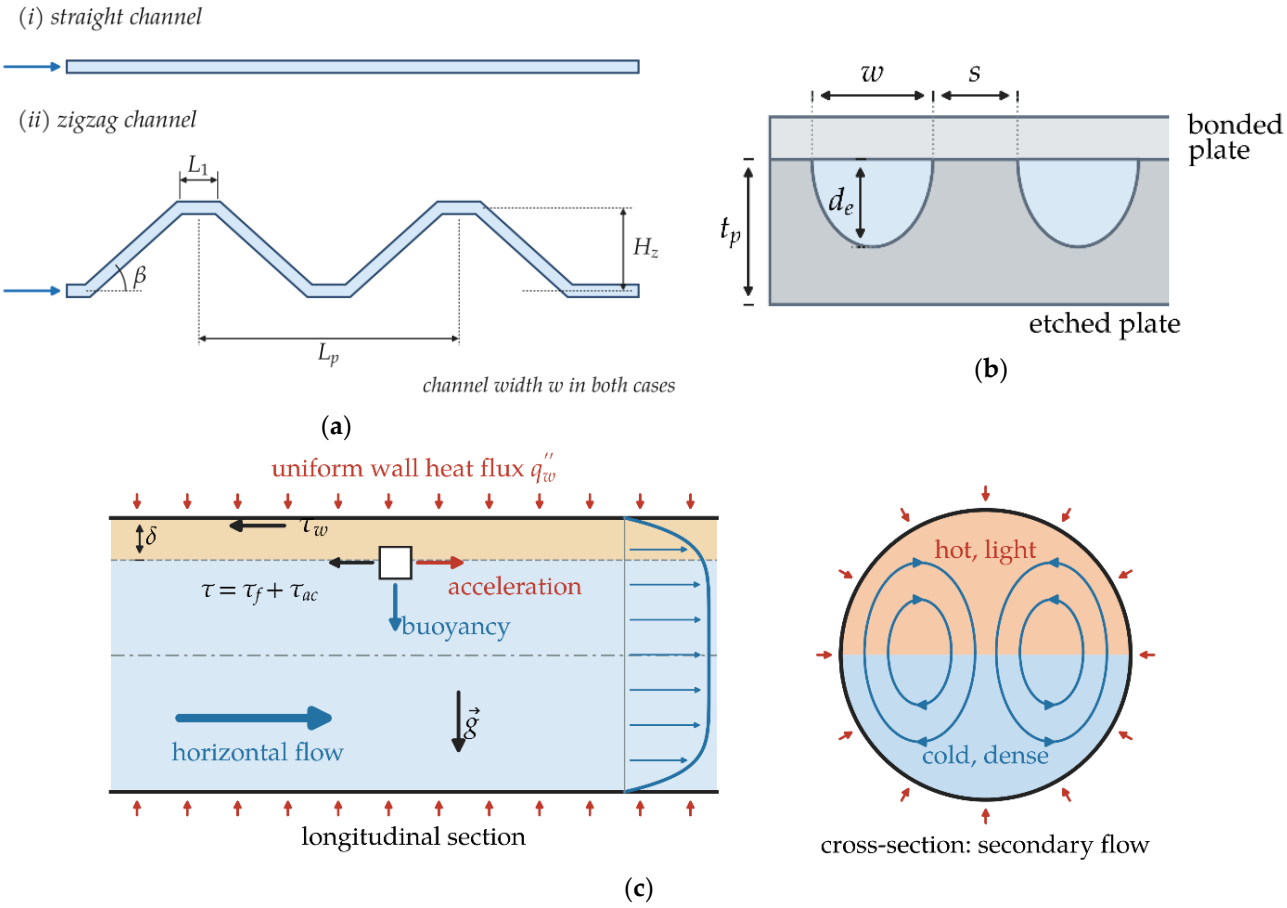


Figure 12. Precooler topologies: (**a**) Ma and Hu [7]; (**b**) Hu and Wang [56]; and (**c**) Park and Kim [57].

3.3.3. Cross-Sectional Shape Effects and Microscale Passage Optimisation

The cross-sectional geometry of PCHE-type passages affects the rate of flow acceleration, the development of near-wall thermal gradients, and the frictional resistance. The reviewed studies indicate that there is no single best geometry used for optimisation. Instead, each geometry demonstrates a trade-off between heat transfer enhancement, ΔP penalty, and wall temperature uniformity.

Li et al. [58] observed an optimum wavy receiver geometry with a wavelength of 15.07 mm and an amplitude of 0.173 mm, with a heat transfer enhancement factor of approximately 1.213, as illustrated in Figure 13a. This finding shows that moderate

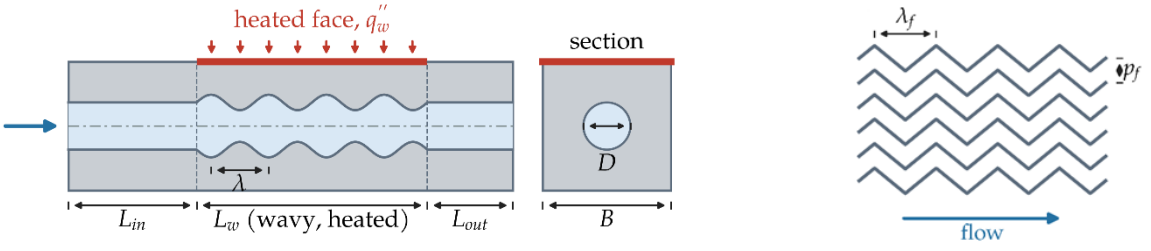
waviness may be employed to enhance thermal performance without requiring significant flow disruption. However, the advantage is dependent on the amplitude and wavelength chosen. Excessive waviness can cause friction to increase more rapidly than heat transfer.

Liu et al. [59] reported heat transfer coefficients approximately twice the Dittus–Boelter predictions and f approximately 7–10 times those of straight channels, as shown in Figure 13b. These comparisons use different reference baselines and therefore do not establish an overall thermal–hydraulic performance advantage. This finding is one of the most obvious examples of the enhancement penalty trade-off in PCHEs. Selection therefore requires a comparison at matched operating conditions and a clearly defined constraint, such as equal pumping power.

This objective-dependent interpretation is supported by comparisons of cross-sectional geometries. Tu and Zeng [60] reported that circular passages demonstrate slightly higher h and ΔP than semicircular passages, while the D_h of the passages reduces both heat transfer and resistance, as shown in Figure 13c. This indicates that there is a limit to the size of the D_h that can be implemented without considering the pumping power requirement. At the microscale, Manda and Peles [8] reported surface heat transfer rates that were 49–55% higher in triangular passages than in circular passages as pressure increased, as illustrated in Figure 13d. Similar results were reported by Zhang et al. [61], who discovered that triangular sections provided the optimum overall performance of 1.075 and a Nu that was roughly 9.8% higher than that of square channels. However, square passages were demonstrated to have lower frictional resistance, as shown in Figure 13e.

The close proximity of the passages in conjunction with a counter-flow configuration and high-conductivity copper walls also supports temperature control, as demonstrated by Zhang et al. [61]. The use of copper walls resulted in an average increase of 16.7% in the h, a decrease of 7.4% in friction, and a reduction of 25.3% in peak wall temperature. This is significant because it shows that PCHE performance is not directly controlled by passage shape. Even with a constant channel geometry, wall material and channel arrangement can help to minimise hot spots and enhance thermal uniformity.

When maximum thermal performance is the primary design objective, triangular-type passages may be beneficial. However, the advantage should not be regarded as universal, as the optimal cross-sectional geometry depends on the thermal–hydraulic requirements and operating conditions. When reducing friction losses, improving manufacturability, or ΔP control are important, square or semicircular passages may provide a more appropriate alternative. The wavy and zigzag passages can increase heat transfer, whilst maintaining a reasonable hydraulic penalty. Accordingly, the cross-sectional shape should be chosen based on the primary design objective, with consideration given to heat transfer duty, ΔP, temperature uniformity, compactness, and ease of manufacture.



(**a**) (**b**)

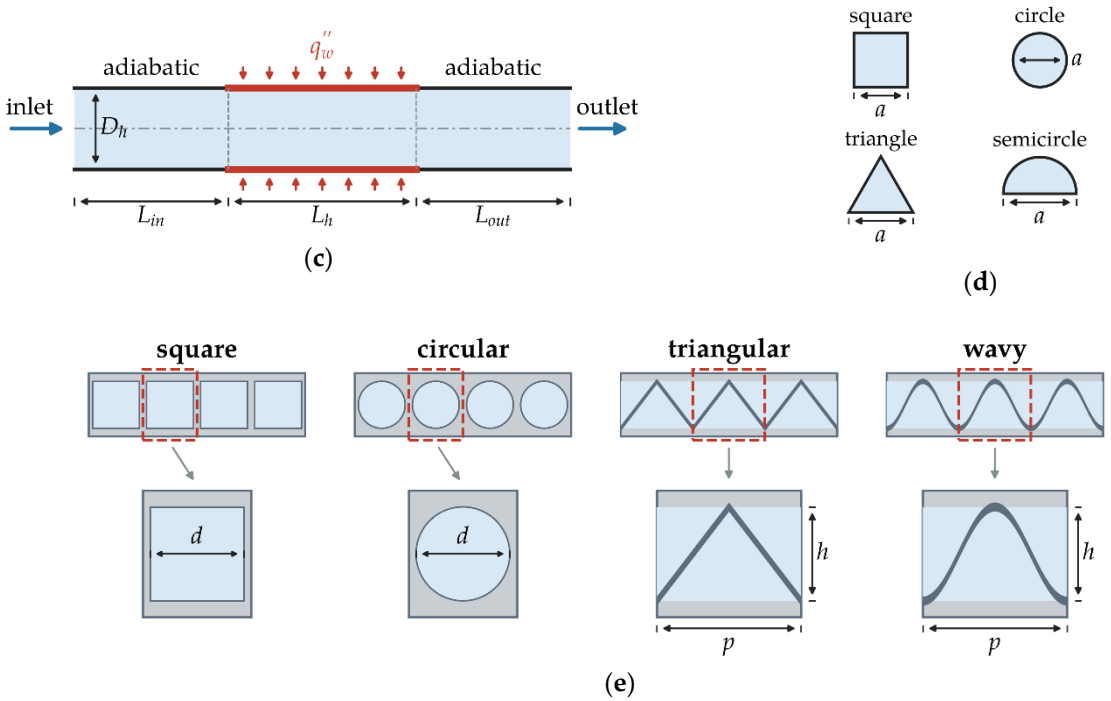


Figure 13. Cross-sectional geometry passages: (**a**) Li et al. [58]; (**b**) Liu et al. [59]; (**c**) Tu and Zeng [60]; and (**d**) Manda et al. [62]; and (**e**) Zhang et al. [61].

Table 4. Important trends in baseline PCHE configurations and compact passage concepts.

Topic	Main Studies	Geometry/Operating Context	Dominant Design Mechanism	Main Quantitative Findings	Design Boundary and Implications
Baseline cooling strategy	Yuan et al. [55]	Parallel rectangular sCO_2 channels with porous liners under supersonic mainstreams, Mach 1–1.5 and T > 2000 K	Coolant redistribution, boundary-layer disruption, porous-wall interaction	Transpiration cooling improved thermal protection even at lower mass flow; thinner and more porous liners increased cooling effectiveness	Useful for investigating coolant-distribution effects under extreme heat load. Not directly transferable to conventional PCHE recuperators without considering pressure loss, manufacturability, and application domain.
PCHE topology	Ma and Hu [7]	Sandwiched-zigzag versus dual-straight compact configurations; precooler application	Topology-induced heat transfer intensification, compactness improvement, flow-path redistribution	Sandwiched-zigzag design increased heat transfer by 66.7%, 74.7% reduction in ΔP, and reduced size by 38.7%. Under precooler conditions, capacity increased by 84.6%, and size decreased by 68%	Contoured layouts can improve duty and compactness; however, performance depends on bend angle, flow distribution, and ΔP constraint.
Specialised compact devices	Hu and Wang [56], and Park and Kim [57]	Passage size comparable to thermal penetration depth; semi-circular PCHE-like passages	Thermal penetration scaling, dynamic stability, wall temperature asymmetry	Increasing channel size to 3–4 times the thermal penetration depth increased pressure amplitude from 0.419 to 0.455 MPa and reduced onset-temperature spread from 14.8 °C to 11.2 °C. Prediction deviations were 10.5% at the top wall and 17.8% at the bottom wall	Passage scale affects both stability and model reliability. Top/bottom wall asymmetry should be considered in PCHE prediction and validation.
Wavy and zigzag passages	Li et al. [58], and Liu et al. [59]	Wavy receiver geometry; zigzag PCHE passages	Secondary flow, boundary-layer redevelopment, bend-induced mixing, increased friction	Optimum wavy geometry: wavelength 15.07 mm, amplitude 0.173 mm, heat transfer factor ≈ 1.213; zigzag h ≈ 2× Dittus–Boelter prediction, with a f ≈ 7–10× that of a straight channel	Selection requires matched operating conditions and a common comparison basis, such as equal pumping power; the reported ratios alone do not establish an overall performance advantage.
Cross-sectional shape	Tu and Zeng [60], Manda et al. [62],	Circular, semicircular, triangular and square passages; microscale compact channels	Shape-controlled wall contact, local acceleration, hydraulic-	Circular passages produced slightly higher h and ΔP than semicircular passages; triangular passages	Triangular passages prioritise thermal performance, whereas square and semicircular passages may offer lower

	and Zhang et al. [61].		diameter effect, friction generation	delivered 49–55% higher heat transfer than circular passages; triangular section reached $\eta \approx 1.075$ and Nu +9.8% compared with square channels	friction or easier fabrication. Shape selection must adhere to the design objective.
Wall and flow arrangement effects	Zhang et al. [61].	Counter-flow neighbouring channels and copper wall arrangement	Improved wall conduction, thermal redistribution, hot-spot suppression	Copper walls increased average h by 16.7%, reduced friction by 7.4% and lowered peak wall temperature by 25.3%	Material and neighbouring-channel arrangement can improve thermal uniformity independently of local passage shape. Important for hot-spot control in compact PCHEs.

3.4. Performance Enhancement and Flow-Distribution Optimisation in PCHEs

The second design challenge is to increase the local h, whilst maintaining the improvement at the exchanger level. In PCHEs, local channel modifications, fin shape, bend structure, manifold and header design, and the flow-path topology are strongly coupled. Local mixing that is improved by geometry may produce a ΔP penalty, excessive blockage, flow maldistribution or local hot spots if these effects are not tolerated at the system level.

The studies summarised in Figures 14–16 and Table 5 demonstrate three levels of PCHE performance enhancement. The first is local passage enhancement, entailing fins and airfoil-type structures which modify the mixing and boundary-layer redevelopment characteristics locally. The second refers to the optimisation of flow distribution, which involves headers, manifolds, bypass routes, and channel arrangement. This establishes how local flow enhancement is distributed evenly throughout the exchanger. The third is topology optimisation, which involves optimising the entire flow path to maximise heat transfer, temperature matching, and hydraulic performance. Therefore, PCHE optimisation is considered a multiscale design issue, which goes beyond local channel-shape optimisation.

3.4.1. Finned and Airfoil-Shaped Passages for PCHE Performance Enhancement

Finned and airfoil-shaped PCHE passages are designed to enhance heat transfer by promoting local mixing, disrupting the boundary layer, and increasing the effective heat transfer area. However, their performance is dependent upon the trade-off between mixing enhancement and blockage-induced pressure loss. Fins that are too thin are less effective at promoting flow redevelopment, while fins that are too thick or dense result in excessive form drag and flow obstruction, which may offset the thermal gain. Consequently, the best fin geometry is not invariably the most flow-disturbing, but the geometry that delivers satisfactory mixing at a reasonable hydraulic cost.

Li et al. [63] determined that the hybrid airfoil/fin channels exhibited maximum performance when transverse spacing, longitudinal spacing, and stagger spacing were 2 mm, 10 mm, and 4 mm, respectively, as illustrated in Figure 14a. In these conditions, performance was enhanced by approximately 2.8–13.2% above the baseline. The outcome suggests that the spacing between the airfoils is fundamental for optimisation, as wake interaction, local redevelopment, and frictional resistance depend on spacing.

Li et al. [64] also observed that increasing fin thickness improved heat transfer, but reduced the flow area and increased flow resistance, as presented in Figure 14b. In terms of the overall performance measure, Fin-5, Fin-6, and Fin-13 outperformed Fin-3 by around 6.3%. This comparison supports the viewpoint that fin thickness should be optimised as opposed to maximised. Increasing fin thickness increases surface heat transfer. However, the associated increase in flow disturbance is accompanied by greater blockage and flow resistance, which can eventually reduce the thermo–hydraulic benefit in general.

The studies presented here demonstrate that airfoils and fin-based passages are effective when moderate heat transfer enhancement with a controlled ΔP is required. The advantage is that they can provide more gradual flow acceleration and lower wake losses than more abrupt ribbed or zigzag structures. Nevertheless, their effectiveness is geometry-dependent and must be evaluated from a thermal–hydraulic viewpoint instead of by way of heat transfer enhancement.

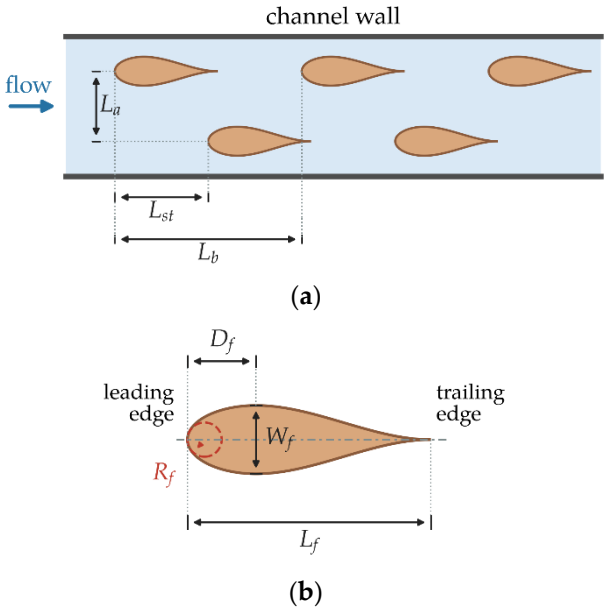


Figure 14. Fin and airfoil designs: (**a**) Li et al. [63]; and (**b**) Li et al. [64].

3.4.2. Manifold, Header, and Flow-Route Optimisation in PCHE Systems

PCHE performance is highly influenced by the distribution of flow at the exchanger level. Even if each channel is well optimised, the same effects can result from poor header or manifold design. Therefore, channel and header optimisation should be regarded as a coupled design problem.

Khoshvaght-Aliabadi et al. [65] showed that the combined channel-routing strategy was effective in improving thermal and hydraulic performance, as depicted in Figure 15a. The configuration featured converged cold-side water channels and diverged hot-side CO_2 channels, which resulted in better thermal performance and a CO_2-side ΔP reduction of around 60%. The outlet temperatures under far-critical, near-critical, and trans-critical operating conditions were recorded as 310.2 K, 299.9 K, and 291.6 K, respectively. This finding is significant not only because it demonstrates the potential for channel routing to modify local heat transfer, but also to modify the pressure loss and sensitivity of the heat transfer to the operating conditions.

Zilio et al. [66] assessed 37 heat transfer correlations for straight and zigzag PCHE channels, as depicted in Figure 15b. Their largest reported total mean heat transfer-rate prediction error, 84.03%, occurred when Nikitin et al.'s [67] correlations were applied to water-to-water experimental data for 90° square zigzag channels. This comparison involved different fluids and geometries from those used to develop the correlations. The result therefore highlights limitations in transferring correlations beyond their calibration conditions and should not be interpreted as a general error bound for near-critical sCO_2 prediction.

In the zigzag precooler with bypass, Ahmed and Ehsan [68] investigated how the inlet water temperature and sCO_2 pressure could be reduced to increase heat transfer, as illustrated in Figure 15c. The result shows that exchanger-level performance depends not only on geometry-dependent factors, but also on other operating-boundary conditions and flow routing conditions. Jin et al. [69] established that modified headers could enhance thermo–hydraulic performance by about 5% and 8.5% over free and straight-rib headers, respectively. Additionally, the reported decrease in flow non-uniformity shows the significance of header design in addition to channel design in achieving stable exchanger operation.

The results in Figure 15 confirm that PCHE optimisation cannot be separated into PCH and manifold optimisation. Without effective flow distribution, a high-performance channel can be detrimental to the system. Conversely, a well-designed header can improve the use of the heat transfer area without implementing substantial channel modifications. Accordingly, the co-design of the header and channel is crucial for stable, predictable, and effective PCHE operation.

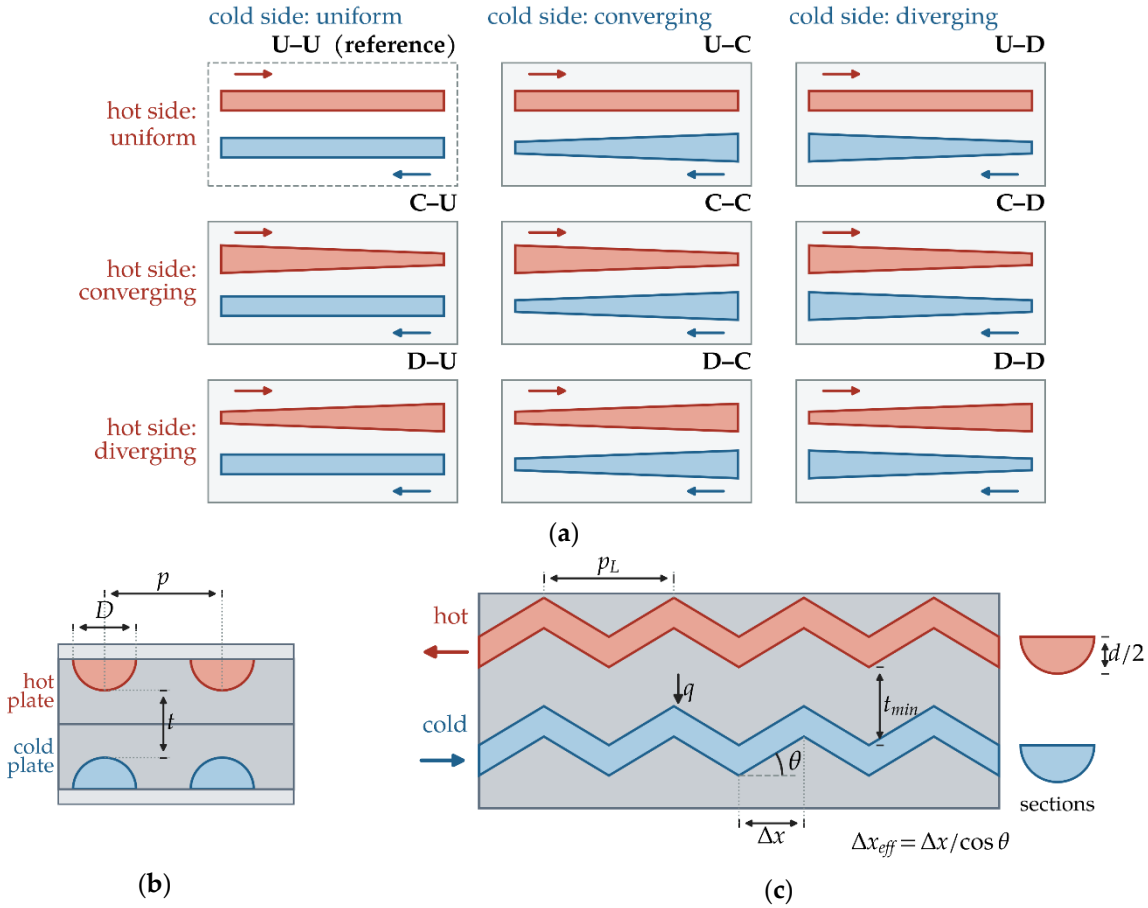


Figure 15. Proposed designs: (**a**) Khoshvaght-Aliabadi et al. [65]; (**b**) Zilio et al. [66]; and (**c**) Ahmed and Ehsan [68].

3.4.3. Topology-Optimised PCHEs and Enhanced Compact Passages

Topology optimisation is regarded as a more advanced approach to PCHE design, given that it considers more than modifying parameters, such as fin thickness, bend angle, or channel spacing. Conversely, this approach alters the complete flow path to increase heat transfer, temperature matching, turbulence generation, and pressure distribution simultaneously. This is particularly applicable in the case of sCO_2 systems where significant property gradients in the vicinity of the pseudo-critical region cause local thermal and hydraulic responses to be highly dependent on the flow-path design.

Li and Liu [70] confirmed that topology optimisation is capable of optimising several performance indices simultaneously, as illustrated in Figure 16. The topology generated using CO_2 properties at 315 K increased the overall heat transfer coefficient, U, by 18.8% and reduced the minimum temperature pinch by 48.8% relative to the original straight-channel model. The comparison used a CO_2 inlet temperature of 313.72 K, a water inlet temperature of 298.15 K, and respective mass flow rates of 0.023 and 0.020 kg/s at a reported operating pressure of 8.85 MPa. Additionally, turbulent kinetic energy increased by about 1.27× whilst reducing the CO_2-side ΔP by almost 55% compared with the straight-

channel baseline. This finding is important given that it indicates that some of the drawbacks associated with local enhancement methods can be overcome through full flow-path redesign. For the investigated conditions, topology optimisation improved the overall heat transfer coefficient while reducing the CO_2-side pressure difference by approximately 55.2% relative to the original straight-channel model.

However, it is essential that topology-optimised PCHEs be thoroughly assessed prior to use. Their performance is dependent on manufacturability, etching feasibility, diffusion-bonding limitations, mechanical integrity at high pressure, and the reliability of the optimised design under off-design conditions. A topology that is optimised for a specific design temperature or mass-flow rate in practical systems may not deliver the same benefits when the operating point changes. Therefore, topology optimisation should be combined with mechanical assessment, ΔP constraints, and off-design performance assessment.

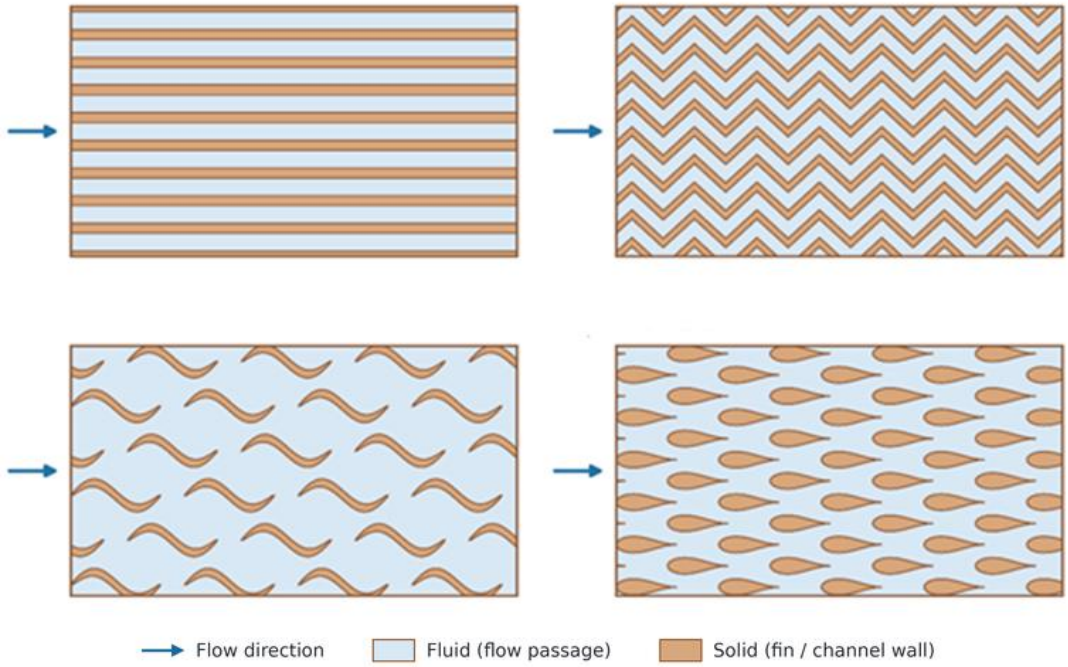


Figure 16. Optimised PCHE proposed by Li and Liu [70].

3.5. Passive Enhancement Strategies for sCO_2 Cooling

In passive enhancement strategies for sCO_2 compact cooling passages, near-wall mixing is enhanced, buoyancy stratification is reduced, HTD is prevented, and wall temperature uniformity is achieved in the absence of active flow control. Nonetheless, the reviewed studies specify that passive enhancement should not be evaluated only on the basis of the magnitude of the heat transfer enhancement. Structures that promote mixing and boundary-layer redevelopment may also increase frictional resistance and form drag and manufacturing complexity. Their influence on dynamic flow stability requires separate evidence from experiments or transient simulations. Thus, instead of asking whether passive enhancement can increase heat transfer, the question is: What structure provides the most acceptable compromise between heat transfer gain, ΔP penalty, wall temperature control, and operational stability under near-critical sCO_2 conditions?

Table 5. Important trends in PCHE performance enhancement and flow-distribution optimisation.

Topic	Main Studies	Design Level/Operating Role	Dominant Mechanism	Main Quantitative Findings	Design Boundary and Implications
Fin and airfoil shaping	Li et al. [63], and Li et al. [64].	Local passage enhancement through airfoil fins and fin-thickness optimisation	Boundary-layer redevelopment, controlled wake mixing, flow-area blockage	Hybrid airfoil-fin channels improved performance by 2.8–13.2%; optimal transverse, longitudinal and stagger spacings were 2 mm, 10 mm and 4 mm; optimised fins improved overall performance by ~6.3%.	Fin geometry should balance mixing enhancement with blockage-induced losses. Airfoil fins are suitable for moderate enhancement when ΔP control remains important.
Flow-route and channel arrangement	Khoshvaght-Aliabadi et al. [65]	Coupled hot-side/cold-side channel routing in compact heat exchanger operation	Flow redistribution, area variation, ΔP reduction, operating-condition control	CO_2-side ΔP was reduced by ~60%; outlet temperatures were 310.2 K, 299.9 K and 291.6 K under far-critical, near-critical and trans-critical conditions.	Channel routing can improve both thermal duty and hydraulic performance; however, the benefit depends on operating regime and hot/cold-side coupling.
Correlation reliability in PCHEs	Zilio et al. [66]	Predictive assessment for straight and zigzag PCHE-type channels	Geometry-induced deviation from conventional Nu correlations	Maximum total mean heat transfer-rate prediction error of 84.03% when Nikitin et al.'s correlations were applied to water-to-water data for 90° square zigzag channels.	Correlation transfer requires compatible fluids, geometries, and operating ranges. The reported maximum error does not establish a general prediction limit for near-critical sCO_2.
Operating-condition and bypass effects	Ahmed and Ehsan [68]	Zigzag precooler with bypass under varied water-inlet temperatures and sCO_2 pressures	Boundary-condition sensitivity, bypass-controlled thermal matching	Lower water-inlet temperature and lower sCO_2 pressure enhanced heat transfer in the zigzag precooler with bypass.	PCHE performance depends on channel geometry and operating boundary conditions. Bypass and inlet conditions should be included in design assessment.
Header optimisation	Jin et al. [69].	Manifold/header-level flow-distribution control	Reduction of flow maldistribution, improved channel utilisation	Modified headers improved thermo–hydraulic performance by ~5% and 8.5% compared with free and straight-rib headers; flow non-uniformity was reduced by 39.4% and 61.8%.	Header/channel co-design is essential for stable exchanger performance. Optimised header designs can reduce hot spots and improve heat transfer-area utilisation.
Topology optimisation	Li and Liu [70]	Full flow-path optimisation of PCHE geometry	Simultaneous enhancement of mixing, temperature matching, turbulence generation and pressure redistribution	Overall, U increased by 18.8%; temperature pinch reduced by 48.8%; turbulent kinetic energy increased by ~1.27×; CO_2-side pressure difference reduced by ~55%.	Full flow-path optimisation can outperform local geometric refinement; however, manufacturability, mechanical integrity and off-design robustness must be assessed.

The studies summarised in Figures 17 and 18 and Table 6 suggest that passive enhancement can be categorised into three design families. The first are ribbed, concave, grooved, and textured surfaces, with near-wall flow reorganisation as the dominant mechanism. The second consists of obstacle-type structures, for example, pin fins, airfoil obstacles, and mini-ribs. The objective is to increase the mixing and decrease the peak wall temperature. The third is made up of inserts, lattices, and additively manufactured roughness, where the enhancement is more three-dimensional and can be used explicitly to suppress thermal stratification and HTD. Therefore, these structures could be evaluated differently depending on the objective. In the case of a structure where ΔP must be controlled, mild surface texturing is attractive, whereas in the case of a structure where the main objective is to control thermal non-uniformity or to mitigate HTD, tapes and lattices are more appropriate.

3.5.1. Surface Texturing and Obstacle-Based Enhancement

Surface texturing and local obstacles are effective in enhancing surface cooling by secondary flow reorganisation, near-wall thermal layer disturbance, and renewal of the heated-wall region. A significant advantage is that they can deliver measurable heat transfer enhancement without a complete redesign of the flow passage. However, their effectiveness depends on whether the additional mixing outweighs the friction penalty.

Under non-uniform heating, Zhang et al. [16] established that local ribs and concaves increased the h by 25.61% and f by 11.81%, as depicted in Figure 17a. These percentages describe changes in different quantities and do not, by themselves, establish a net thermo–hydraulic benefit. Such an assessment requires a defined performance criterion and consistent comparison conditions. Consequently, concave or ribbed surfaces can be useful when their geometry is optimised to redirect the near-wall thermal layer without leading to significant blockage.

Wang et al. [71] proved that spiral grooves can promote annular heat transfer, as demonstrated in Figure 17b. Amongst the tested designs, the six-start circular-arc groove achieved the best performance, with an average channel h of 2538 W/m^2 K and an evaluation factor of 2.03. This finding indicates the potential to improve thermal performance through the introduction of rotational or swirling flow components that improve the fluid renewal close to the wall by means of groove geometry. Nonetheless, this benefit is geometry-dependent, as the balance between secondary-flow generation and frictional losses depends on the groove number, angle, curvature, and depth.

Fins, pin fins, airfoil obstacles, and mini-ribs provide more aggressive augmentation. As shown in Figure 17c, Liu et al. [72] reported that pin-fin channels enhanced the h by 3.08 times compared with plain channels, while decreasing the peak surface temperature by approximately 36–37% and attaining a thermal-performance factor of 1.84 at Re = 45,000. This reveals that pin fins are particularly effective for cooling applications where the limiting design parameter is maximum surface temperature in conjunction with high q″ conditions. However, pin-fin enhancement leads to additional form drag and consequently should be assessed with respect to thermal performance and not simply heat transfer enhancement.

Kumar et al. [73] confirmed that airfoil obstacles can enhance thermal–hydraulic performance when optimised spacing and chordwise dimensions are employed, as depicted in Figure 17d. This result is consistent with previous PCHE fin studies, which documented that airfoil-type structures do not necessarily impede flow, but can support controlled mixing that reduces wake losses in contrast to blunt obstacles. As illustrated in Figure 17e, Zeng et al. [74] demonstrated that mini-ribs could generate an enhancement factor of around 1.73 and a thermal-performance factor of approximately 1.43 under high

thermal loads. Nevertheless, a height-to-pitch ratio of 10 could reduce the maximum wall temperature by 27.57%.

In general, surface texturing and obstacle-based enhancement are particularly well suited to wall temperature control or local HTD suppression as opposed to minimising pumping power, as illustrated in Figure 17. Pin fins and mini-ribs provide greater heat transfer enhancement and cooling power. However, pin fins require rigorous ΔP analysis, whereas mini-ribs require more stringent ΔP control.

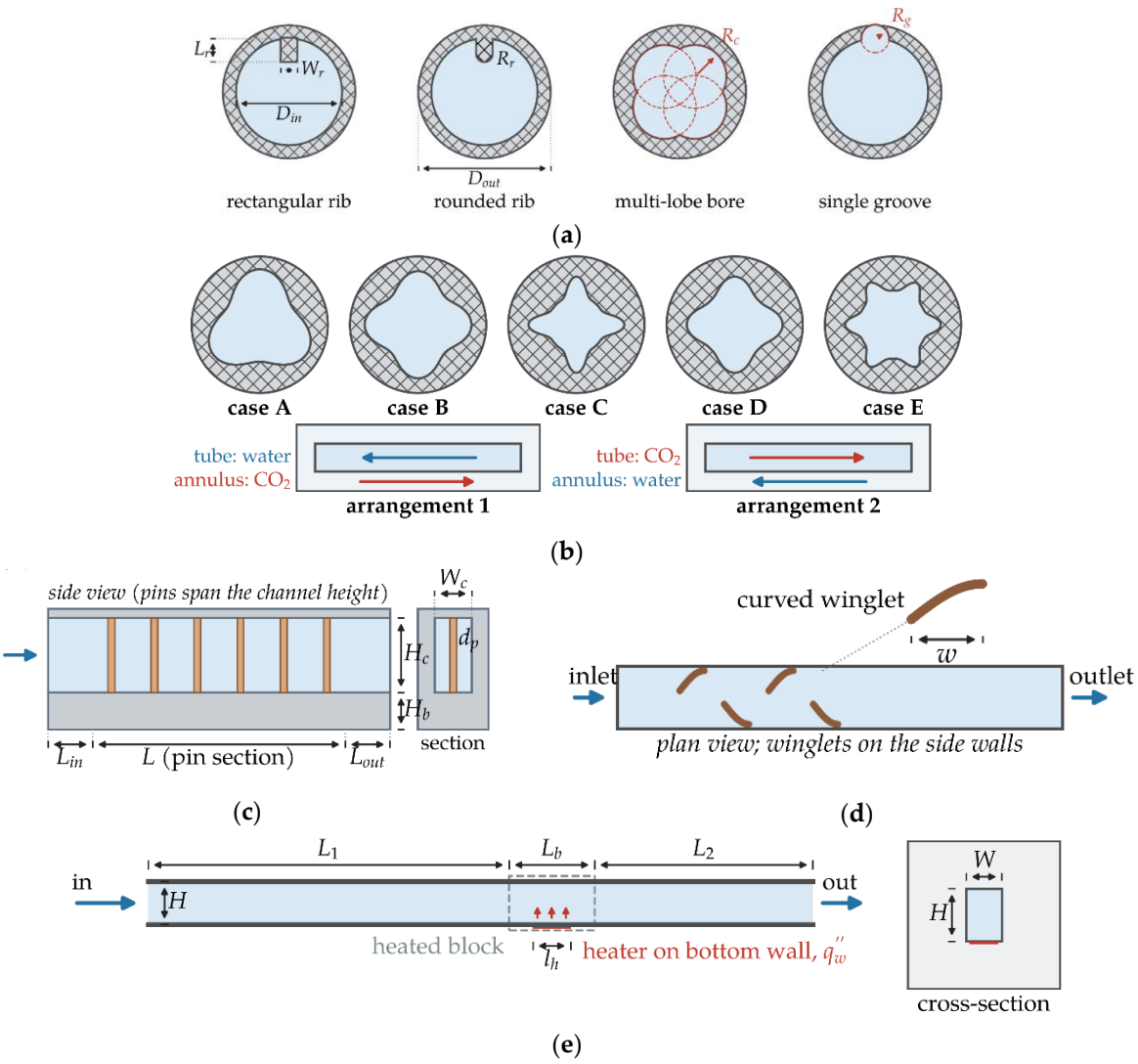


Figure 17. Flow reorganisation: (**a**) Zhang et al. [16]; (**b**) Wang et al. [71]; (**c**) Liu et al. [72]; (**d**) Kumar et al. [73]; and (**e**) Zeng et al. [74].

3.5.2. Inserts for Stratification Suppression and HTD Mitigation

For three-dimensional mixing, surface texturing is not as effective as internal inserts and lattice structures. The main advantage associated with using these structures is not only the enhancement of the average h, but also the suppression of circumferential thermal non-uniformity, disruption of buoyancy-driven stratification, and reduction of local wall temperature peaks. This is particularly important for sCO_2 cooling under high q″ and near-pseudocritical conditions. The drawback is that these structures generally result in a greater ΔP penalty and require comprehensive geometric optimisation.

Li et al. [75] established that the friction ratio for twisted tubes in tube-in-tube cooling was approximately 3.63–7.29, the Nu ratio about 3.43–5.75, and the COP approximately 1.90–2.94, as shown in Figure 18a. Most studies indicated that a twist ratio of 3.78 generally

provided the best thermo–hydraulic behaviour. The results demonstrate that twisted tapes are not low-resistivity enhancement devices. Conversely, they are effective when the ΔP is acceptable and improved heat transfer and cross-sectional mixing are required.

Under optimal conditions, Li et al. [76] demonstrated that twisted tapes can minimise the circumferential thermal non-uniformity by up to 95.7%, attaining a PEC of roughly 1.81 and an average improvement in performance of ~203%, as depicted in Figure 18b. With respect to HTD mitigation, this finding is significant because it indicates that inserts can address an underlying problem associated with smooth tubes and channels, where local heat transfer degradation can occur, even if the average h is acceptable. Therefore, twisted tapes are desirable when thermal stability is considered more important than minimising ΔP.

For even greater 3D mixing, lattice inserts should be employed. For claw-shaped arrays investigated by Wang et al. [77], the peak wall temperature was reduced by approximately 40 K, whereas the minimum local h increased by approximately 937 W/m^2 K (see Figure 18c). For vertical lattices investigated by Xiang et al. [78], turbulent kinetic energy increased approximately fivefold; this finding alone does not establish the effect on system-level dynamic stability, as seen in Figure 18d. Circular-tetrahedral lattices reported by Liu et al. [79] revealed one of the highest enhancement levels, with the peak wall temperature reduced by 52.5% from 1495 K to 711 K and increasing the Nu to 3.78–11.49 times that of the reference case. The performance factor was approximately 2.65, as presented in Figure 19a.

The results of these lattices demonstrate that three-dimensional inserts can be more effective than texturing for HTD suppression, wall temperature reduction, and high q″ thermal protection. Nonetheless, these structures can also incur high friction penalties, cause local recirculation, and create manufacturing challenges. Consequently, lattice enhancement is most appropriate in applications where thermal protection is more important than minimum pumping power, for example, high q″ regenerative cooling and compact devices with restrictive wall temperature constraints.

For high-speed flight cooling applications with q″ equal to ~5 MW/m^2, Xu et al. [80] confirmed that mini-ribs improved heat transfer, achieving an enhancement factor of ~1.73 and a thermal-performance factor of ~1.43, as shown in Figure 19b. Moreover, a pitch-to-rib-height ratio of 10 reduced the maximum wall temperature by 27.57%. Furthermore, channels with higher wall conductivity reduced entropy and temperature gradients, supporting the implementation of sCO_2 in scramjet regenerative systems while acknowledging friction increases and the requirement to manage buoyancy near the critical region.

Another enhancement path is provided by additively manufactured rough surfaces, which can be fabricated as part of the channel surface rather than as an insert. Zhao et al. [81] compared the surface roughness of a smooth machined tube to an SLM-printed tube, revealing that the surface roughness increased from about 6.4 to 23.4 μm, as presented in Figure 19c. This increased the Nu by around 126–234% and the friction by approximately 120–297%, with PEC values of around 1.60–2.53. Consequently, Additive Manufacturing (AM) roughness provides an enhancement, although it is not hydraulically free. Its appropriateness depends on the preference for integrated roughness compared with more complex inserts and on the acceptable ΔP.

In particular, Figures 18 and 19 show that inserts, lattices, and AM roughness are extremely effective HTD-mitigation systems; however, their design must be limited by friction, manufacturability, and stability considerations. Twisted tapes are suitable for circumferential stratification suppression, lattice inserts are appropriate for severe wall temperature reduction, and AM roughness is suitable for wall temperature reduction with integrated enhancement instead of separate inserts.

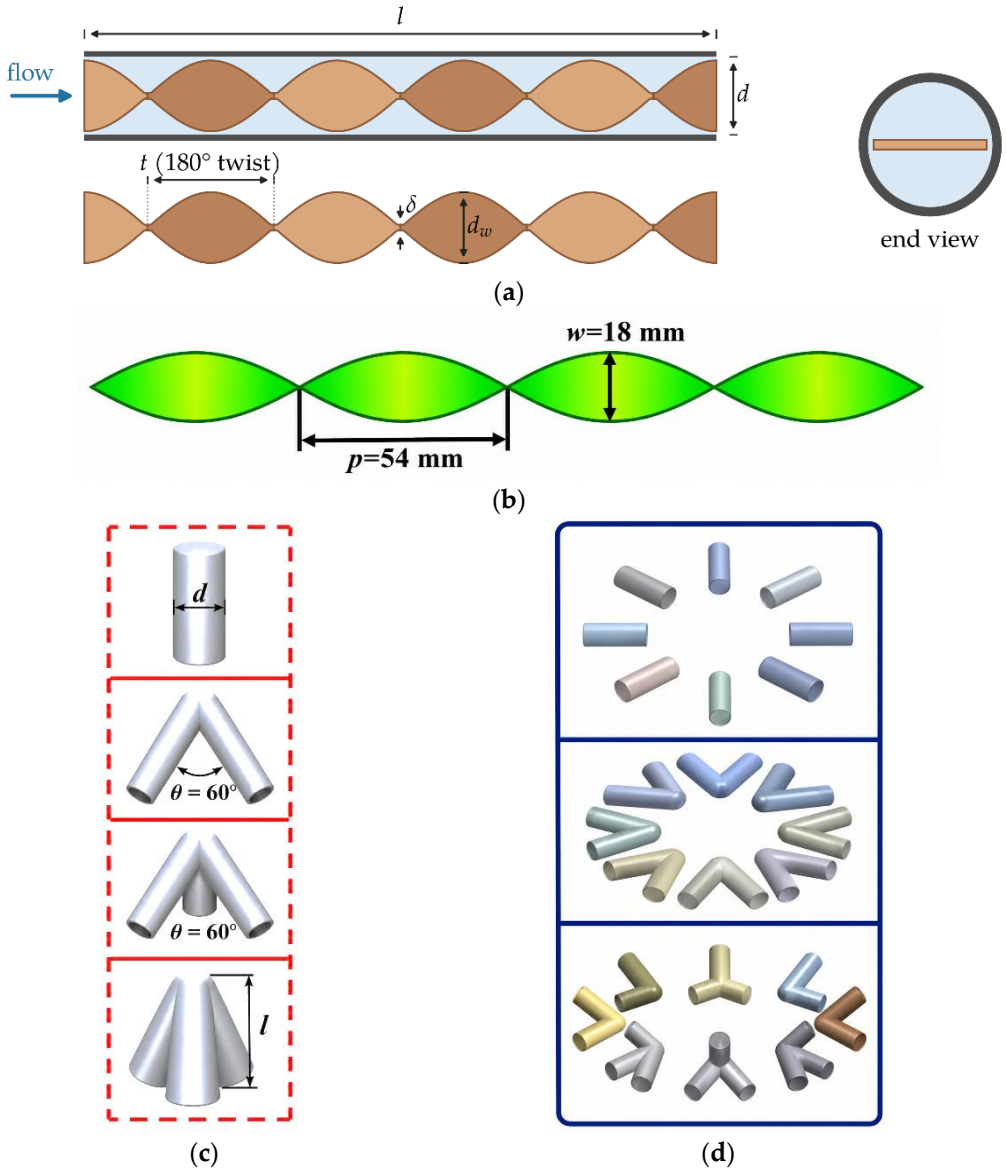
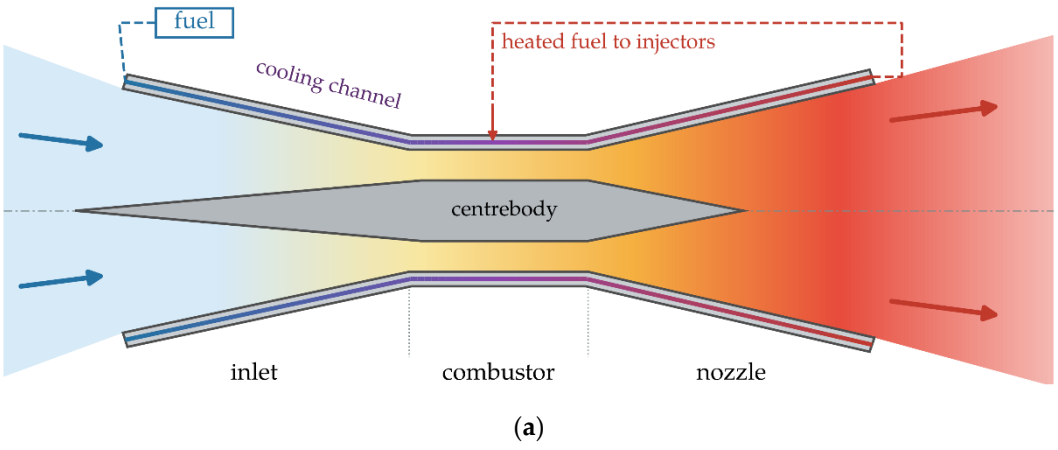


Figure 18. Twisted-tape and lattice enhancements: (**a**) Li et al. [75]; (**b**) Li et al. [76]; (**c**) Wang et al. [77]; and (**d**) Xiang et al. [78].



(**a**)

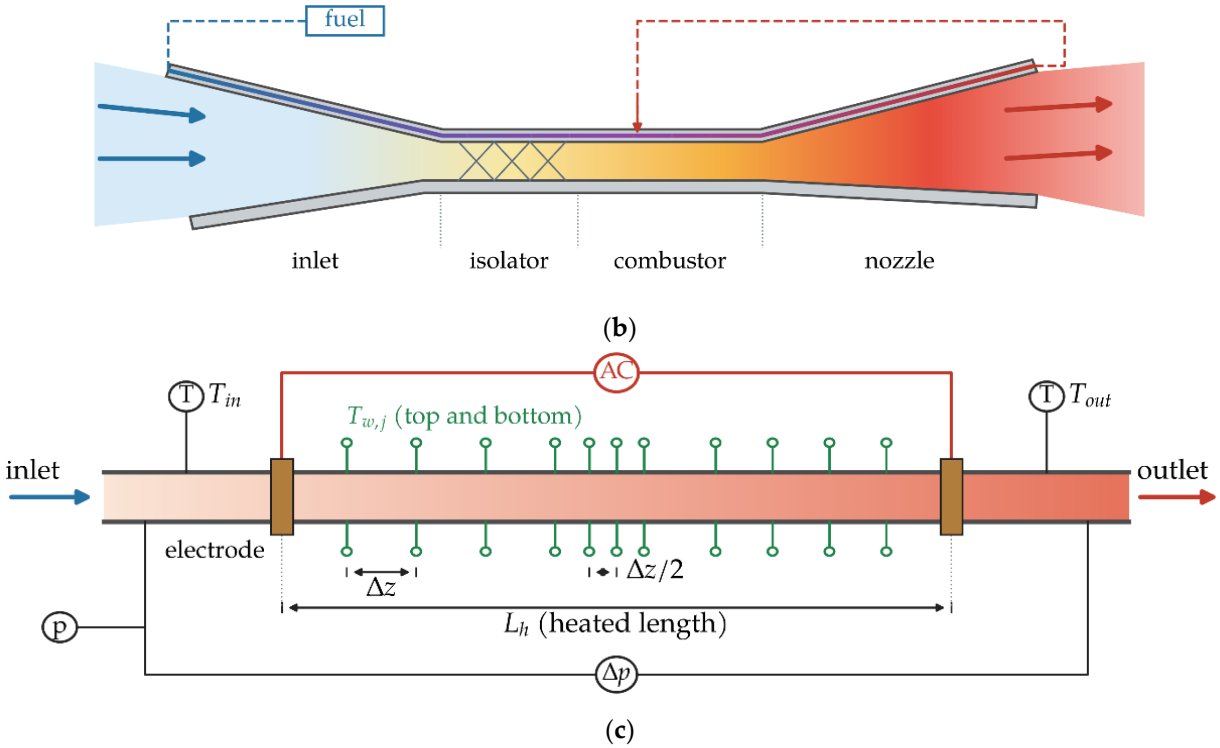


Figure 19. Lattice structures, mini-ribs, and additively manufactured roughness: (**a**) Liu et al. [79]; (**b**) Xu et al. [80]; and (**c**) Zhao et al. [81].

3.6. Application-Specific, Coupled-System, and Dynamic Operating Considerations

The previous sections addressed geometry, passive enhancement, PCHE topology, and optimisation of flow distribution. However, application-specific constraints that cannot be expressed only through local heat transfer and ΔP criteria also inhibit the feasibility of compact sCO_2 heat exchangers. The geometry that may be considered optimum under steady laboratory conditions may not be the most appropriate choice for a practical system owing to factors such as material compatibility, working fluid composition, liquid metal coupling, exchanger duty, plant-level economics, and dynamic operating conditions.

The studies reviewed in Figure 20 and Table 7 show that there are four levels of application-specific design constraints. The first is the material/fluids interface, where corrosion, oxidation, and fluid/material compatibility are important in terms of durability. The second is the formulation of the working fluid, in which mixtures can help to enhance thermal performance; however, they can also contribute to increased pressure loss. The third refers to coupled-system integration, where the exchanger has to meet duty-specific and plant-level requirements. The fourth concerns dynamic operation, under which the relative importance of various channel geometries could change with rolling motion or transient operating conditions. Therefore, application-specific PCHE designs should be evaluated beyond local thermo–hydraulic performance, with consideration given to durability, stability, predictability, and system integration. Material Compatibility, Working-Fluid Composition and Coupled Liquid-Metal/sCO_2 Systems.

Table 6. Important trends in passive enhancement strategies for sCO_2 cooling.

Enhancement Type	Main Studies	Dominant Mechanism	Main Quantitative Findings	Hydraulic/Stability Penalty	Design Boundary and Implications
Ribbed, concave and grooved surfaces	Zhang et al. [16], and Wang et al. [71]	Near-wall flow reorganisation, local boundary-layer disruption, secondary-flow generation	h increased by 25.61% with 11.81% friction penalty; six-start circular-arc spiral groove gave average h ≈ 2538 W/m² K and evaluation factor ≈ 2.03	Moderate friction increase depending on rib/groove geometry	Suitable for moderate enhancement and wall temperature control when ΔP penalty must remain limited.
Pin fins and airfoil obstacles	Liu et al. [72], and Kumar et al. [73]	Enhanced mixing, wake interaction, increased surface area, controlled flow disturbance	Pin-fin channels increased heat transfer by 3.08×; maximum wall temperature reduced by 36–37%; thermal-performance factor reached 1.84 at Re = 45,000	Increased form drag and ΔP; optimum depends on spacing and chordwise dimensions	Useful for high q″ cooling and peak-temperature suppression; however, must be optimised using combined thermal–hydraulic metrics.
Mini-ribs	Zeng et al. [74]	Near-wall mixing, heat transfer from wall region to core, suppression of local hot spots	Enhancement factor ≈ 1.73; thermal-performance factor ≈ 1.43; pitch-to-height ratio of 10 reduced maximum wall temperature by 27.57%	Additional friction; pitch/height ratio effectively controls net benefit	Suitable when maximum wall temperature reduction is more important than minimum friction loss
Twisted tapes	Li et al. [75], and Li et al. [76]	Swirl generation, cross-sectional mixing, suppression of circumferential stratification	Friction ratio 3.63–7.29; Nu ratio 3.43–5.75; COP 1.90–2.94; thermal non-uniformity reduced by up to 95.7%; PEC ≈ 1.81	High friction penalty; twist ratio controls performance	Highly effective for HTD and stratification mitigation when thermal stability is prioritised over ΔP minimisation.
Lattice inserts	Wang et al. [77], Xiang et al. [78], and Liu et al. [79]	Three-dimensional mixing, turbulence generation, boundary-layer interruption, hot-spot suppression	Peak wall temperature reduced by 40–57 K; turbulent kinetic energy increased by ~5×; peak wall temperature reduced by 52.5% in circular-tetrahedral lattices; Nu increased by 3.78–11.49×; overall performance factor ≈ 2.65	Potentially high friction and manufacturing complexity; dynamic stability requires separate assessment	Strongest option for severe HTD mitigation and high q″ thermal protection; however, requires careful optimisation of density and ΔP.
Additively manufactured roughness	Zhao et al. [81]	Distributed roughness-induced turbulence and wall-layer disruption	Roughness increased from 6.4 to 23.4 μm; Nu increased by 126–234%; friction increased by 120–297%; PEC = 1.60–2.53	Significant friction increase; regime-dependent benefit	Useful for integrated enhancement in AM channels; however, should be evaluated against planned inserts and ΔP constraints.

3.6.1. Material Compatibility, Working-Fluid Composition and Coupled Liquid-Metal/sCO$_2$ Systems

Material compatibility introduces an additional design constraint in LBE–sCO$_2$ heat exchangers. Liao et al. [82] coupled an oxidation–corrosion model with CFD to investigate a martensitic-steel PCHE containing straight semicircular passages, with LBE on the hot side and sCO$_2$ on the cold side. Their simulations identified sharp corners as locations susceptible to severe corrosion, as illustrated in Figure 20a. These findings concern LBE-side material interaction under the investigated conditions and should not be interpreted as a general assessment of corrosion on both fluid sides.

Oxygen chemistry is central to interpreting these results. The OECD/NEA handbook explains that oxygen control in lead-alloy systems must maintain conditions that support protective oxide formation while avoiding coolant contamination by solid oxides. The permissible operating range depends on temperature and structural material. Consequently, an increase in oxide-layer thickness cannot, by itself, be interpreted as an increase in damaging corrosion; protective-layer formation and material degradation must be distinguished [83].

For compact-exchanger design, these observations support evaluating channel geometry together with wall temperature, material selection, and coolant chemistry. A useful durability assessment should report exposure duration, oxide-layer condition, and material loss alongside thermal–hydraulic performance. The results of a geometry-specific oxidation model should not be used alone to establish component lifetime or select a universally optimal coolant velocity. Here, corrosion is therefore treated as an application-specific constraint on feasible PCHE designs; comprehensive lifetime prediction remains outside the scope of this transport review.

Another fundamental design variable is working-fluid composition. The addition of He to CO$_2$ resulted in an increase in heat transfer of ~396% and an increase in ΔP of ~1147%, as recorded by Wen et al. [84] (see Figure 20b). In comparison, CO$_2$–Kr/Xe mixtures were found to deliver a superior thermo–hydraulic compromise among the mixtures tested. The result indicates that fluid property tuning has a significant influence on the performance of the compact exchanger; however, this might be associated with a high ΔP penalty. Consequently, heat transfer enhancement is not the only measure used for evaluating mixtures. It is important that they are also evaluated on the basis of ΔP, compressor or pumping work, stability, compatibility, and the benefits at the cycle level.

The operating constraints of coupled liquid-metal/sCO$_2$ PCHEs also explain how the preferred geometry changes with operating conditions. Under a ΔP limit of 55 kPa, Fu et al. [85] optimised LBE–sCO$_2$ intermediate heat-exchanger PCHEs, as illustrated in Figure 20c. They showed that heat transfer capacity can be considerably improved when the LBE side and the number of sCO$_2$ passages are increased. They also reported that the volumetric heat transfer rate could increase by roughly 176% when the rectangle-to-two configuration is chosen. This indicates that channel arrangement must be explicitly optimised for ΔP constraints. Without these constraints, a design could provide heat transfer but continue to be hydraulically impracticable.

Li et al. [86] established that heat transfer increases with increasing sCO$_2$ mass flow rate, pressure, and temperature difference. Conversely, heat transfer decreases with increasing heat-exchanger wall thickness and decreasing number of sCO$_2$ channels, while ΔP increases as the number of sCO$_2$ channels decreases, as illustrated in Figure 20d. This result highlights a common design trade-off in PCHEs. Reducing wall or passage dimensions increases the thermal conductance benefit; however, it could also increase the hydraulic penalty and mechanical stresses. Therefore, the optimum coupled-system design is not always the smallest design. Effectively, it is the design that meets the

following conditions, such as heat duty, ΔP limit, structural integrity, and material compatibility.

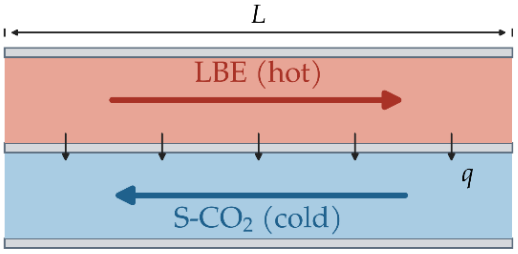
3.6.2. System-Level Integration, Duty-Specific Correlations, and Dynamic Operation

At the plant scale, the geometry of PCHs can impact not only local heat transfers but also cycle efficiency and economics. Gao et al. [6] related PCHE channel design to a small modular reactor (SMR)-based Brayton cycle and reported that a cycle efficiency of approximately 39.12% and a levelized cost of electricity (LCOE) of 0.0456/kWe can be achieved. This result demonstrates that channel geometry can influence plant performance, given that pressure loss, recuperator efficiency, and compactness affect cycle efficiency and cost. Accordingly, PCHE selection should not be entirely based on component-level thermal performance.

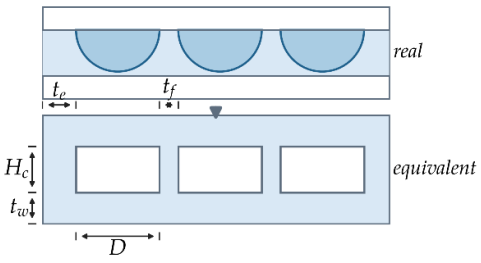
Additionally, duty-specific modelling is essential because precoolers, preheaters, and regenerators have different thermal boundary conditions and fluid-property variation regimes. Wang et al. [87] developed duty-specific correlations. The wall-driven precoolers achieved fits of approximately 99.5%, whereas the other configurations achieved fits of about 94.2%, with external validation errors of 8–14%. This finding is consistent with an important finding in this review, which states that a single generalised PCHE correlation is unlikely to be valid for all exchanger duties. Correlations should be correlated with exchanger function, temperature approach, wall condition, and local position in relation to the pseudo-critical region.

Another design constraint stems from the dynamic operating conditions. Cheng et al. [88] compared straight, sinusoidal-wavy, and zigzag channels under rolling motion. The change in h was observed to be about 0.02% for sinusoidal-wavy channels, 0.25% for straight channels, and 5.57% for zigzag channels at $T_0 = 2$ s and $\theta_m = 30°$. The change in ΔP between neighbouring periods was 163.63%, 446.59%, and 78.45%, respectively, for the three periods. The results reveal that the geometry with the best average heat transfer performance is not automatically the most appropriate for dynamic operation. The zigzag channels might provide higher average heat transfer, although they can also generate more significant oscillations, while the sinusoidal-wavy channels might be more stable.

The design of application-specific PCHs requires a more extensive assessment framework that assimilates steady local h and ΔP. In nuclear or liquid-metal systems, material compatibility and corrosion are limiting factors. In relation to mixture-based systems, there is a need to compensate for the additional ΔP that results from the increased heat transfer. In Brayton-cycle and SMR applications, channel design affects plant-level efficiency and economics. In moving or dynamically loaded systems, maximum average heat transfer may not be as important as thermal or hydraulic stability.



(**a**)



(**d**)

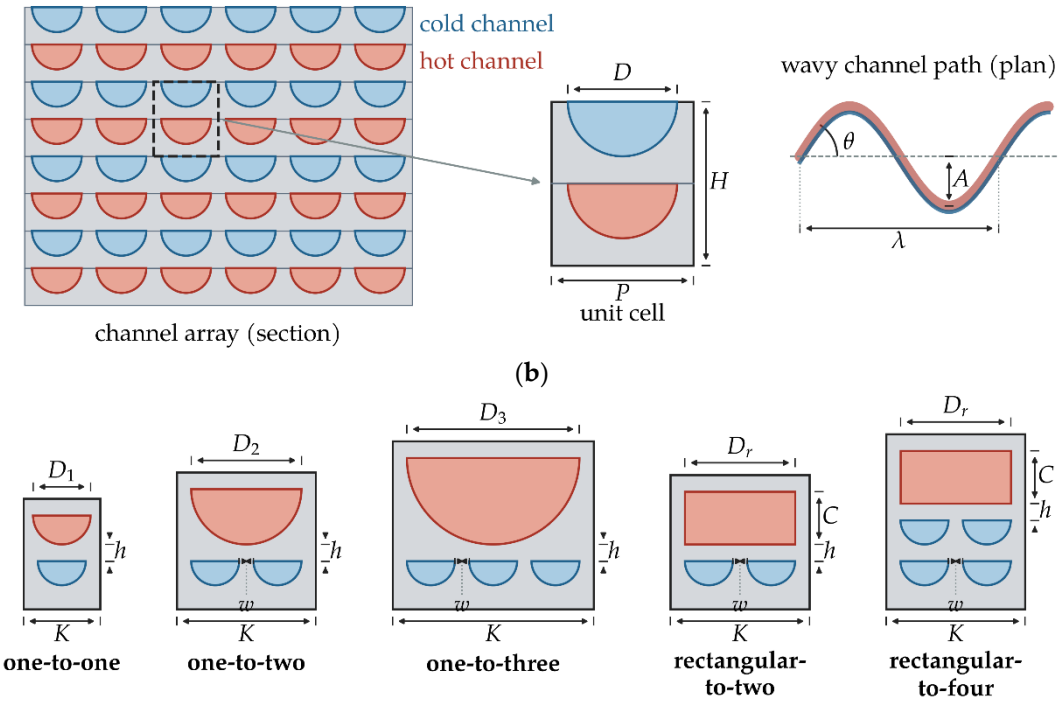


Figure 20. Proposed designs: (**a**) Liao et al. [82]; (**b**) Wen et al. [84]; (**c**) Fu et al. [85]; and (**d**) Li et al. [86].

Table 7. Important trends in application-specific, coupled-system and dynamic PCHE operation.

Topic	Main Studies	Application/Operating Context	Dominant Constraint	Main Quantitative Findings	Design Boundary and Implications
Materials and corrosion	Liao et al. [82]	LBE-cooled fast-reactor PCHEs with sCO_2 coolant	Oxidation corrosion, sharp-corner concentration, velocity-dependent durability	Numerical modelling identified sharp corners as corrosion-sensitive locations; oxide-growth predictions require interpretation within the model's material, chemistry, and operating conditions.	Geometry smoothing and velocity regulation are durability requirements, not only hydraulic design choices.
CO_2 mixtures	Wen et al. [84]	CO_2 mixed with He, Kr or Xe for compact heat transfer performance modification	Property tuning versus ΔP penalty	CO_2–He increased heat transfer by ~396% and ΔP by ~1147%; CO_2–Kr/Xe delivered the most effective thermo–hydraulic compromise.	Fluid composition can improve heat transfer; however, it may impose a severe ΔP penalty. Mixture selection must therefore include system-level pumping/compression impact.
Coupled LBE–sCO_2 PCHEs	Fu et al. [85], and Li et al. [86],	Intermediate heat exchangers and coupled liquid-metal/sCO_2 systems	ΔP limit, compactness, wall thickness, passage number, mechanical feasibility	Under a 55 kPa ΔP limit, a rectangle-to-two configuration reached approximately 176% of the natural heat transfer rate per unit volume; increasing sCO_2 mass flow rate, pressure, and temperature difference improved heat transfer; reducing wall thickness and sCO_2 channels increased compactness but increased ΔP.	Passage arrangement should be optimised under explicit ΔP and structural constraints. Maximum compactness is not always the most advantageous system design.
System-level integration	Gao et al. [6]	SMR-based Brayton cycle with PCHE integration	Coupling between PCHE geometry, cycle efficiency and economics	Optimised SMR Brayton-cycle PCHE achieved approximately 39.12% efficiency and LCOE of 0.0456/kWe.	Channel geometry affects plant-level economics through recuperator effectiveness, pressure loss, compactness and cycle performance.
Duty-specific correlations	Wang et al. [87]	Precoolers, preheaters and regenerators	Exchanger-duty dependence of predictive correlations	Correlation fits reached about 99.5% for wall-driven precoolers and 94.2% for other cases; external validation errors were typically 8–14%.	PCHE correlations should be matched to exchanger duty, wall condition, and operating region rather than applied universally.
Dynamic/rolling operation	Cheng et al. [88]	Straight, sinusoidal-wavy and zigzag channels under rolling motion	Thermal–hydraulic stability under dynamic operation	At $T_0 = 2$ s and $\theta_m = 30°$, h variation was −0.02% for sinusoidal-wavy, 0.25% for straight, and 5.57% for zigzag channels; ΔP variations were 163.63%, 446.59%, and 78.45%.	Sinusoidal-wavy channels support stability, whereas zigzag channels promote higher average heat transfer but larger oscillatory response.

4. Instabilities and Heat Transfer Deterioration in sCO_2: Pseudo-Boiling, Variable-Property Convection, and Feedback Mechanisms

Instabilities and HTD in sCO_2 compact thermal systems are caused by the combined influence of steep near-critical thermophysical-property gradients, buoyancy, thermal acceleration, partial relaminarisation, near-wall turbulence suppression, and flow redistribution. The effects are particularly noticeable near the pseudo-critical temperature, where relatively small changes in wall or bulk temperature cause significant changes in density, specific heat, viscosity, and thermal conductivity. Consequently, the local h, wall temperature distribution, ΔP, and flow stability can change considerably even when the fluid is maintained in a single-phase state.

The studies outlined in Figures 21–25 and Table 8 indicate that HTD is not regulated by a single mechanism. A pseudo-boiling framework is valuable to understand the pseudo-critical region, where the fluid displays different liquid-like, transition-like, and gas-like transport properties. However, pseudo-boiling should not be considered the only reason for HTD. Variable-property single-phase convection, buoyancy-induced stratification, thermal acceleration, turbulence suppression, inlet-state effects, channel-scale effects, and system-level feedback are all examples of effects that can be explained as causes of heat transfer deterioration, as documented in the literature. Thus, this section is intended to provide a physical analogy for pseudo-boiling rather than replace the variable-property convection theory.

A mechanism hierarchy would be helpful to connect the reviewed studies. First, sharp property variations in the vicinity of the pseudo-critical region cause local changes in density, specific heat, viscosity, and thermal conductivity. Second, these gradients influence buoyancy, acceleration, wall-normal mixing, and turbulence production. Third, local heat transfer is less effective and the near-wall region warms when the heated near-wall fluid develops sufficiently low density and thermal resistance. Fourth, for compact passage and coupled systems, this local deterioration can lead to variations in ΔP, mass flow oscillations, flow maldistribution, and dynamic instabilities. HTD and flow instability are distinct phenomena that may interact through thermo–hydraulic feedback under specific operating and system conditions.

4.1. Pseudo-Boiling, HTD Mechanisms, and Instability Onset

Interpretation of Figure 21 requires distinguishing subcritical boiling from single-phase transport at supercritical pressure. Liu et al. [89] simulated near-critical film boiling at 7.0 and 7.37 MPa, where liquid and vapour coexist with a phase interface, as shown in Figure 21a. Their 7.5 MPa case instead represents variable-property, single-phase natural convection without a liquid–vapour interface. Its initial bulk temperature was 10 °C, below the critical temperature; heating produces a continuous transition through the pseudo-critical region. Accordingly, “liquid-like” and “gas-like” describe property states rather than coexisting phases.

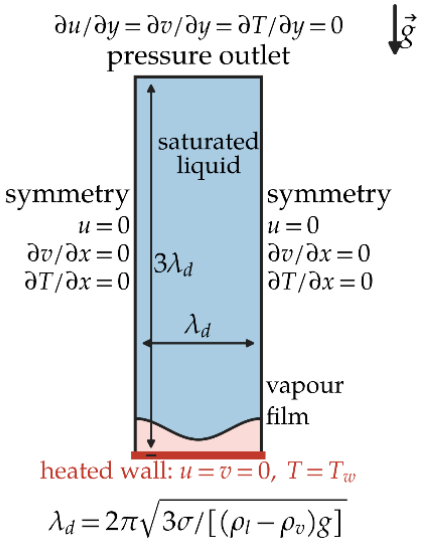
These pool-heating results provide qualitative insight into low-density near-wall layers and buoyant plumes. Their application to confined forced convection requires separate consideration of imposed mass flux, confinement, wall shear, and thermal acceleration. They therefore do not establish channel HTD thresholds or demonstrate identical deterioration mechanisms across these configurations.

As pressure increased, Whitaker et al. [90] found that the flow behaviour changed progressively from near-critical boiling-like behaviour to supercritical-like behaviour, as illustrated in Figure 21b. Wang et al. [91] formally described this behaviour using a three-regime pseudo-boiling framework bounded by T− and T+, as explained in Figure 21c.

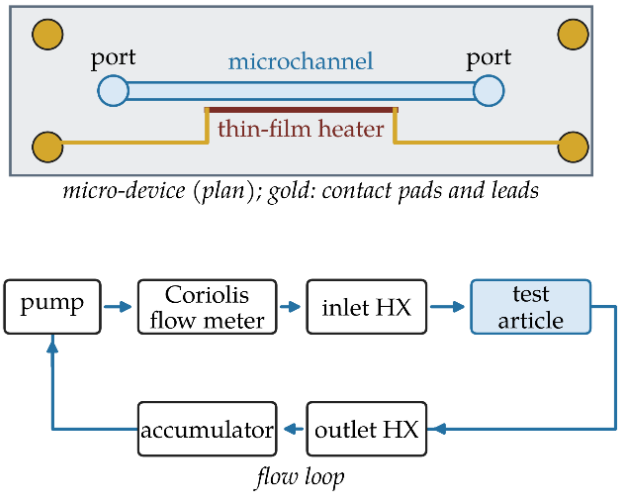
These studies confirm that the heat transfer near the pseudo-critical region cannot be accurately described by the standard single-phase correlations based on the bulk properties. Significantly, local wall states relative to the pseudo-critical line must be considered.

There are also system-scale and criterion-based studies that support this viewpoint; however, they also demonstrate the limitations associated with an entirely pseudo-boiling-based explanation. Chen et al. [92] found that thermosyphon performance is highest when operating near the pseudo-critical temperature and that cool-side performance is less affected when the flow rate is determined, as depicted in Figure 21d. This indicates that instability and HTD may encompass local wall-layer behaviour, in addition to circulation feedback. Longmire and Banuti [93] reported that under HTD-prone conditions, a gas-like low-conductivity wall layer may form, with behaviour similar to film boiling. To differentiate between normal and HTD, Xu et al. [94] suggested a critical threshold for supercritical boiling.

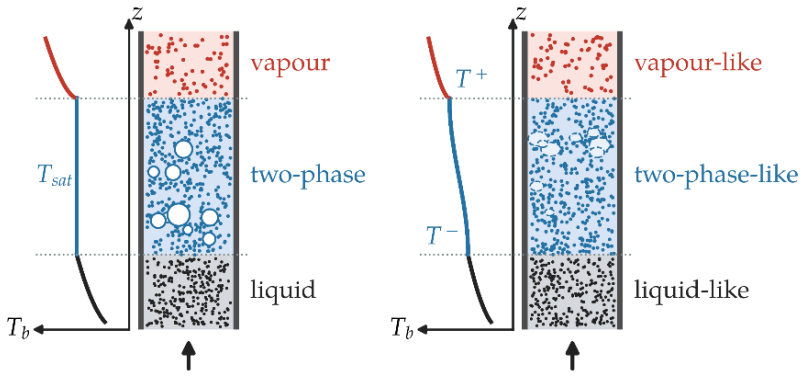
The results in Figure 21 imply that the onset of HTD is not necessarily connected with the failure of turbulent heat transfer, but rather with a transition in the transport regime. However, the change is not entirely controlled by pseudo-boiling. For a complete understanding, pseudo-critical property variations, variable-property convection, buoyancy, thermal acceleration, near-wall turbulence modification, and the system feedback must be considered simultaneously.



(**a**)



(**b**)



(**c**)

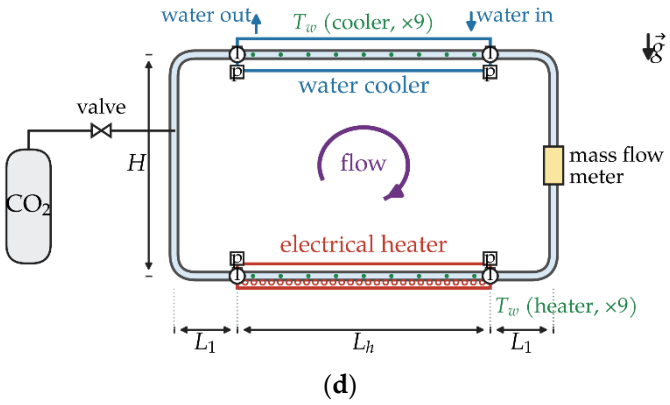


Figure 21. HTD investigation: (**a**) Liu et al. [89]; (**b**) Whitaker et al. [90]; (**c**) Wang et al. [91]; and (**d**) Chen et al. [92].

4.2. Geometry, System Operation and HTD Mitigation

HTD is significantly influenced by geometry and hydraulic scale owing to the effects on secondary flow, stratification, wall-layer renewal, and the residence time of near-wall fluid in the pseudo-critical region. Channel geometry can either exacerbate or alleviate HTD, depending on whether it promotes mixing without creating unnecessary friction or flow instability, as shown by the studies in Figure 22.

For 7-pin bundles, Liu et al. [95] found that wire-wrap spacers in a bundle promote crossflow mixing and maintain lower edge channel temperatures. A PEC > 1 was reached at q″ above 1 kW/cm^2, as presented in Figure 22a. This implies that if the mixing exceeds the hydraulic penalty, it can help to reduce the deterioration of the local wall layer caused by spacer-induced mixing. In the two-phase-like regime, Cheng et al. [96] demonstrated that the top-generatrix degradation is influenced by the tube diameter. However, the influence of the diameter is reduced when the bulk temperature is above the degradation band, as shown in Figure 22b. The finding confirms the importance of hydraulic scale, although its effect is dependent on the local thermodynamic regime.

Fan and Tang [97] demonstrated that non-uniform circumferential heating increases the local viscous-sublayer thickness and decreases diffusion, as shown in Figure 22c. Under buoyancy, Wang et al. [98] provided evidence that large horizontal tubes have a greater temperature difference between the top and bottom, as illustrated in Figure 22d. The results presented here indicate that the redistribution of low-density near-wall fluid is governed not only by buoyancy, but also influenced by the location at which q″ is applied. Therefore, non-uniform heating can alter a globally acceptable heat transfer condition into a local wall temperature problem.

Li et al. [99] demonstrated that conical strips can completely suppress the HTD in large vertical tubes, with COP values ranging from 1.21–1.35, as shown in Figure 22e. This indicates that near-wall reattachment is possible and can be prevented by using well-designed inserts. Conversely, Cheng and Xu [15] found that non-uniform axial heating in large vertical tubes improves mixing and increases friction, although vapour-like layers remain near the wall, as depicted in Figure 22f. This contrast is significant given that additional mixing is not always sufficient to remove HTD. The mixing must take place in the appropriate region and should be sufficiently intense to break the low-density wall layer without causing a significant ΔP.

Geometry influences HTD by its influence on wall layer recovery, secondary flow, buoyancy-driven redistribution and sensitivity to thermal-boundary conditions, as summarised in Figure 22. Accordingly, the potential for HTD mitigation should be based on thermal and hydraulic considerations, such as wall temperature peak, circumferential non-uniformity, friction penalty, and stability margin.

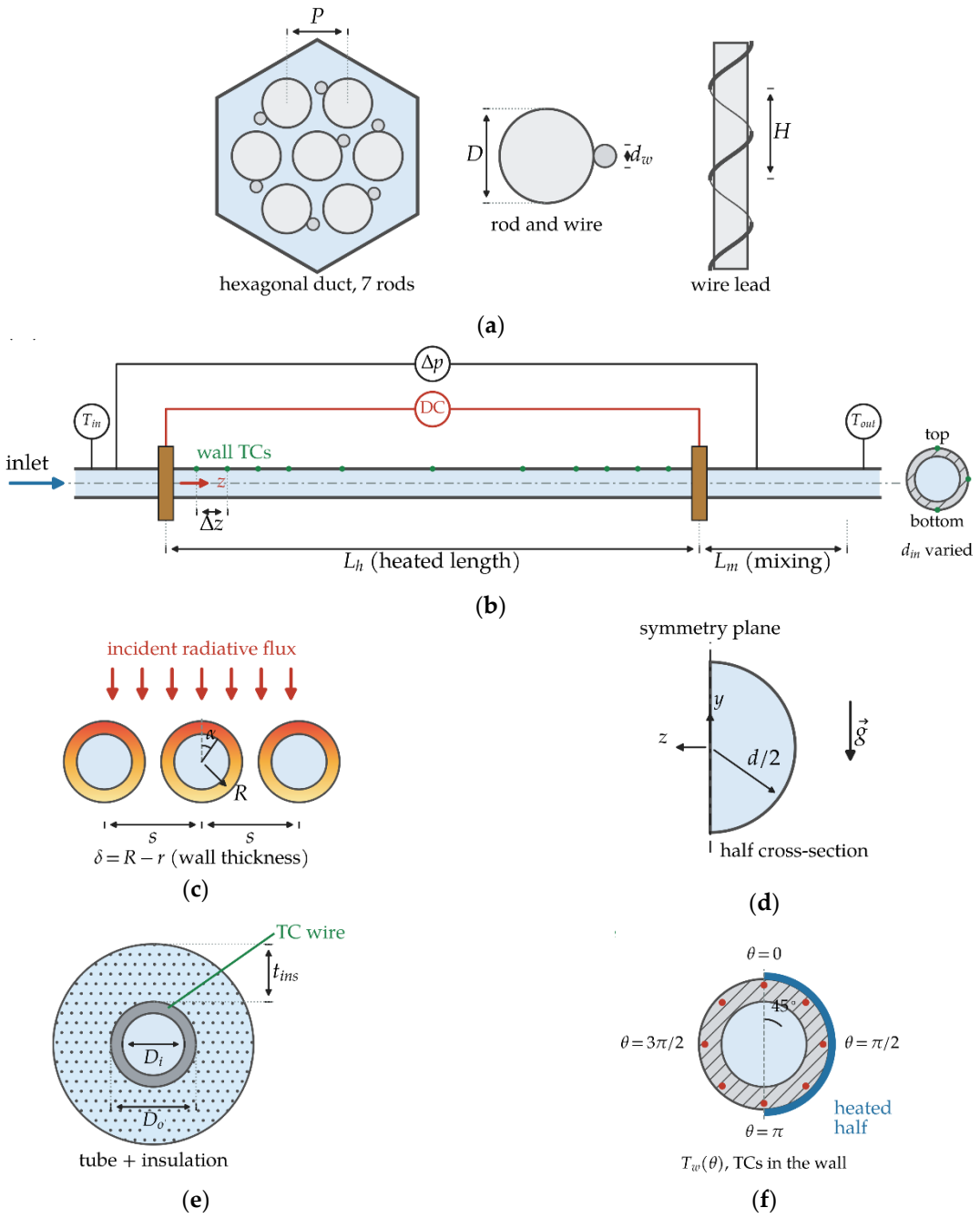


Figure 22. Geometric features: (**a**) Liu et al. [95]; (**b**) Cheng et al. [96]; (**c**) Fan and Tang [97]; (**d**) Wang et al. [98]; (**e**) Li et al. [99]; and (**f**) Cheng and Xu [15].

As shown by the instability studies in Figure 23, HTD reveals a clear tendency to be associated with oscillatory behaviour. Zhang et al. [100] reported wall temperature oscillations and mass-flow excursions when q″ exceeded the deterioration threshold, as shown in Figure 23a. Luo et al. [101] recorded regular oscillations near the pseudo-critical state in natural-circulation parallel channels with a period of approximately 28 s, an amplitude of 14–21%, and a wall temperature variation of almost 12%, as depicted in Figure 23b. According to these studies, the occurrence or intensification of hydraulic oscillations can be observed as a result of variations in local properties affecting density and flow distribution, which in turn results in a ΔP.

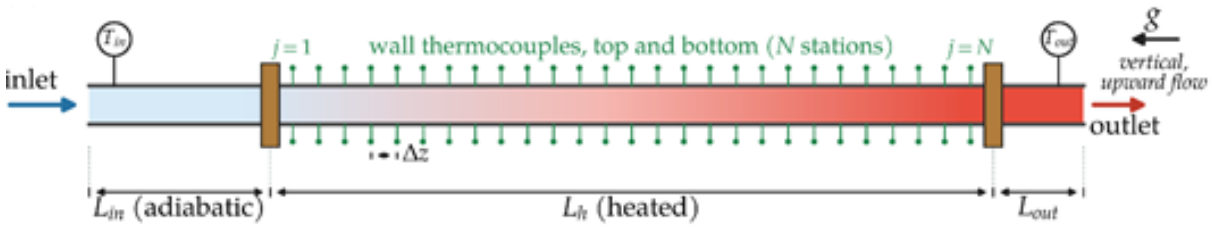
In the study they conducted, Wang et al. [102] demonstrated that the critical trans-pseudocritical number can be lowered by roughly 20.6% using converging–diverging tubes as compared with straight tubes, consequently supporting density-wave oscillations,

as shown in Figure 23c. This is significant because it demonstrates that a geometry designed to increase heat transfer can reduce the stability threshold.

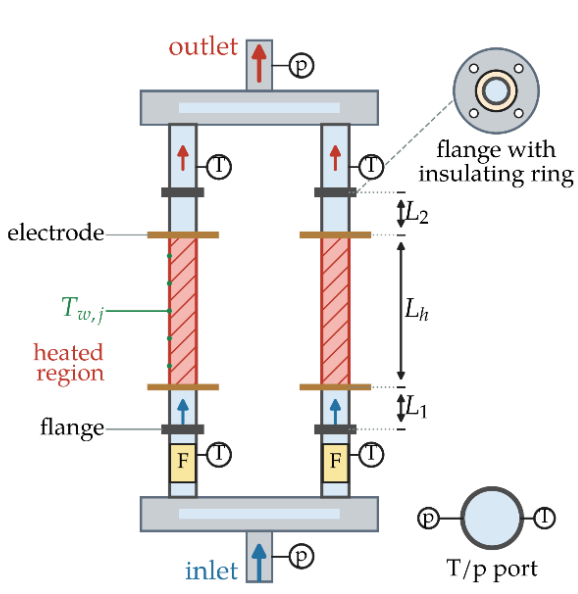
As discussed by Cai et al. [103], an instability can emerge after the onset of HTD and re-emerge after partial recovery, as illustrated in Figure 23d. Zhang et al. [104] associated the instability with thermal-acceleration-induced relaminarisation.

The studies in Figure 23 demonstrate interactions between HTD and oscillations under particular conditions, rather than equivalence between these phenomena. Local HTD concerns impaired wall heat removal, identified through reduced h or increased wall temperature relative to a specified reference. Steady flow redistribution concerns unequal channel flow rates without necessarily involving temporal oscillations. Dynamic instability requires time-dependent evidence, such as sustained or growing fluctuations in mass flow, pressure, or temperature beyond measurement uncertainty or numerical noise.

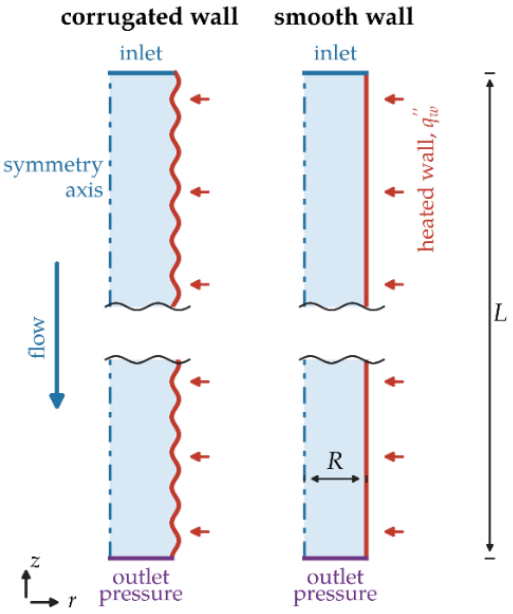
For example, Zhang et al. [100] experimentally observed oscillations in a uniformly heated vertical tube at G = 240–400 kg/m² s and p = 7.5–9 MPa. Wang et al. [102] used dynamic simulations to demonstrate increased susceptibility to density-wave oscillations in converging–diverging tubes. These findings support case-specific coupling, but their onset criteria should not be transferred directly to natural-circulation loops, parallel channels, or PCHEs with different boundary conditions.



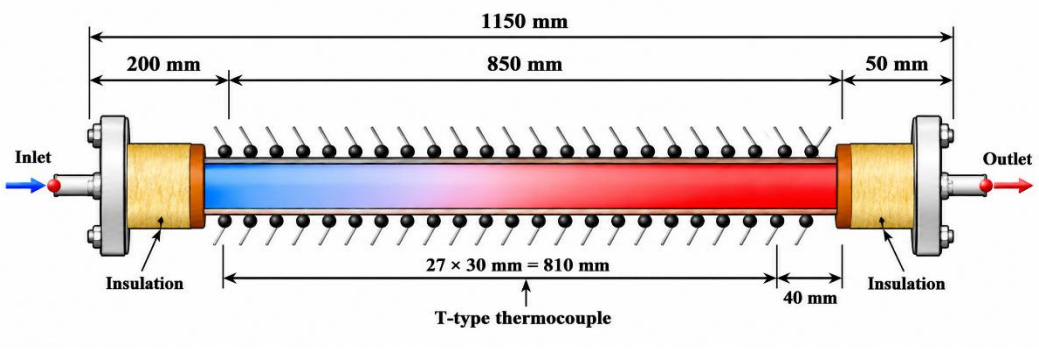
(**a**)



(**b**)



(**c**)



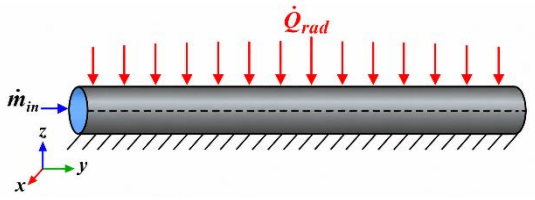
(**d**)

Figure 23. Instability analysis: (**a**) Zhang et al. [100]; (**b**) Luo et al. [101]; (**c**) Wang et al. [102]; and (**d**) Cai et al. [103].

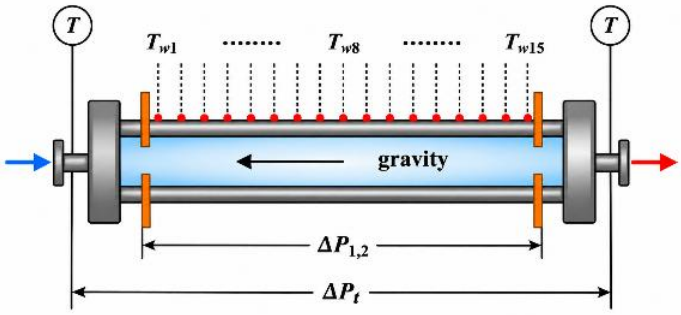
This explanation extends beyond individual channels to system-level and mitigation studies, as illustrated in Figure 24. Studies by Emerick et al. [105] demonstrated that the performance of a solar receiver can be improved by approximately 3% via the non-uniform distribution of sCO_2 flow within the receiver, as shown in Figure 24a. While flow maldistribution is generally viewed as detrimental, this result shows that deliberately designed flow maldistribution can lead to a better match between heat input and coolant flow at the receivers. Huang et al. [106] established that ΔP oscillations are inhibited by increasing the pressuriser size, as shown in Figure 24b. Draskic et al. [107] reported that oscillations around the pseudo-critical region are more severe at lower driving heights, but can be decreased either by increasing the mass flow rate or by increasing the cold-leg resistance.

Zhang et al. [108] reported that bottom heating provides the most uniform heat transfer in a sealed natural-convection system, as illustrated in Figure 24c. This is an indication that heating location is an important factor regulating stability-related variables. Chen et al. [109] and Wang et al. [110] proved that lattice arrays can reduce peak wall temperature by more than 40 °C and increase the h by up to 11.5 times. According to these studies, it is essential to implement both local enhancement and system-level stabilisation because local enhancement is effective in reducing peaks in wall temperature, whereas hydraulic stabilisation can suppress oscillatory feedback.

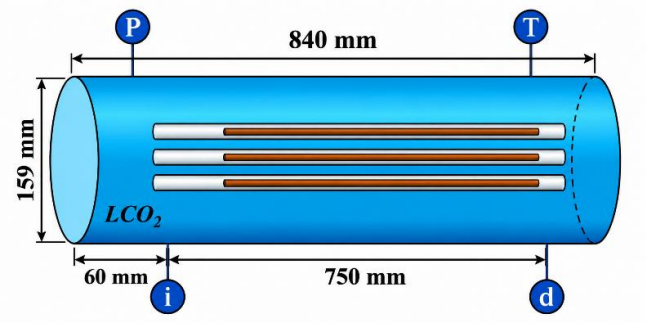
Figure 24 indicates that local and system-level measures are required for HTD mitigation. The near-wall layer can be renewed using inserts, lattices, and enhanced surfaces, whereas the hydraulic loop can be stabilised using pressurisers, cold-leg resistance, mass-flow control, and flow-distribution strategies.



(**a**)



(**b**)



(**c**)

Figure 24. System-level operation: (**a**) Emerick et al. [105]; (**b**) Huang et al. [106]; and (**c**) Zhang et al. [108].

4.3. Near-Critical Transport in Components and Specialised Systems

The studies in Figure 25 provide supporting context for the component-level consequences of near-critical transport. They are considered where they clarify thermal-boundary conditions, circulation feedback, or prediction limitations relevant to compact passages. Their application-specific findings do not establish general performance rankings or imply that the same mechanisms govern every system.

Yan et al. [111] demonstrated that after optimisation, a net power output of up to ~162 kW can be obtained while reducing fuel consumption in a closed-Brayton thermal-management system, as illustrated in Figure 25a. Dang et al. [112] established that partial wall coating has the ability to alter thermal response, revealing that wall treatment can influence component-level heat management, as shown in Figure 25b. With periodic flow reversal and a resulting amplification of convection, Zhang et al. [113] reported that natural circulation can achieve $Re = 6 \times 10^4$, as described in Figure 25c. For a cylindrical-fin compact receiver with horizontal flow and sidewall heating, Zhang et al. [114] reported buoyancy and acceleration significance thresholds of $Ri = 5.7 \times 10^{-3}$ and $Ac = 5.8 \times 10^{-7}$, respectively, as shown in Figure 25d. The results presented by Wang et al. [115] indicate that viscous dissipation accounts for less entropy generation than heat transfer, as illustrated in Figure 25e. This research explains that near-critical transport influences not just the h but also entropy generation, receiver safety, circulation stability, and system efficiency.

Evidence obtained from more specialised systems is in agreement. Wang and Hu [116] reported that a thermoacoustic engine based on a PCHE can attain a mean pressure of 9.621 MPa with an onset temperature difference of only 14.8 °C in the critical region, as shown in Figure 25f. In the transcritical range, homogeneous equilibrium modelling can overestimate the liquid fraction by around 12%, as shown by Huang et al. [117], at a critical pressure ratio of 0.54–0.55, as depicted in Figure 25g. Xi et al. [118] showed that sCO_2 jets can have longer potential cores than subcritical jets, with sharper and more diffusion-dominated interfaces, as illustrated in Figure 25h. Additionally, Xiong et al. [119] reported changes of approximately 83% in load and heat dissipation within lubrication films near the pseudo-critical point. The results show that pseudo-critical transport influences not only heat-exchanger performance, but also expansion, mixing, acoustics, and lubrication.

The complexity means that empirical correlations should be applied with caution. Classical correlations suggested by Winterton [120], Gnielinski [121], and Jackson [122] continue to be effective, but their accuracy can be reduced by pseudo-critical property gradients, non-uniform heating, compact passages, buoyancy, acceleration, and geometry-induced mixing. A more recent set of geometry-specific and near-critical correlations [123,124] is also available to use as a basis for compact sCO_2 design; however, it is also limited by its calibration range. Therefore, the physical interpretation and

applicability limits should be emphasised in the main text, while the detailed mathematical forms and validity limits of the correlations are provided in Appendix A.

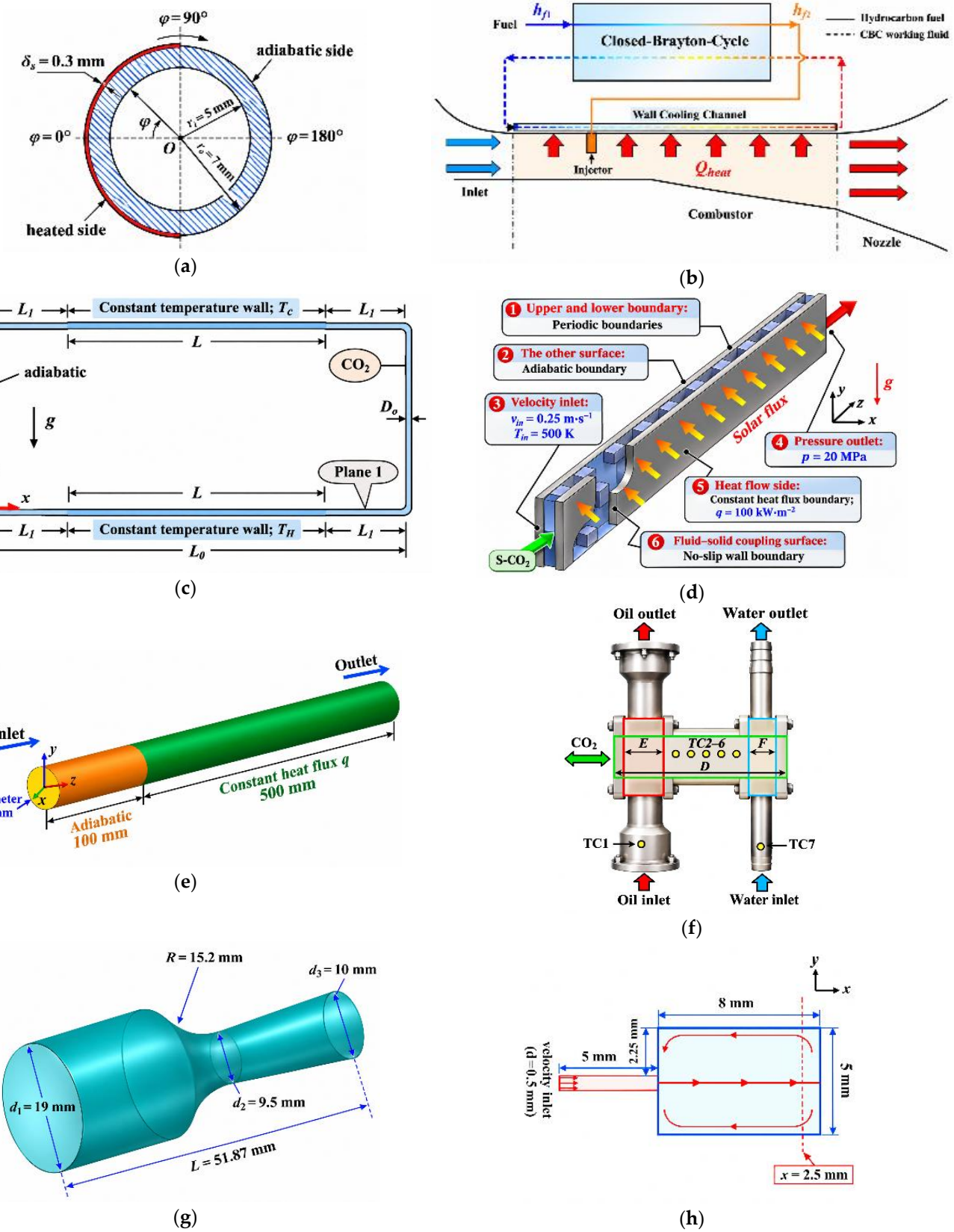


Figure 25. Precooling designs: (**a**) Yan et al. [111]; (**b**) Dang et al. [112]; (**c**) Zhang et al. [113]; (**d**) Zhang et al. [114]; (**e**) Wang et al. [115]; (**f**) Wang and Hu [116]; (**g**) Huang et al. [117]; and (**h**) Xi et al. [118].

Table 8. Significant trends in HTD, instability, and system-level sCO_2 operation.

Topic	Main Studies	Dominant Mechanism	Main Quantitative Findings	Limitations/Cautions	Design Implications
Pseudo-boiling and HTD onset	Liu et al. [89], Whitaker et al. [90], Wang et al. [91], Chen et al. [92], Longmire and Banuti [93], and Xu et al. [94]	Pseudo-critical property transition, liquid-gas transport, gas near-wall layer	Subcritical film boiling at 7.0/7.37 MPa; single-phase natural convection at 7.5 MPa; three transport bands proposed; critical supercritical-boiling number introduced	Pseudo-boiling is an analogy, rather than two-phase flow. It cannot by itself explain all HTD cases	Use pseudo-boiling to identify high-risk wall-layer transition regions combined with variable-property convection, buoyancy and acceleration analysis
Geometry and scale effects	Liu et al. [95], Cheng et al. [96], Fan and Tang [97], Wang et al. [98], Li et al. [99], and Cheng and Xu [15].	Secondary flow, wall-layer renewal, circumferential stratification, and diameter and heating-location effects	Wire-wrap spacers achieved PEC > 1; conical strips suppressed HTD with COP = 1.21–1.35; large diameters intensified top–bottom separation	Additional mixing may increase friction without removing gas-like wall layers under heating conditions	Geometry should be selected to promote near-wall layer renewal and suppress local wall-film formation without experiencing excessive hydraulic penalty
Oscillations and instability	Zhang et al. [100], Luo et al. [101], Cai et al. [103], Zhang et al. [104], and Wang et al. [102].	Density-wave oscillations, thermal-acceleration-induced relaminarisation, mass-flow feedback	Mass-flow excursions exceeded ±10%; oscillation periods ≈ 28 s; amplitudes 14–21%; converging–diverging tubes reduced critical trans-pseudocritical number by ≈20.6%	Enhancement geometries can reduce stability margins even when they improve average heat transfer	Assess HTD and instability together using coupled heat transfer/ΔP/stability criteria
System-level stabilisation and mitigation	Emerick et al. [105], Huang et al. [106], Draskic et al. [107], Zhang et al. [108], Chen et al. [109] and Wang et al. [110]	Flow redistribution, pressuriser damping, cold-leg resistance, heating-location control, lattice-enhanced mixing	Receiver performance improved by ≈3%; ten-panel layout reached ≈76%; lattice arrays reduced wall temperature peaks by >40 °C and increased h up to 11.5×; other mitigation strategies reduced peak wall temperature by ≈50 °C and increased h by ≈140%	Receiver-scale flow redistribution and local enhancement may not be directly applicable to closed-loop or PCHE operation without stability assessment	Combine local HTD mitigation with hydraulic-loop stabilisation and flow-distribution control
Component and cycle implications	Yan et al. [111], Dang et al. [112], Zhang et al.	Coupling between near-critical transport, entropy generation,	Closed-Brayton net power ≈162 kW; natural circulation	Component-level results are application-specific	HTD behaviour should be included in component and plant-scale design,

	[113], Zhang et al. [114], and Wang et al. [115]	coating/wall treatment, natural circulation and receiver thresholds	reached Re ≈ 6×10^4; deterioration thresholds of Ri = 5.7×10^{-3} and Ac = 5.8×10^{-7}; entropy generation dominated by heat transfer rather than viscous dissipation	and should not be generalised without matching operating conditions	specifically for receivers, thermal-management loops and Brayton systems
Interfacial and specialised transport	Wang and Hu [116], Huang et al. [117], Xi et al. [118], and Xiong et al. [119]	Thermoacoustic response, transcritical expansion, jet mixing, lubrication-film property variation	Mean pressure reached 9.621 MPa at an onset temperature difference of 14.8 °C; homogeneous equilibrium modelling overestimated liquid fraction by ≈12%; load and heat-dissipation variations reached ≈83% near Tpc	Standard heat-exchanger correlations do not represent these effects	Near-critical property variation should be considered in expansion, mixing, acoustic and lubrication applications
Correlation use	Winterton [120], Gnielinski [121], Jackson [122–124]	Empirical prediction under strong property variation, non-uniform heating, compact geometry, buoyancy and acceleration	Classical models remain useful reference tools; geometry-specific correlations are generally more reliable for compact near-critical conditions	Correlations are bounded by calibration range and may fail under non-uniform heating or enhanced geometries	Detailed equations retained in Appendix A; validity range, error band, geometry type and operating window provided for each correlation

5. Comparative Synthesis, Correlation Coverage and Further Research

This section synthesises the evidence around the review's two central questions. First, it examines how geometry and heating conditions modify buoyancy, acceleration, mixing, and near-wall transport. Second, it assesses whether reported performance gains and predictive models remain applicable beyond their original configurations. The resulting design guidance identifies the limiting mechanism, the demonstrated benefit of a modification, and the conditions bounding its use.

The reviewed studies encompass various D_h, operating pressures, G and q″, heating modes, channel lengths, and ΔP definitions. The goodness factor or entropy-generation metric can differ considerably for each case. Consequently, this review compares the geometries employing reported and directly comparable metrics, such as heat transfer enhancement, $\Delta P/f$ penalty, PEC, pumping-power requirements, compactness, thermal uniformity, HTD tendency, stability, and correlation reliability. Formal PEC, goodness-factor, and entropy-generation values are discussed only when they are reported in the original studies or can be directly calculated from the available data.

The synthesis is arranged around Figures 26–31. Figure 26 brings together compact passage geometries, applications, and their dominant mechanisms, whereas Figure 27 compares the trade-offs between different fluid platforms.

Figure 28 summarises the scale–surface architecture matrix, Figure 29 compares fin and insert families, and Figure 30 links HTD mechanisms with stability and mitigation strategies. Figure 31 summarises the main literature gaps, correlation coverage in Appendix A, and the future-work roadmap. The findings are converted into explicit design and research implications in Tables 9–13. Configuration selection should satisfy the required heat duty and wall temperature limits within acceptable pressure-drop, manufacturing, and operating constraints, using predictive models validated for the intended conditions.

5.1. Compact sCO_2 Passage Geometry and Applications

The first level of synthesis, which is set out in Figure 26, connects compact passage families with the application domain and dominant physical mechanisms. This is required since the examined configurations cannot be ranked without considering the configuration's function. A geometry that performs well in a baseline test section may be an appropriate choice for a PCHE recuperator, while a highly enhanced lattice or twisted-tape passage might provide better HTD control, but be unsuitable under pumping-power constraints.

Valuable reference geometries consist of straight and smooth tubes with the benefit that they provide a good indication of the fundamental mechanisms of near-pseudocritical heat transfer, such as stratification, thermal acceleration, partial relaminarisation, upper-wall temperature rise, and the onset of HTD. In most cases, however, they are not the most suitable for system applications requiring small size and high heat duty, owing to the limited ability to suppress local wall overheating under high q″ and low G.

Curved, serpentine, tapered, diverging, and flattened passages fall within the middle range of designs. They are able to alter the near-wall flow through secondary flows, local acceleration, and changes in flow area. In some cases, these geometries enhance heat transfer and minimise ΔP. However, the advantage is extremely dependent on heating conditions, flow conditions, and local thermodynamic state near the pseudo-critical temperature. Accordingly, profiled or curved passages should not be regarded as superior to straight passages.

The most suitable compact-system candidates are micro/minichannel heat sinks and PCHE passages. Micro/minichannels have short thermal diffusion lengths and high surface-area density, but are sensitive to property gradients across the wall-normal direction, unidirectional heating, $D_{h,}$ and local crossing of Tpc. PCHEs are compact, deliver high pressure resistance, and are compatible with thermal integration, particularly in Brayton cycle recuperators, precoolers, nuclear applications, and compact energy devices. Nonetheless, their performance is influenced not only by the passage geometry, but also by the header design, channel routing, maldistribution of the flows, topology, manufacturability, and off-design operation. The enhanced passages provide a way to control HTD and reduce hot spots, including ribs, grooves, pin fins, twisted tapes, lattice inserts, and AM roughness. These can be effective near-wall flow restratifiers and reduce thermal stratification, but generally they increase friction or manufacturing complexity. They can be acceptable when local wall temperature control or the mitigation of local hot spots in the heated region is considered more important than minimum pumping power.

Table 9 shows a summary of the dominant mechanisms, primary thermal benefit, hydraulic penalties, appropriate application range, and design implications of the various compact sCO_2 passage families shown in Figure 26, providing a qualitative design synthesis of their approaches.

Table 9 underlines the importance of not ranking the reviewed geometries based only on heat transfer enhancement. Instead, each configuration has a distinctive role to play in the design, including baseline mechanism identification, compact high-flux cooling, PCHE integration, hot-spot suppression, HTD mitigation, hydraulic economy, and system stability. The level of detail relating to operating conditions varies among the reviewed studies. Therefore, the tables provide data on channel scale, operating pressure, G, q″, heat transfer enhancement, ΔP/friction penalty, and applicability boundaries only when these constraints were provided in the original studies. Where this information is not usually reported, it is not recalculated or inferred. In these cases, it is treated as a qualitative design implication. This ensures that no unsupported comparisons are made whilst allowing the tables to provide a practical summary of the design when comparing compact sCO_2 configurations.

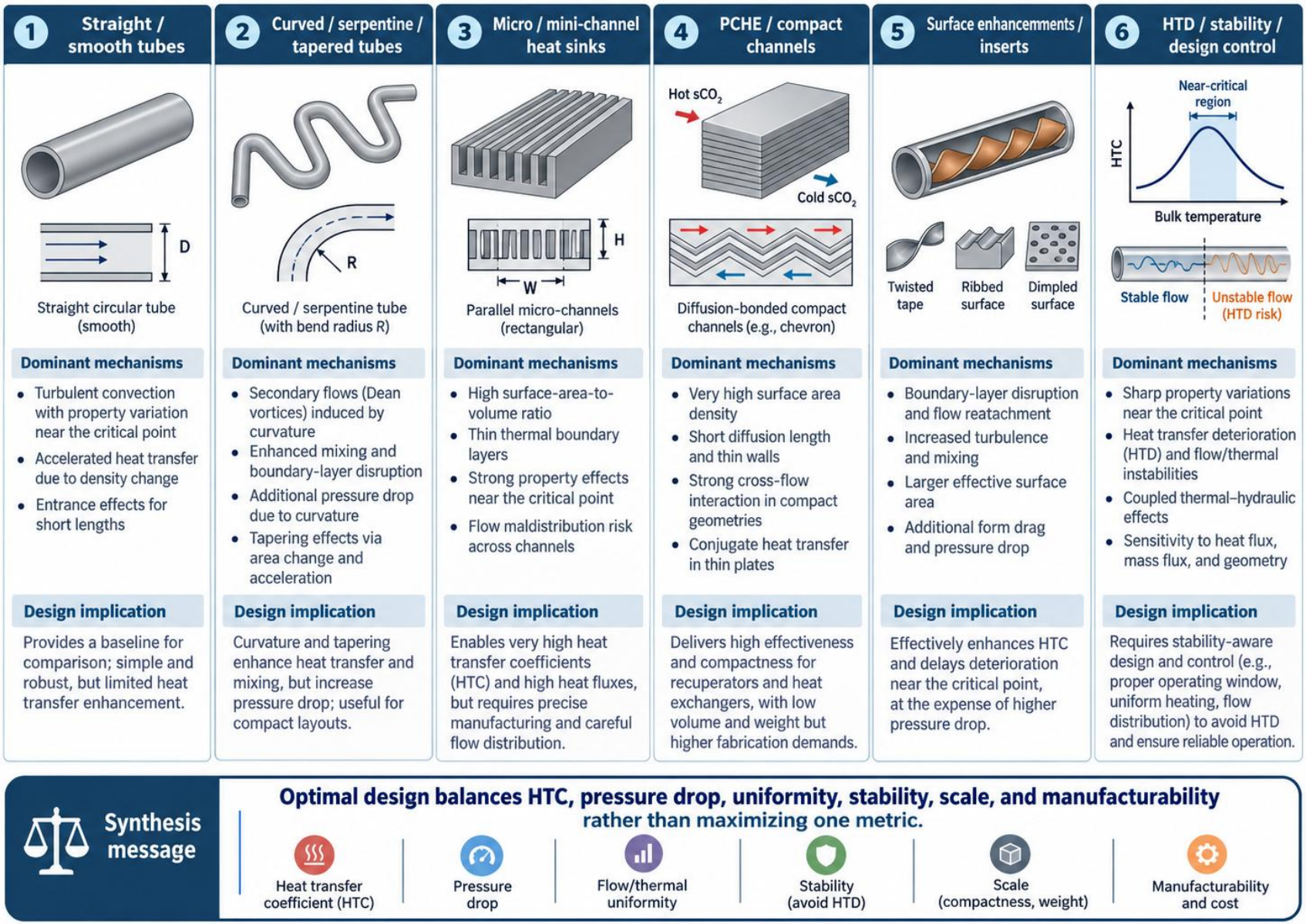


Figure 26. Compact sCO_2 passage geometries and applications [17,23,30,69,79,100].

https://doi.org/10.3390/en19215380

Table 9. Design-level interpretation of compact sCO_2 passage families.

Passage Family	Dominant Mechanism	Representative Thermal Benefit	Representative Hydraulic Penalty	Potential Application	Design Implications
Straight/smooth tubes	Buoyancy, thermal acceleration, pseudo-critical property variation	Baseline reference	HTD and circumferential non-uniformity achievable	Mechanism studies; correlation benchmarking	Use as reference geometry, instead of as an optimised compact design
Curved/serpentine passages	Secondary flow and cross-sectional mixing	Local h up to 1.285×	f +9%; possible large axial/cross-sectional ΔT	Compact passages where secondary flow is beneficial	Use only when secondary flow improves wall-layer renewal without excessive ΔP
Diverging/profiled tubes	Area variation and local acceleration control	Heat transfer +5.2–28.6%; flattened tubes up to ~64–65%	Diverging tubes: ΔP −52.1 to −68.5%; flattened tubes may increase ΔP	Low-ΔP or high-h tube enhancement	Select diverging tubes for hydraulic economy and flattened/profiled tubes for higher h
Micro/mini-channel heat sinks	Short thermal length, local Tpc crossing, wall-normal gradients	h up to 2.37×; base temperature −27.2%	Highly geometry- and heating-dependent	Electronics cooling; high q″ compact devices	Evaluate h, ΔP, base temperature and uniformity simultaneously
PCHE passages	Compactness, topology-controlled mixing, pressure-resistant construction	Zigzag channels: h ≈ 2× the Dittus–Boelter prediction; U +18.8% relative to the original straight-channel model at 8.85 MPa; CO_2/water inlet temperatures 313.72/298.15 K and mass flow rates 0.023/0.020 kg/s.	Zigzag channels: f ≈ 7–10× that of straight channels; maldistribution requires separate assessment.	Recuperators, precoolers, Brayton-cycle and nuclear heat exchangers	Co-design channel geometry, headers, manifolds and operating point
Ribs/grooves/concaves	Near-wall flow reorganisation	h +25.61%; evaluation factor up to ~2.03	Friction +11.81% in reported cases	Moderate passive enhancement	Assess enhancement and hydraulic penalty together under the reported operating conditions.
Pin fins/mini-ribs	Wake mixing, surface-area increase, hot-spot disruption	h up to 3.08× that of plain channels; reported peak surface-temperature reduction of approximately 36–37%.	Form drag and blockage increase	High q″ cooling; hot-spot control	Use when peak wall temperature is the main constraint
Twisted tapes	Swirl and circumferential mixing	Nu ratio ~3.43–5.75; thermal non-uniformity reduction up to 95.7%	f ratio ~3.63–7.29	Stratification control and HTD mitigation	Useful for stratification suppression and wall temperature control when additional pumping requirements are acceptable
Lattice/AM structures	Three-dimensional mixing and distributed roughness	Lattices: Nu up to ~3.78–11.49×; AM roughness: Nu +126–234%	AM roughness: f +120–297%; lattices may cause high ΔP	Severe HTD mitigation; AM-enabled compact passages	Optimise density, roughness and hydraulic penalty together

Table 9 summarises source-specific findings. Its reported enhancement factors and hydraulic penalties should be compared quantitatively only where the reference configurations, operating conditions and metric definitions are compatible.

https://doi.org/10.3390/en19215380

5.2. Fluid-Platform and Thermophysical Trade-Offs

The progression from geometry selection to fluid-platform selection is illustrated in Figure 27. This is significant because the thermophysical response of the working fluid in the pseudo-critical region also affects sCO_2 performance, as opposed to the performance only being determined by the channel architecture. Pure sCO_2 has a high specific-heat peak, large density variations, and high heat transfer potential near Tpc. These same attributes also make the flow sensitive to buoyancy, thermal acceleration, as well as pressure distribution and heating distribution.

A significant advantage of pure sCO_2 is its ability to deliver significant heat transfer enhancement in a compact volume when operating near the pseudo-critical region. These characteristics make sCO_2 attractive for compact Brayton-cycle heat exchangers, high-flux cooling, solar receivers, and advanced thermal management systems. The disadvantage is that the same steep property gradients can cause HTD, wall temperature rise, oscillatory instability, and correlation failure when the local wall or bulk state passes through the pseudo-critical zone too rapidly or non-uniformly.

Modifying or blending CO_2 can affect the pseudo-critical temperature and the thermal compatibility of the fluid with the application. This can be useful when the desired heat-source or sink temperature is not well matched to pure CO_2. However, mixtures present trade-offs, such as higher ΔP, different compression work requirements, uncertainty in property predictions, material incompatibility, and the need for extra validation. Consequently, mixture selection should consider not only heat transfer enhancement, but system-level metrics, such as heat duty, ΔP, pumping or compression power, thermal stability, and component compatibility.

Although alternative fluid benchmarks, such as water, helium, hydrocarbons, liquid metals, as well as other supercritical fluids, are valuable for comparison, they help to identify whether the advantages associated with sCO_2 are attributable to its thermophysical properties, compactness, or system-level characteristics. For example, when considering specific near-pseudocritical heat-sink conditions, water may exhibit simplified thermal behaviour, whereas sCO_2 could provide reduced ΔP and increased compactness. As a result, the choice of working fluid can be undertaken in conjunction with the geometry and operating window, as opposed to being considered afterwards. Figure 27 illustrates how the selection of the working fluid influences the allowable operating window.

5.3. Scale–Surface Architecture Matrix

Figure 28 provides an architectural synthesis of the review by separating compact sCO_2 systems according to hydraulic scale and surface architecture. It is important that this distinction is fully explained, given that there are several inconsistencies in the literature that stem from attempts to compare geometric parameters at different hydraulic scales and dominant transport mechanisms.

D_h alone does not establish the dominant transport mechanism. Cross-scale interpretation must also consider pressure, G, q″, orientation, heating distribution, and wall and bulk temperatures relative to Tpc. Comparisons should examine buoyancy relative to inertia, thermal acceleration, and geometry-induced mixing using consistently defined parameters. Where operating conditions differ substantially, observed performance differences cannot be attributed uniquely to channel size. The scale–architecture matrix therefore identifies mechanisms requiring assessment, rather than assigning a universal dominant mechanism to each size category.

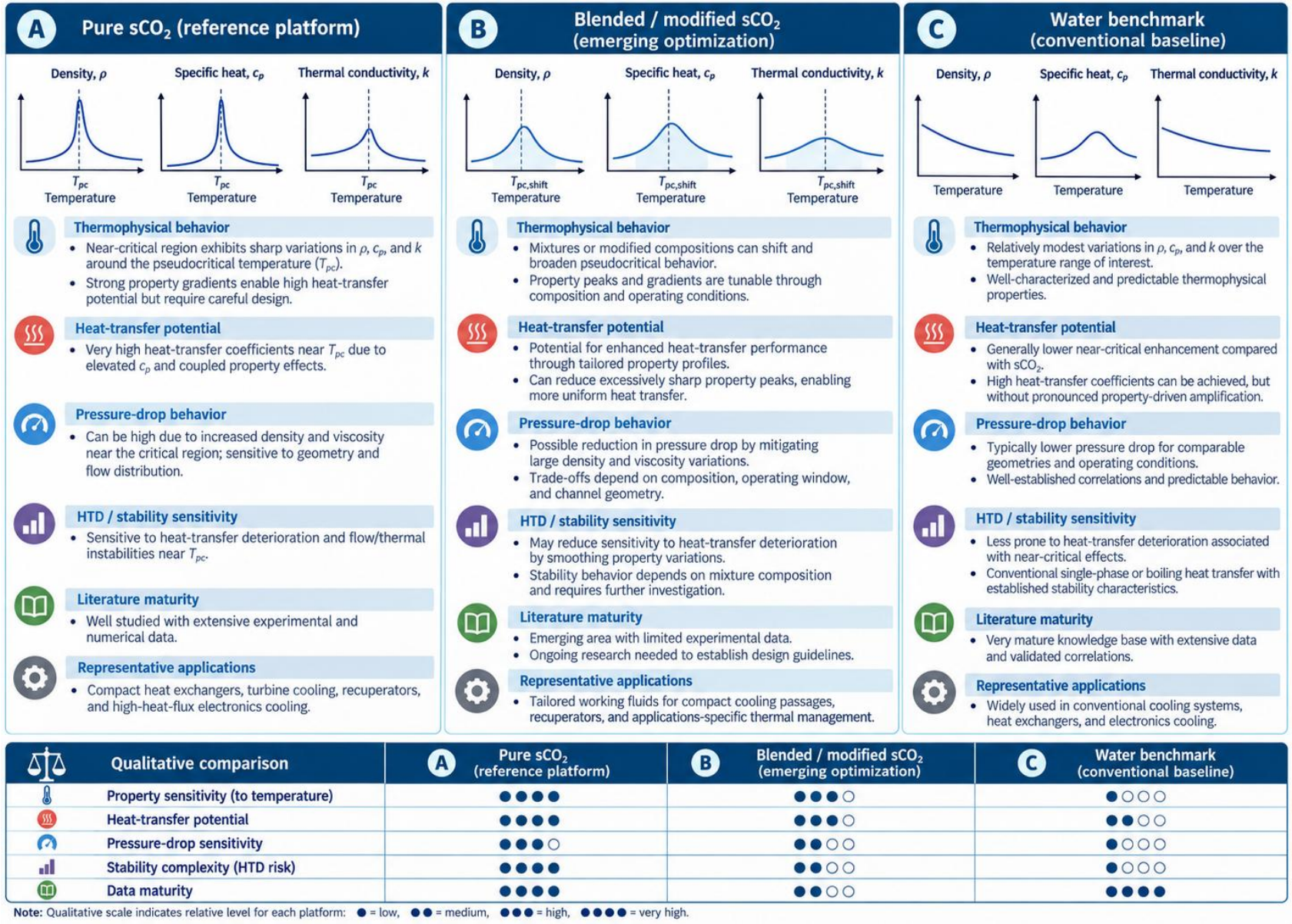


Figure 27. Fluid-platform and thermophysical trade-offs in compact sCO2 thermal systems [1,54,84].

https://doi.org/10.3390/en19215380

PCHE passages present another architectural issue. They contain small $D_{h,}$ but their performance is influenced by topology, bend angle, flow redistribution, header design, diffusion bonding, and manufacturing constraints. The advantage of a compact system in these systems is that the heat transfer density does not result in a significant increase in ΔP, maldistribution, or prediction uncertainty.

Finned, inserted, lattice, and roughened passages add further complexity. They are used to rejuvenate the near-wall layer, disrupt stratification, or inhibit HTD. However, they also alter the flow physics via wake interaction, swirl, secondary flows, surface roughness, and/or 3D mixing. Their design cannot be directly copied from smooth-tube or straight-channel correlations; therefore, it is important to have predictive tools which are both scale- and architecture-specific, as explained in Figure 28.

The scale-based interpretation in Figure 28 is summarised further in Table 10, which connects each architectural level with the dominant transport issue, design risk, type of correlation required, and future data needed. The table illustrates why the correlations cannot be assumed to be transferable across scales. The correlation derived for a smooth macro-scale tube cannot be directly applied to microchannels, PCHEs with bends, or lattice and AM passages with three-dimensional flow redevelopment.

5.4. Fin, Insert, and Passive-Enhancement Family Trade-Offs

Figure 29 presents the passive enhancement families, which should be chosen based on the dominant thermal limitation. The reviewed literature asserts that enhancement structures have different functions: some enhance the average h, others reduce the maximum wall temperature, while others reduce circumferential temperature non-uniformity and/or delay the onset of HTD.

Moderate enhancement is generally accomplished with moderate grooves, ribs, and concaves. They redistribute the near-wall flow and influence the thermal boundary layer while preventing excessive form drag. Their main benefit is that they deliver heat transfer improvement with a relatively low hydraulic penalty. Airfoil fins and optimised PCHE fins provide a more controlled enhancement route because their streamlined shape produces less wake loss than blunt obstacles. Therefore, they are applicable where there is a need to balance moderate heat transfer enhancement against ΔP control.

Pin fins and mini-ribs enable local mixing and are effective at hot-spot reduction. They can be used for high q″ cooling, although the blocking and form-drag effects should be carefully considered. When the primary concern is circumferential non-uniformity or buoyancy-driven stratification, twisted tapes are particularly advantageous. They generate swirl which can regenerate the near-wall layer and minimise thermal imbalance; however, they impose a substantial frictional penalty.

Lattice inserts and AM roughness are the most intensive techniques. Lattices generate high-intensity three-dimensional mixing and can significantly reduce wall temperature peaks, which is suitable for severe HTD mitigation. AM roughness provides heat transfer enhancement using surface structures created during the fabrication process, although they can also impose a significant frictional penalty. Thus, passive enhancement should be chosen not just to maximise Nu or h, but according to the specific failure mode that is being targeted.

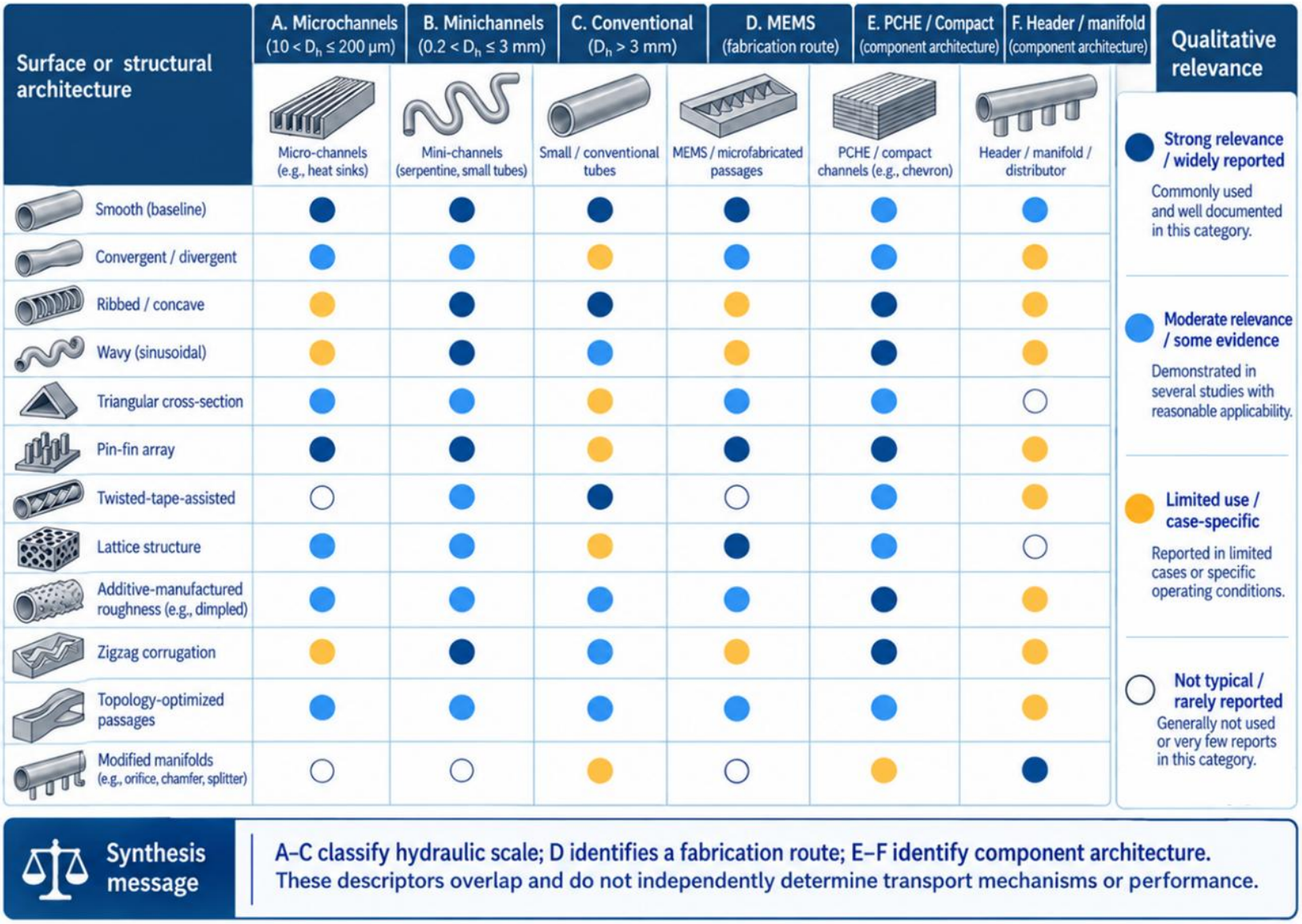


Figure 28. Hydraulic-scale and architecture classification of compact sCO_2 passages, synthesised from the reviewed literature [17,23,24,79,81].

Table 10. Scale–architecture relationships and correlation requirements.

Classification Axis and Category	Transport Mechanisms Requiring Assessment	Main Design Risk	Correlation Requirement	Future Data Needs
Hydraulic scale: conventional channels, $D_h > 3$ mm	Buoyancy, stratification, thermal acceleration	HTD at upper wall or heated side	Property-ratio and buoyancy-aware correlations	Local wall temperature and ΔP
Hydraulic scale: minichannels, $0.2 < D_h \leq 3$ mm	Compactness and local near-pseudo-critical transitions	Considerable sensitivity to q″, G and D_h	D_h-aware near-critical correlations	G, q″, p, D_h and local T/Tpc ranges
Hydraulic scale: microchannels, $0.01 < D_h \leq 0.2$ mm	Wall-normal gradients and one-sided heating	Correlation failure under local property variations	Local-property and heating-aware correlations	Wall and core temperature fields and uncertainty
Component architecture: PCHE	Bend-induced mixing, topology, maldistribution	High-f or poorly utilised channels	Geometry-specific Nu/f correlations	Header/channel flow distribution and off-design data
Enhancement features: fins and inserts	Wake mixing, swirl, boundary-layer renewal	Form drag and blockage	Coupled Nu–f–PEC correlations	Optimised spacing, pitch, blockage and ΔP
Enhancement features: lattices and AM surfaces	3D mixing and roughness-induced turbulence	High ΔP and manufacturability constraints	Structure-specific Nu/f/stability models	Roughness, porosity, density and mechanical data
System-level compact devices	Coupled thermal–hydraulic feedback	Instability, oscillation, corrosion, off-design drift	Component-level and transient correlations	Dynamic, material and application-specific validation



Figure 29. Trade-offs among fin and insert families in compact sCO_2 cooling passages [16,63,69,70,72,76,79,81].

https://doi.org/10.3390/en19215380

5.5. HTD and Stability Framework

Figure 30 helps to connect the geometry synthesis with the future-work roadmap. It demonstrates that HTD is not just a local phenomenon, but arises from a series of interacting processes. In the immediate vicinity of the pseudo-critical temperature, rapid changes in density, specific heat, viscosity, and thermal conductivity modify the near-wall flow layer. A low-density gas-like near-wall region can develop under strong or non-uniform heating, causing a reduction in the effectiveness of heat transfer in the near-wall region. This can cause an increase in wall temperature, a decrease in turbulent transport, and lead to deterioration.

This process may be enhanced or modified by buoyancy and thermal acceleration. This can cause deterioration at the top wall. In vertical flows, buoyancy interacts with flow direction, flow inertia, and ΔP distribution. Local geometry and heating asymmetry control the renewal or preservation of the near-wall layer in compact channels. Therefore, the impact of geometry relates to changes in the low-density near-wall layer of the wall, affecting its survival time and thickness.

Changes in local temperature and density may modify channel pressure differences and flow distribution. Whether this produces sustained oscillations depends on the coupled system, including its driving mechanism, hydraulic resistance, compressible volumes, and thermal response. Stability assessment should therefore distinguish forced circulation from natural circulation and specify the imposed pressure or flow boundary conditions. Lower steady wall temperatures or more uniform channel flow demonstrate thermal or distribution benefits; improved dynamic stability requires separate experimental or transient-simulation evidence.

This also emphasises the limitations of current correlations, as the average Nu under uniform, steady heating conditions may not predict wall temperature spikes, flow oscillations, or HTD onset under non-uniform heating conditions. Thus, each relevant variable that represents buoyancy, acceleration, local T/Tpc condition, q″/G, heating pattern, D_h, geometry, and stability thresholds must be included in future correlations.

5.6. Correlation Coverage and Limitations

The correlation database summarised in Appendix A provides a framework to predict sCO_2 heat transfer, f, and the onset of HTD under a variety of operational and geometrical conditions. However, the correlations examined should not be considered interchangeable. Their applicability depends on the geometry, heating method, pressure level, D_h, flow direction, G, q″, and the thermodynamic state corresponding to the pseudo-critical temperature. The main concern is not only the number of available correlations, but whether they provide adequate information to assess their validity for use in engineering.

The correlations in Appendix A can be divided into seven main families: classical turbulent-tube correlations, property-ratio and near-critical correlations, buoyancy and acceleration-modified correlations, compact-passage and PCHE-specific correlations, HTD-onset threshold correlations, friction-factor correlations, and enhanced-passage correlations. Conventional correlations, such as Dittus–Boelter, Petukhov, Gnielinski, and Winterton-type correlations, are valuable as reference correlations, as they provide simple Re–Pr relationships for turbulent convection. However, near the pseudo-critical region, their direct use is restricted as they do not consider rapid changes in density, specific heat, viscosity, thermal conductivity, buoyancy, and thermal acceleration. For these reasons, they should be used only for comparison or as a first approximation and not for final design of compact sCO_2 passages.

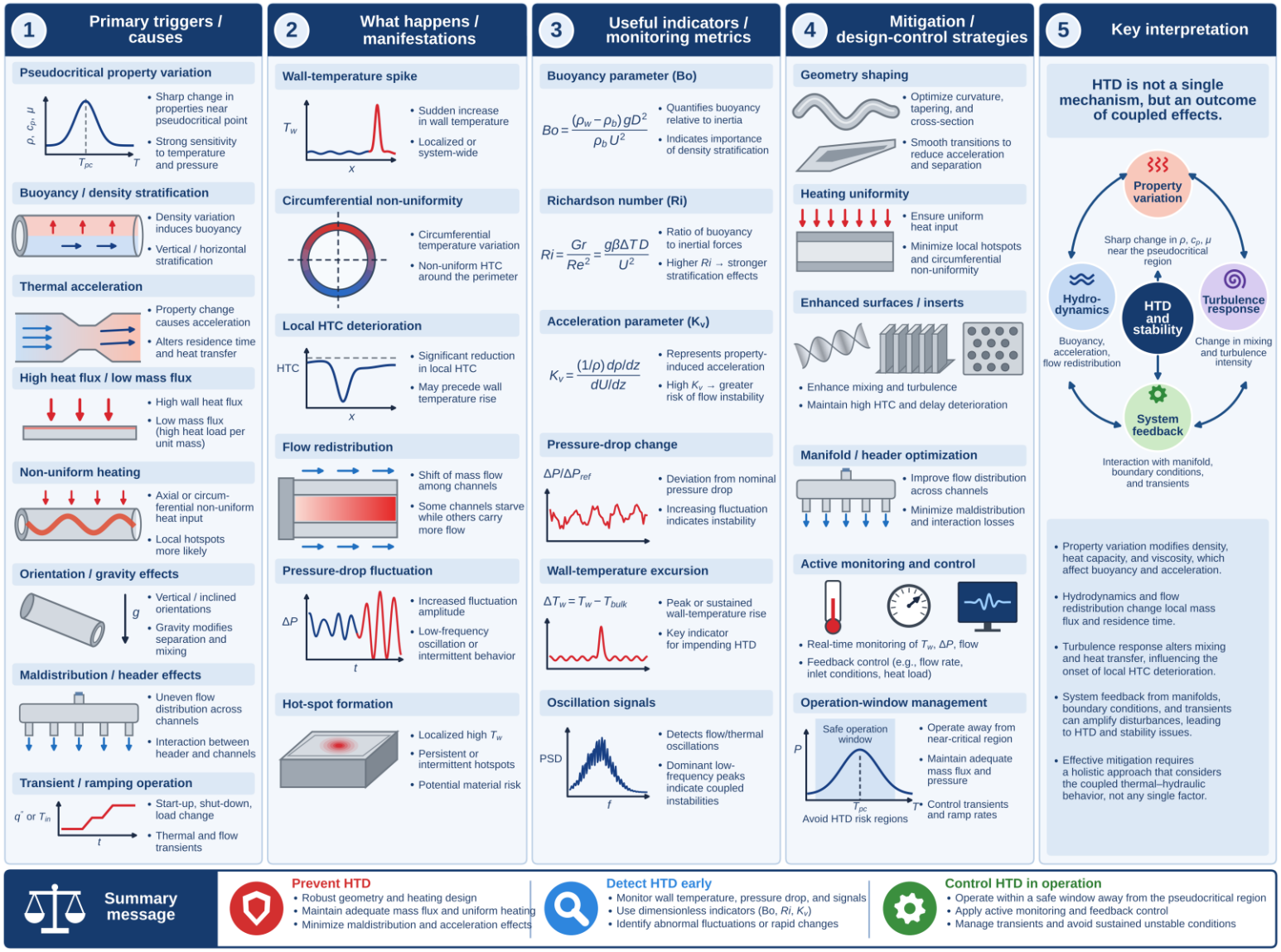


Figure 30. HTD and flow-stability framework for compact sCO_2 cooling passages [30,93,100,101,106].

The main drawback of property-ratio correlations is that they require additional correction terms, such as ϱw/ϱb, cp, w/cp, b, μw/μb, kw/kb, or temperature ratios relative to Tpc. These models are more appropriate for near-pseudo-critical tube flows because they consider strong property variations between the wall and bulk fluid. However, most are limited to circular smooth tubes and uniform-heating assumptions. Thus, they are unable to automatically consider one-sided heating, circumferential non-uniformity, curved passages, microchannels, PCHE bends or inserts, lattice structures, or AM roughness.

Published criteria provide configuration-specific screening limits. Zhang et al. [53] identified negligible buoyancy and acceleration effects below $Ri = 2.7 \times 10^{-3}$ and $Ac = 7.8 \times 10^{-8}$, respectively, for a horizontal minichannel under unilateral heating. For a compact receiver containing cylindrical fins under sidewall heating, Chen et al. [109] reported corresponding thresholds of $Ri = 5.7 \times 10^{-3}$ and $Ac = 5.8 \times 10^{-7}$. These values should retain their source-specific definitions and applicability limits; exceeding a significance threshold does not alone establish mechanism dominance or HTD onset. Furthermore, q″/G has units of J/kg and should be identified as a dimensional heat-to-mass-flux ratio, rather than a dimensionless criterion.

Compact-passage correlations are more useful in practice for compact heat exchangers because they can include a geometrical parameter, for example, channel angle, channel pitch, fin angle, curvature, channel-length ratio, and D_h. However, their transferability continues to be limited. A correlation derived for a straight PCHE channel should not be assumed to be valid for zigzag, wavy, S-shaped, airfoil-fin, topology-optimised, or lattice-enhanced passages. This restriction is particularly significant since prediction errors are relatively small for simpler channels, but can become substantial for zigzag or strongly enhanced passages. Accordingly, PCHE correlations should be considered valid only within the geometric and operating limits for which they have been developed.

The value of the HTD onset correlations is their ability to predict the onset of deterioration heat and the transition from normal to deteriorated heat transfer. Typically, these models depend on a q″ threshold, G effects, pressure ratio, D_h, or comparison with a reference h. However, most HTD-onset criteria are not accompanied by f predictions, wall temperature non-uniformity, transient instability, or system-level flow redistribution. Consequently, they have the ability to detect deterioration, although they may not accurately predict whether a compact component will be thermally and hydraulically stable.

The hydraulic part of the design problem is evaluated using f correlations. However, they are often not considered in conjunction with heat transfer correlations.

In compact sCO_2 systems, heat transfer enhancement may be accompanied by increased ΔP and pumping-power requirements. Its effect on dynamic stability requires separate experimental or transient-simulation evidence under the relevant system conditions. Thus, future models should not only predict heat transfer, but also provide coupled Nu–f, h–ΔP, PEC, wall temperature and stability data within established validity ranges.

Table 11 summarises the correlation families and their principal applicability limits. Reported errors are comparable only when the predicted quantity, error definition, and validation conditions are consistent. Calibration error does not establish accuracy for independent datasets or different geometries. The full equations, geometry and operating ranges, and applicability limitations are provided in Appendix A.

Table 11. Applicability limits and required upgrades for extensively used sCO_2 correlation families.

Correlation Family	Main Variables/Correction Terms	Applicability Strength	Main Limitation	Required Upgrade
Classical turbulent-tube correlations	Re, Pr, f, heating/cooling exponent	Useful baseline for smooth turbulent tubes	Weak near Tpc, under buoyancy, acceleration, HTD and non-uniform heating	Use only as reference; add near-critical and buoyancy corrections
Property-ratio/near-critical correlations	ϱw/ϱb, cp, w/cp, b, μw/μb, kw/kb, T/Tpc	Better representation of pseudo-critical property variation	Typically limited to smooth tubes and simple heating conditions	Add geometry, heating-pattern and local wall-state descriptors
Buoyancy/acceleration-modified correlations	Bu, Ac, Gr/Re^2, $Gr/Re^{2.7}$, q″/G, Ri-type terms	Useful for HTD-risk screening and mixed-convection interpretation	No universal threshold across orientation, D_h, pressure and heating mode	Standardise buoyancy/acceleration definitions and validate across scales
PCHE/compact-passage correlations	Re, Pr, f, channel angle, pitch, fin angle, D_h	More relevant to compact heat exchangers	Topology-specific; poor transferability between straight, zigzag, wavy, and airfoil passages	Develop separate validated Nu–f models for each PCHE topology
HTD-onset correlations	q_{onset}, G, Re, Pr, p/pc, D_h, h/h_{ref}	Identifies deterioration risk	Not coupled with friction, wall temperature non-uniformity or instability	Couple HTD threshold with Nu–f, wall temperature and stability criteria
Friction-factor correlations	Re, f, roughness, viscosity ratio, geometry factors	Provides hydraulic penalty estimate	Frequently separated from heat transfer and PEC analysis	Integrate with Nu/h, ΔP, pumping power and PEC
Enhanced-passage correlations	Roughness, pitch, blockage, fin spacing, bend angle, insert geometry	Covers selected enhancement mechanisms	Weak coverage for twisted tapes, lattices, AM roughness and combined enhancements	Build family-specific Nu–f–HTD–stability models with uncertainty limits

As presented in Table 11, a significant issue with the existing correlation data is not the lack of available equations, but that a limited number are only applicable to contemporary compact sCO_2 architecture. Classical correlations are beneficial for comparison with baseline results, whereas property-ratio and buoyancy-modified correlations provide enhanced predictive capabilities in the pseudo-critical region. Nonetheless, most available correlations do not entirely consider geometry-induced secondary flow, one-sided heating, local wall temperature non-uniformity, the effects of PCHE manifold, passive inserts, lattice structures, or AM roughness.

This is also crucial when using the large correlation database in Appendix A, as it explains why the database needs to be used cautiously. A correlation developed from smooth-tube data can be useful to determine physical scaling, but should not be applied directly to zigzag PCHEs or microchannel heat sinks unless the geometry, D_h, heating pattern, and operating window are incorporated in the calibration database. Equally, a correlation might perform well for a particular channel angle or topology, but ineffectively for another topology owing to the different local mixing, separation, wake interaction, and pressure recovery processes.

The main gap is the lack of coupled thermal–hydraulic prediction. Numerous correlations are available to predict Nu or h, whereas others predict f or ΔP. This separation is inadequate for compact sCO_2 systems because heat transfer enhancement, ΔP penalty, wall temperature control, and stability margin should be considered concurrently. For instance, passive inserts or roughened passages can increase Nu. However, if this enhancement comes with too large an increase in f, the system benefit may be negated. Accordingly, future correlations should provide Nu/h/f/ΔP, with preference given to including PEC, pumping-power requirements, wall temperature uniformity, and the onset of HTD.

A further significant limitation is the lack of validity ranges and uncertainty. For practical engineering applications, a correlation should include ΔP, G, q″, a range of Re, D_h, inlet state, wall and bulk temperatures in Tpc units, heating mode, geometry parameters, uncertainty, and prediction error. When these data are absent, the correlation cannot be safely extended to new or shorter passages. This is essential for ML-ready databases and future hybrid Computational Fluid Dynamics (CFD)–correlation– machine learning (ML) models, as incomplete metadata can limit both conventional model validation and data-driven prediction.

Appendix A should be considered a correlation inventory, rather than as a full engineering design database. Its value is in bringing together the available predictive tools and demonstrating the progression of the field from classical Re–Pr correlations to property-ratio, buoyancy-aware, acceleration-aware, PCHE-specific, and HTD-threshold models. The main drawback is that numerous correlations are geometry-specific, have limited operating ranges, and are poorly documented. As a result, this underlines the need for data-driven and physics-informed prediction methods, which are discussed in the next subsection.

5.7. Data-Driven and Physics-Informed Prediction of Compact sCO_2 Heat Transfer

The limitations discussed in Section 5.6 show that conventional semi-empirical correlations are useful for baseline interpretation, although their transferability is limited under significant pseudo-critical property variations, compact geometry, non-uniform heating, passive enhancement, and HTD. These restrictions have led to the development of data-driven and hybrid modelling methods to predict sCO_2 heat transfer. The main reason is that transport of sCO_2 near the pseudo-critical region is extremely nonlinear. Small changes in pressure, wall temperature, bulk temperature, q″, or D_h can give rise to large variations in density, specific heat, viscosity, thermal conductivity, buoyancy, and

thermal acceleration. These coupled effects are difficult to reproduce employing a single universal closed-form correlation.

Wen et al. [125] used machine-learning techniques to predict sCO_2 heat transfer in the pseudo-critical zone. They showed that artificial neural networks (ANNs) and XGBoost can capture nonlinear HTD trends when the bulk temperature approaches or exceeds Tpc. The ANN model achieved an R^2 of approximately 0.995 for new data, although prediction accuracy decreased in some regions below Tpc. This finding denotes that ML can reproduce nonlinear HTD behaviour. However, its reliability remains sensitive to data distribution, thermal-regime coverage, and extrapolation beyond the training range.

In addition, the ML approach has been applied to numerical databases and geometry-specific design variables to enable compact heat exchanger design. Using numerical modelling and machine-learning analysis, Wen et al. [84] investigated the local flow and heat transfer characteristics of supercritical CO_2 mixtures in sinusoidal wavy-channel PCHEs. This study is directly applicable to the design of compact sCO_2 systems, connecting mixture properties, local channel geometry, and thermal–hydraulic response. Nonetheless, the accuracy of those models continues to be dependent on mixture composition, channel topology, and the CFD database of models used to develop the models.

An approach to transfer-learning and deep-learning frameworks based on multi-fidelity data was proposed by Shi et al. [126], with the aim of predicting supercritical CO_2 heat transfer behaviour under a wider range of working conditions. Most importantly, these approaches intend to lower the cost of producing large high-fidelity datasets by using data of varying fidelities. This is effective for optimisation of compact channels, where full CFD campaigns are expensive. However, consistency between the multi-fidelity datasets, data distribution, and validation range is important, as an ML model can only generalise when the low- and high-fidelity data represent uniform underlying physics.

Interpretable ML has also been applied in the field of supercritical-fluid heat transfer. Under specified q″ and given wall temperature boundary conditions, Li et al. [127] predicted the heat transfer characteristics of SFs using interpretable ML and back-propagation neural networks. This work is useful, as it moves ML beyond simple regression to physical interpretation of the effect of the input variables. However, the interpretability of these models depends on particular descriptors, the quality of the training database, and whether the input variables adequately describe near-wall property variations, buoyancy, acceleration, and thermal boundary conditions.

Another emerging application area concerns dynamic and off-design conditions. Shao et al. [128] used ML techniques to simulate supercritical CO_2 heat transfer performance in ocean rolling conditions. This is important because the time-dependent inertia, flow redistribution caused by rolling motion, and the thermal–hydraulic coupling can influence system behaviour. These studies demonstrate the ability to expand the scope of ML beyond steady-state tube or channel datasets. However, the models developed for rolling tubes are not directly applicable to PCHEs, microchannels, twisted tapes, or lattice passages without further testing.

Neural-network surrogates trained with CFD are also developing rapidly. In their study, Ao et al. [129] presented a deep-learning-based rapid prediction approach for 3D sCO_2 flow and heat transfer in semi-circular tube sections, based on a feedforward neural network trained on numerical data. This surrogate is effective because it can reduce computational costs when several CFD evaluations are required during the design optimisation process. Nonetheless, its accuracy is dependent on the CFD setup,

turbulence model, boundary conditions, and range of geometries characterised in the training data.

Experimental data-driven ML is also crucial. Grabowski et al. [130] developed a technique to train ML models using experimental sCO_2 heat transfer data to predict performance under heat transfer conditions. This direction is useful given that experimental databases contain real measurement uncertainty and system responses. Moreover, it identifies a significant drawback associated with compact sCO_2 ML, as many experimental studies fail to report the parameters of ΔP, G, q″, D_h, wall temperature, local property evaluation, and uncertainty in sufficient detail.

Table 12 summarises these developments by listing representative ML-assisted and data-driven studies. The field has evolved from basic ANN-based heat transfer regression to XGBoost, Random Forest, support vector regression (SVR), transfer learning, interpretable ML, and CFD-trained neural-network surrogates. It also demonstrates that most models are dependent on the geometry and dataset used for training.

The studies summarised in Table 12 should be assessed by distinguishing interpolation accuracy, extrapolation capability, and physical consistency. A high R^2 within a sampled operating range does not, by itself, demonstrate that a model captures the mechanisms governing HTD. Validation should establish whether the test data represents independent experiments or simulations, rather than neighbouring points from cases also used for training. Where local measurements or CFD samples originate from the same operating case, withholding complete cases provides a more demanding assessment of generalisation.

Transferability should be evaluated separately across pressure, mass flux, heat flux, thermodynamic regime, and geometry. A model tested within its training range cannot be assumed to predict an unseen HTD regime or a different channel topology. Where independent tests outside the training domain are unavailable, its demonstrated applicability should remain restricted to the evaluated conditions. Claims of physical learning should also be supported by tests of conservation, limiting behaviour and sensitivity to relevant dimensionless parameters; feature importance alone is insufficient evidence.

For engineering use, prediction errors should therefore be reported separately for normal heat transfer and deterioration, together with training-domain boundaries and uncertainty estimates. Models intended for design should additionally be assessed against independent experimental data and applicable correlations. This assessment would distinguish useful interpolation tools from models with demonstrated predictive capability beyond their calibration domain.

Finally, future ML models for compact sCO_2 systems should implement multi-output and physics-informed methods. The inputs should include Re, Pr, ΔP, G, q″, q″/G, D_h, T/Tpc, wall-to-bulk property ratios, buoyancy indicators (Gr/Re^2 or Bu), acceleration parameters, Richardson-type indicators, geometry ratios, roughness parameters, fin pitch, bend angle, and heating-pattern descriptors. The outputs should include Nu, h, f, ΔP, pumping-power penalty, peak wall temperature, uniformity, onset of HTD, and stability margin, in addition to PEC.

Table 12. Representative ML-assisted and data-driven studies for sCO_2 heat transfer prediction.

Study	ML/Data-Driven Method	Data Source/Configuration	Main Inputs	Main Outputs	Main Contribution	Main Limitations of Compact sCO_2 Design
Wen et al. [125]	ANN, XGBoost, and other ML regressors	sCO_2 heat transfer database near pseudo-critical conditions	Operating parameters and thermophysical descriptors near Tpc	Heat transfer prediction and HTD tendency	Demonstrated ANN and XGBoost can predict nonlinear HTD behaviour near or above Tpc; ANN achieved $R^2 \approx 0.995$ on new data	Accuracy decreased in some regions below Tpc; prediction remains sensitive to data distribution and thermal-regime coverage
Wen et al. [84]	SVR, ANN, Random Forest, XGBoost	Numerical database for sCO_2 mixtures in sinusoidal wavy-channel PCHEs	Mixture composition, local flow variables, geometry descriptors, thermal state	Local flow and heat transfer characteristics	Extended ML prediction to compact PCHE-type channels and CO_2 mixtures	Reliability depends on CFD database, mixture range and selected channel topology
Shi et al. [126]	Transfer learning and deep learning using multi-fidelity data	Combined low- and high-fidelity data for sCO_2 heat transfer behaviour	Operating and thermal descriptors within working conditions	Rapid prediction of sCO_2 heat transfer behaviour	Transfer learning improved prediction over wider operating ranges while reducing demand for high-fidelity data	Multi-fidelity consistency, training-data distribution and validation range remain critical
Li et al. [127]	Interpretable ML and BPNN models	Supercritical-fluid heat transfer datasets under given q″ and wall temperature conditions	Flow, thermal and property-related variables	h and heat transfer characteristics	Introduced interpretable ML to analyse supercritical-fluid heat transfer under different boundary conditions	Explainability depends on selected descriptors and quality of training data
Shao et al. [128]	ML models combined with numerical and experimental interpretation	sCO_2 heat transfer under ocean rolling conditions	Rolling condition, flow and thermal descriptors, operating parameters	Heat transfer performance under dynamic motion	Extended ML prediction to dynamic marine/offshore-type conditions	Primarily valid for the studied rolling-tube configuration; transfer to PCHEs; enhanced passages requires validation
Ao et al. [129]	Feedforward neural-network surrogate	Numerical database for semi-circular sCO_2 tube sections	Geometry, operating conditions and local thermal–flow variables	Rapid 3D prediction of sCO_2 flow and heat transfer	Demonstrated fast CFD-trained prediction of 3D sCO_2 flow and heat transfer	Accuracy depends on CFD assumptions, boundary conditions and training-domain coverage
Grabowski et al. [130]	ML model trained on experimental heat transfer data	Experimental sCO_2 heat transfer database	Experimental operating variables and thermal descriptors	Prediction of new heat transfer Correlation	Demonstrated the value of ML to reproduce experimental trends and support additional data generation	Substantially dependent on experimental data quality, metadata completeness and uncertainty reporting

For this reason, further research should move beyond black-box modelling toward an integrated CFD–experiment–correlation–ML framework. Experimental data should validate the results and provide uncertainty limits, CFD should provide detailed local fields and controlled parametric variation, classical correlations should provide dimensionless physical scaling, and ML should accelerate interpolation, optimisation, and sensitivity analysis. Physics-informed ML can assist compact sCO_2 design by modelling nonlinear interactions, screening candidate geometries, predicting HTD risk, and supporting the development of the geometry-specific correlations. These models are required to clearly report their training range, input variables, uncertainty, and the extrapolation limits. If these safeguards are not in place, ML predictions could experience the same limited-transferability issues as current conventional correlations.

5.8. Future Research Roadmap

Figure 31 summarises the directions for further research identified in this review. The challenge is not only the need for further research, but also the absence of comparable, standardised and transferable data. Many compact geometries and enhancement structures have been shown in the literature to be promising, although the reported metrics are not always consistent. Some studies describe significant heat transfer enhancement without appreciable friction losses; however, others fail to provide local wall temperature distributions or ΔP data. Additionally, several correlations are presented without complete validity ranges or uncertainty/error bands. These variations make reliable comparisons difficult and limit the development of general design guidelines.

Standardised reporting is the main priority. Further research should include Re, Pr, ΔP, G, q″, D_h, wall and bulk temperatures with respect to Tpc, heating distribution, geometric parameters, Nu or h, f or ΔP, PEC, uncertainty, and stability behaviour. If these parameters are not included, the data cannot be used to support development of robust correlations or machine-learning models.

Coupled Nu–f–HTD modelling is the second priority. Heat transfer enhancement cannot be assessed independently of the ΔP penalty, the cost of pumping power, wall temperature uniformity, and stability margin. In relation to compact sCO_2 devices, the effect of HTD and flow oscillations must be evaluated both thermally and hydraulically for the reason that these systems frequently operate near deterioration and instability thresholds.

The third priority is the development of geometrically aware models. Smooth-tube correlations should not be applied directly to microchannels, PCHEs, ribs, tapes, lattices, or AM roughness. Each architecture should be validated using a suitable range of parameters and, where possible, within a common dimensionless framework, which consists of geometry ratios, heating conditions, and property-variation terms.

Heating-aware prediction is the fourth priority. Numerous practical systems are subject to one-sided, circumferentially non-uniform, localised, or transient heating. Thus, future correlations and CFD validation studies should comprise heating-pattern descriptors and local wall-position data.

The fifth priority is stability-integrated design. Future models should integrate ΔP feedback, mass-flow oscillations, flow maldistribution, natural-circulation behaviour, and off-design operation of the heat transfer device. This is essential with respect to compact recuperators, receivers, nuclear systems, and dynamic thermal management devices.

The sixth priority is physics-informed AI and hybrid modelling. When ML models are trained on standardised databases with recognised uncertainty and operating limits, they can accelerate optimisation. Inputs to physics-informed ML should be dimensionless and comprise variables such as Re, Pr, Bu, Ac, Ri, q″/G, T/Tpc, geometry ratios, roughness

parameters, and heating-pattern indicators. In addition to prediction accuracy, models should report extrapolation limits and uncertainty.

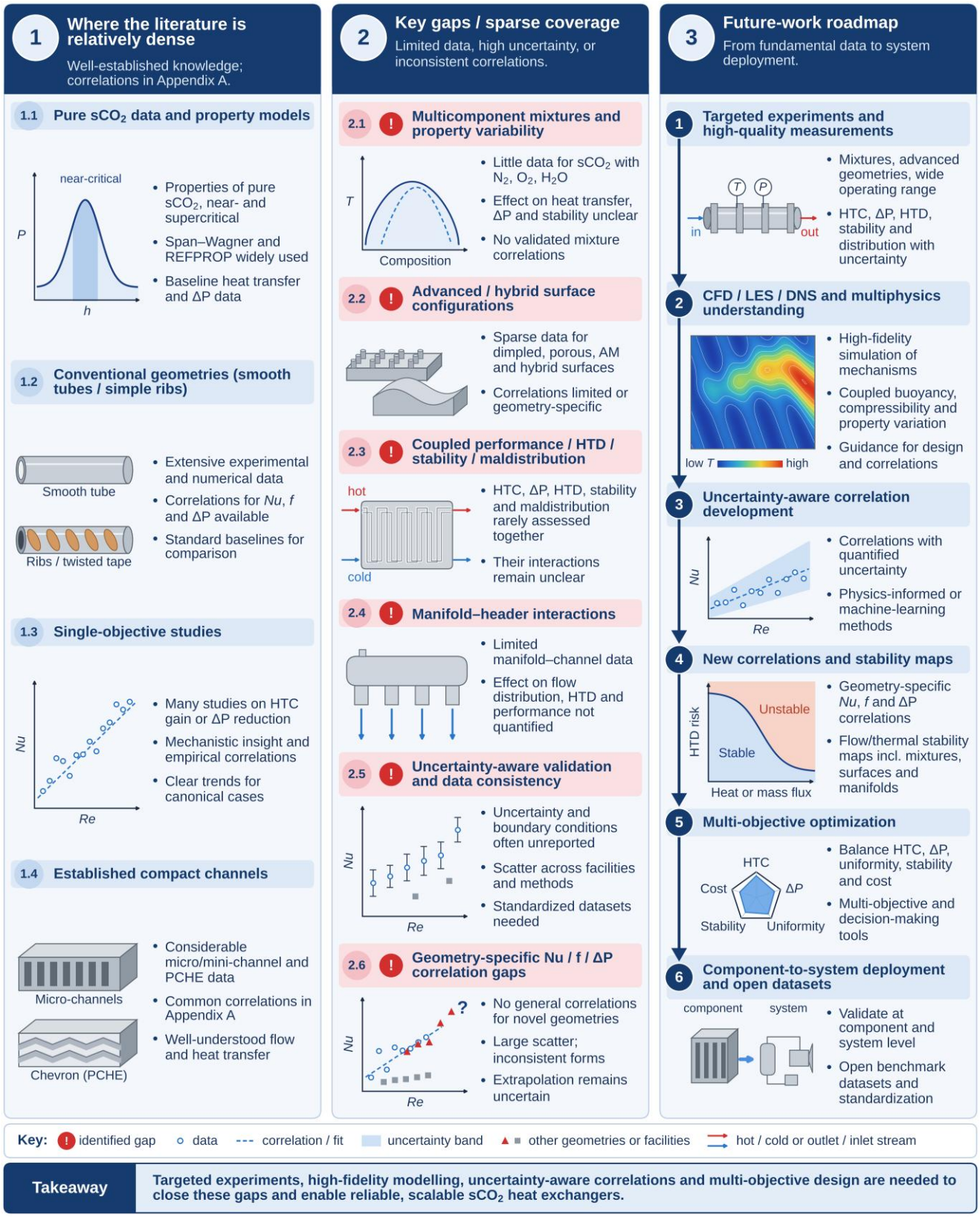


Figure 31. Literature gaps, correlation coverage in Appendix A and future-work roadmap for compact sCO_2 thermal systems.

Table 13 summarises the future-work roadmap shown in Figure 31. Table 13 identifies the practical research directions required to tackle the gaps, unlike the previous analysis, which concentrates on the limitations of existing correlations. The following priorities are recommended as a guide for future experimental, numerical, correlative, and AI-supported studies.

Table 13 emphasises the need for more than just isolated experiments or CFD cases in the future. The most important requirement is the need for a common reporting format so that results obtained from various geometries, scales, and applications can be compared based on common thermal–hydraulic and stability parameters. This is fundamental to establish correlations and ML models that can be transferred between compact sCO_2.

Table 13. Future research priorities identified from Figures 26–31.

Priority	Current Limitation	Required Development	Expected Benefit
Standardised reporting	Studies report different variables and incomplete operating ranges	Report Re, Pr, p, G, q″, D_h, T/Tpc, geometry, heating mode, Nu/h, f/ΔP, PEC and uncertainty	Enables fair comparison and database construction
Coupled thermal–hydraulic assessment	Heat transfer gain is often separated from ΔP penalty	Report Nu/h together with f/ΔP, pumping power, PEC and wall temperature uniformity	Prevents misleading ranking based only on h
Geometry-specific correlations	Tube correlations are frequently transferred to compact geometries	Develop separate correlations for tubes, microchannels, PCHEs, inserts, lattices and AM passages	Improves prediction reliability
Heating-aware prediction	One-sided and non-uniform heating are poorly represented	Include axial/circumferential q″ distribution and wall-location effects	Improves local hot-spot and HTD prediction
HTD/stability integration	Deterioration and oscillation are often treated separately	Couple q_{onset}, wall temperature, ΔP feedback, mass-flow oscillation and maldistribution	Improves safe operation near Tpc
PCHE system co-design	Passage and header design are often optimised separately	Optimise channel, header, manifold and operating point together	Reduces maldistribution and improves exchanger utilisation
Passive-enhancement optimisation	Strong enhancement frequently increases friction	Use Nu–f–PEC–stability optimisation for ribs, tapes, lattices and roughness	Identifies useful enhancement rather than maximum disturbance
Hybrid CFD–ML modelling	Existing datasets are not ML-ready	Develop standardised CFD and experimental databases with uncertainty and extrapolation checks	Enables rapid, reliable optimisation

6. Conclusions

This review synthesises the thermo–hydraulic behaviour of supercritical CO_2 in compact thermal systems and establishes a coherent framework relating transport mechanisms, geometry, enhancement strategies and system-level performance to a wide range of configurations.

The principal finding is that heat transfer behaviour in sCO_2 systems is controlled by the coupled interaction of pseudo-boiling, buoyancy-driven stratification, and thermal acceleration, as opposed to any single dominant mechanism. These effects, particularly marked near the pseudo-critical region, restructure near-wall turbulence, promote partial relaminarisation, and drive HTD. Accordingly, HTD should be regarded as a primary design constraint, not an edge-case anomaly.

Geometry functions as a first-order control parameter, although its effectiveness is intrinsically conditional. Straight tubes provide the mechanistic baseline; however, they are also the most susceptible to deterioration. Curved and serpentine passages can suppress stratification by way of secondary flows, while tapered and profiled geometries modify the trade-off between heat transfer and pressure drop instead of improving both entirely. In micro and minichannels, correlation applicability depends on the combined effects of hydraulic diameter, operating state, and heating conditions; reduced size alone does not establish stronger property gradients or correlation failure.

In terms of PCHEs, performance is governed by multi-scale coupling where local channel topology controls mixing and heat transfer intensity, whereas headers, flow routing and operating conditions determine whether these gains are realised at the system level. Advanced configurations, such as zigzag, airfoil and topology-optimised passages deliver substantial improvements in compactness and thermal duty, but only when channel and manifold designs are considered as an integrated system. Application-specific constraints, including fluid composition, dynamic operation, and material compatibility, also define the feasible operating range.

Passive enhancement strategies consistently improve thermal performance by disrupting the low-density near-wall layer responsible for HTD. Enhancement structures may introduce hydraulic penalties, while their effects on flow distribution and dynamic stability require separate assessment under the relevant system conditions. Therefore, the most effective designs are those that achieve a balanced compromise between heat transfer enhancement, pressure-drop cost and thermal stability, rather than maximising Nusselt number.

Predictive reliability remains limited by the transferability of correlations across fluids, geometries, heating conditions, and thermodynamic regimes. Their use requires checking the original calibration ranges and validation evidence. Further development should incorporate relevant transport mechanisms and geometry and heating effects, supported by independent validation.

Author Contributions: Conceptualization, A.A. and J.M.; methodology, A.A. and J.M.; formal analysis, A.A., M.I. and J.M.; investigation, A.A., M.I. and J.M.; resources, A.A.; data curation, M.I.; writing—original draft preparation, A.A., M.I. and J.M.; writing—review and editing, A.A., M.I. and J.M.; visualization, J.M.; supervision, A.A.; project administration, A.A. All authors have read and agreed to the published version of the manuscript.

Funding: This research received no external funding.

Data Availability Statement: No new data were created or analyzed in this study. Data sharing is not applicable to this article.

Conflicts of Interest: The authors declare no conflicts of interest.

Nomenclature

Symbol	Definition	Unit
A	Heat transfer surface area	m^2
Ac	Thermal acceleration parameter	–
AR	Aspect ratio of channel cross-section	–
Bu	Buoyancy parameter	–
c_p	Specific heat at constant pressure	J/kg K
D	Diameter or characteristic length	m
D_h	Hydraulic diameter	m
AM	Additive Manufacturing	-
f	Friction factor	–

G	Mass flux	Kg/m² s
h	Convective heat transfer coefficient	W/m² K
k	Thermal conductivity	W/m K
Nu	Nusselt number	–
p	Pressure	Pa
PCHEs	Printed circuit heat exchangers	-
PEC	Performance evaluation criterion	–
HTD	Heat transfer deterioration	
CFD	Computational fluid dynamics	-
ML	Machine learning	-
ANN	Artificial Neural Network	-
AI	Artificial intelligence	-
SMR	Small modular reactor	-
LBE	Lead–bismuth eutectic	-
LCOE	Levelized cost of electricity	-
SVR	Support vector regression	-
Pr	Prandtl number	–
q″	Wall heat flux	W/m²
q″/G	Heat-to-mass-flux ratio	J/kg
Re	Reynolds number	–
Ri	Richardson number	–
T	Temperature	K
Tpc	Pseudo-critical temperature	K
ΔP	Pressure drop	Pa
η	Thermal performance index	–
ϱ	Density	kg/m³
μ	Dynamic viscosity	Pa s
ν	Kinematic viscosity	m²/s

Greek Symbols

Symbol	Definition	Unit
α	Thermal diffusivity	m²/s
β	Thermal expansion coefficient	1/K
θ	Inclination angle	°
λ	Thermal conductivity (alternate symbol)	W/m K

Subscripts and Superscripts

Symbol	Definition
b	Bulk value
in/out	Inlet/outlet
pc	Pseudo-critical
w	Wall
avg	Average
max/min	Maximum/minimum

Appendix A. Correlation Database for Heat Transfer and Friction in sCO_2 Compact Passages

Authors	Equation	Geometry and Operating Range	Applicability and Limitations
Kim and Kim [30]	$Nu_w = 0.226 Re_b^{1.174} PP_b^{1.057} \left(\frac{\rho_w}{\rho_b}\right)^{0.571} \left(\frac{\overline{C_p}}{C_{p,b}}\right)^{1.032} Ac^{0.489} Bu^{0.0021}$ $Ac = \frac{q^+}{Re_b^{0.625}} \left(\frac{\mu_w}{\mu_b}\right) \left(\frac{\rho_b}{\rho_w}\right)^{0.5}$ $Bu = \frac{Gr_q}{Re_b^{3.425} Pr^{0.8}} \left(\frac{\mu_w}{\mu_b}\right) \left(\frac{\rho_b}{\rho_w}\right)^{0.5}$	Vertical circular tube; upward CO_2 flow. D = 4.5 mm; p = 7.46–10.26 MPa; bulk T = 29–115 °C; q″ = 38–234 kW/m²; G = 208–874 kg/(m²·s).	Heating; buoyancy and acceleration corrections.
Chen et al. [109]	$Nu_{c,bot} = 0.075 Re^{0.8} Pr^{-0.307} \left(\frac{T_b}{T_{w.bot}}\right)^{0.553}$ $Nu_{c,top} = 0.158 Re^{0.8} Pr^{0.515} \left(\frac{T_b}{T_{w.top}}\right)^{6.951}$	Vertical upward CO_2 in a straight reference tube and expanding adaptive channels; heated length 1.00 m; 0.20 m adiabatic inlet/outlet extensions. Straight ID 4 mm; illustrated adaptive channel expands from ID 2 to 6 mm. Study coverage: p = 7.5–10 MPa; inlet T = 15–25 °C; heat flux = 35–65 kW/m²; mass flow = 5.03–7.54 g/s; adaptive-length fraction la/L = 0–1. These are study conditions, not validity limits for the listed equations.	SST k–ω; upward heating and conjugate wall conduction.
Shi et al. [123]	$Nu = 0.0986 Re^{0.687} P_r^{0.4} \left(\frac{\mu_b}{\mu_w}\right)^{0.14}$ $f = 0.513 Re^{-0.667}$	Airfoil-fin PCHE; 400 mm model length; fin length × width × height = 4 × 1 × 1.5 mm; longitudinal/transverse/staggered pitches = 8/3/4 mm; CO_2 at 20 MPa. Re = 11,671–123,483; Pr = 0.73–0.75; μb/μw = 1.03–1.09. Fluid T = 779–1073 K; inlet T = 873–1073 K.	Listed equations are the CO_2 fits for the airfoil channel, far from Tpc. RNG k–ε with enhanced wall functions; properties vary with temperature at fixed 20 MPa. Darcy friction convention.
Kim et al. [124]	$Nu = (0.0292 \pm 0.0015) Re^{0.8138 \pm 0.0050}$ $f = (0.2515 \pm 0.0097) Re^{-0.2031 \pm 0.0041}$, fin angle 32.5° $Nu = (0.0188 \pm 0.0032) Re^{0.8742 \pm 0.0162}$ $f = (0.2881 \pm 0.0212) Re^{-0.1322 \pm 0.0079}$, fin angle 40.0°	Zigzag PCHE; semicircular hot/cold passages of diameter 1.9/1.8 mm; hydraulic diameter 1.15 mm. CFD models use the same fin angle on both sides: 32.5° or 40°. 32.5° fit: 2000 < Re < 58,000; 40° fit: 2000 < Re < 55,000; 0.7 < Pr < 1.0 for both.	Angle-specific CFD fits, combining hot- and cold-side results; SST k–ω and REFPROP properties. Narrow Pr interval reflects recuperator conditions;

			coefficient-fit uncertainty is not prediction error.
Bringer and Smith [131]	$Nu_b = 0.0375Re_x^{0.77}Pr_w^{0.55}$	Circular-tube turbulent flow; CO_2 form of Bringer and Smith ID = 0.18 in. (4.572 mm); p = 1200 psia (about 8.274 MPa); bulk T = 70–120 °F (21.1–48.9 °C); Re = 30,000–300,000.	Coefficient 0.0375 is for CO_2; the survey gives 0.0266 for water. Nu and Re use the characteristic temperature tx, selected from tb, tpc or tw according to (tpc − tb)/(tw − tb); Pr uses wall temperature. The original model does not account for the thermal-conductivity peak near Tpc.
Yoon et al. [132]	$Nu_b = 0.14Re_b^{0.69}Pr_b^{0.66}$, when $T_b/T_{pc} > 1$ $Nu_b = 0.013Re_bPr_b^{-0.05}\left(\frac{\varrho_{pc}}{\varrho_b}\right)^{1.6}$, when $T_b/T_{pc} \leqslant 1$	Horizontal copper tube; CO_2 cooling. ID = 7.73 mm; inlet p = 7.5–8.8 MPa; G = 225, 337 and 450 kg/(m²·s).	Cooling; separate branches for Tb/Tpc > 1 and ≤1.
Oh and Son [133]	$Nu_b = 0.023Re_b^{0.7}Pr_b^{2.5}\left(\frac{c_{p,b}}{c_{p,w}}\right)^{-3.5}$, when $T_b/T_{pc} > 1$ $Nu_b = 0.023Re_b^{0.6}Pr_b^{3.2}\left(\frac{\varrho_b}{\varrho_w}\right)^{3.7}\left(\frac{c_{p,b}}{c_{p,w}}\right)^{-4.6}$, when $T_b/T_{pc} \leqslant 1$	Horizontal stainless-steel circular tubes; CO_2 cooling. IDs = 4.55 and 7.75 mm; G = 200–600 kg/(m²·s); inlet p = 7.5–10.0 MPa; inlet T = 90–100 °C.	Cooling; oil-free loop; separate branches for Tb/Tpc > 1 and ≤1.
Kuang et al. [134]	$Nu = 0.022186Re^{0.8}Pr^{0.3}\left(\frac{\varrho_r}{\varrho_w}\right)^{-1.4652}\left(\frac{\bar{c}_p}{c_{p,w}}\right)^{0.0832}$	Aluminium microchannel tube with 11 circular ports; port ID 0.79 mm; CO_2 gas cooling. Experimental coverage: p = 8–10 MPa; G = 300–1200 kg/(m²·s).	The listed equation is Huai's earlier model reproduced for comparison, with coefficient 0.001546; match its own heat-capacity averaging convention.
Lee et al. [135]	$Nu = \frac{Re_b^{0.56}Pr^{0.27}\left(\frac{c_{p,b}}{c_{p,w}}\right)^{0.2}\ \text{when } T_b}{T_{pc}} > 1$ $Nu = Re_b^{0.35}Pr^{0.20}\left(\frac{c_{p,b}}{c_{p,w}}\right)^{-3}\ \text{when } T_b/T_{pc} \leqslant 1$	CO_2 gas cooler with a micro-fin tube, ID 4.6 mm and OD 5.0 mm; dimensions reported in the supplied publisher abstract. Cooling pressures discussed in the supplied abstract: 8.0 and 10.0 MPa.	Cooling; micro-fin geometry. Available evidence is an abstract excerpt, not the complete paper.
Gupta et al. [136]	$Nu = 0.0038Re_w^{0.957}Pr_w^{0.139}\left(\frac{\mu_w}{\mu_b}\right)^{-0.222}\left(\frac{\varrho_w}{\varrho_b}\right)^{0.836}\left(\frac{k_w}{k_b}\right)^{-0.754}$	Vertical Inconel-600 bare tube; ID = 8 mm; heated length = 2.208 m; outlet p = 7.4–8.8	Cooling; upward CO_2 flow.

		MPa; G = 900–3000 kg/(m²·s); inlet T = 20–40 °C; q″ = 15–615 kW/m².	
Huai and Koyama [137]	$Nu = 0.022186Re^{0.8}Pr^{0.3}\left(\frac{\varrho_r}{\varrho_w}\right)^{-1.4652}\left(\frac{\bar{c}_p}{c_{p,w}}\right)^{0.0832}$	Horizontal extruded aluminium multiport section, effective length 500 mm, width 20 mm and thickness 2 mm; equivalent hydraulic diameter 1.31 mm; CO_2 cooling. p = 7.4–8.5 MPa; bulk-mean T = 22–53 °C; G = 113.7–418.6 kg/(m²·s); heat flux magnitude = 0.8–9 kW/m².	CO_2 cooling using water-cooled copper blocks on both sides. Nu, Re and Pr are evaluated using bulk-mean properties. Application should retain the source-defined property ratios and coefficient precision.
Kim et al. [138]	$Nu_b = Nu_{var} \cdot f(B)$ $f(B) = \begin{cases} (0.8 + 6 \cdot 10^6 B)^{-0.8} \text{ when } B \leqslant 7 \cdot 10^{-8} \\ 0.261 + 3.068 \cdot B^{0.1} \text{ when } 7 \cdot 10^{-8} \leqslant B \leqslant 7 \cdot 10^{-7} \\ 1.47 - 6.7 \cdot 10^5 \cdot B \text{ when } 7 \cdot 10^{-7} \leqslant B \leqslant 10^{-6} \\ 0.8 \text{ when } 10^{-6} \leqslant B \leqslant 10^{-5} \\ 0.1423 \cdot B^{-0.15} \text{ when } 10^{-5} \leqslant B \end{cases}$ $B = \frac{\overline{Gr}}{Re_b^{2.7}\overline{Pr}^{0.5}}$	Vertical upward CO_2 in an internally heated annulus; unheated outer tube ID 10 mm, inner heater rod OD 8 mm; heated length 1.80 m. Heated-perimeter equivalent thermal diameter 4.5 mm. Inlet p = 7.75 and 8.12 MPa; inlet T = 0–37 °C; G = 400–1200 kg/(m²·s); heat flux ≤ 150 kW/m².	Constant heat flux on the inner rod; outer tube unheated. Nu based on the variable-property reference and piecewise B correction. Some large-temperature-difference cases were excluded from fitting; retain source regime limits.
Simoes et al. [139]	$Nu = 0.558Re_b^{0.8}Pr_b^{0.4}\left(\frac{\varrho_w}{\varrho_b}\right)^{0.224}\left(\frac{\overline{c_p}}{c_{p,b}}\right)^{0.362}\left(\frac{Gr_b}{Re_b^2}\right)^{0.07}$	Kenics static mixer used as a CO_2 heat exchanger. p = 8–21 MPa; T = 283–323 K; mass flow = 2–15 kg/h; bulk Re = 1000–20,000; bulk Pr = 2–7; fluid temperature rise = 10–35 K.	Static mixer geometry.
Bruch et al. [140]	$Nu = Nu_{FC} \cdot 15 \cdot \left(\frac{Gr_b}{Re_b^{2.7}}\right)^{0.4}$	Vertical copper tube, ID 6 mm; two 0.75 m counter-flow tube-in-tube sections joined by a U-bend; CO_2 cooled by water; upward and downward flow. Study coverage: p = 7.4–12 MPa; T = 15–70 °C; mass flow = 5–60 kg/h; G = 50–590 kg/(m²·s).	Listed equation is Fewster's relation reproduced, not Bruch's own fit. Bruch proposes separate aiding/opposing cooling models. Integral, subsection-averaged data reduction.
Liu et al. [141]	$Nu_w = 0.01Re_w^{0.9}P_w^{0.5}\left(\frac{\varrho_w}{\varrho_b}\right)^{0.906}\left(\frac{C_{p,w}}{C_{p,b}}\right)^{-0.585}$	Horizontal circular tubes; CO_2 cooling. Tested IDs = 4, 6 and 10.7 mm;	heating

Li et al. [142]	$Nu_{b,pdf} = 0.023Re_{b,pdf}^{0.8}Pr_{b,pdf}^{0.4}\left(\frac{\varrho_{w,pdf}}{\varrho_{b,pdf}}\right)^{0.3}\left(\frac{\overline{C_{P_{pdf}}}}{C_{P_{b,pdf}}}\right)^{n}$	PCHE with nine semicircular channels; CO_2 heating and cooling; experiments and CFD. Dh = 1.16 mm; L = 0.5 m; inlet p = 7.5–10 MPa; G = 326 and 762 kg/(m²·s); inlet T = 10–90 °C; experimental mean q″ = 30 kW/m²; additional numerical cases at 60 and 90 kW/m².	Heating and cooling; properties evaluated using the probability-density-function formulation. Experimental mean heat flux 30 kW/m²; numerical extensions at 60 and 90 kW/m².
Kim and Kim [143]	$Nu_b = 2.0514Re_b^{0.928}Pr_b^{0.742}\left(\frac{\varrho_w}{\varrho_b}\right)^{1.305}\left(\frac{\mu_w}{\mu_b}\right)^{-0.669}\left(\frac{C_{p,a}}{C_{p,b}}\right)^{0.888}(q^+)^{0.792}$	Vertical circular tube, ID 4.5 mm; heated length 0.90 m; upward and downward turbulent CO_2 heating. Upward data: p = 7.46–10.26 MPa; G = 208–874 kg/(m²·s); q″ = 38–234 kW/m². Downward data: p = 7.42–10.49 MPa; G = 233–879 kg/(m²·s); q″ = 52–231 kW/m². Reported bulk T = 29–115 °C.	Uniform direct electrical heating; correction includes heat-flux and property-ratio effects. It is calibrated for both flow directions; retain the definitions of q^+ and averaged heat capacity.
Yoon et al. [144]	$Nu = 3.7 + 0.0013Re_{min}^{1.12}P^{0.38}$ $Nu = 0.027Re_{min}^{0.78}Pr^{0.4}$ $f \cdot Re_{min} = 9.31 + 0.028Re_{min}^{0.86}$	Airfoil-fin PCHE; numerical study. Helium branch: 0 < Remin < 2500; Pr = 0.6–0.8. CO_2 branch: 3000 < Remin < 150,000; Pr = 0.6–0.8. Friction relation: 0 < Remin < 150,000.	Helium in the laminar regime and CO_2 in the turbulent regime; Remin uses the minimum flow cross-section.
Chu et al. [145]	$j = 0.026 \times \left(\frac{L_b}{L}\right)^{-0.170}\left(\frac{W}{L_a}\right)^{-0.248}Re_{in}^{-0.19\times(W/L_a)^{-0.187}}$ $f = 0.357 \times \left(\frac{L_b}{L}\right)^{-0.252}\left(\frac{W}{L_a}\right)^{-0.255}Re_{in}^{-0.173\times(W/L_4)^{-0.274}}$	PCHE with distributed airfoil fins; channel height 1 mm; full numerical domain contains 20 fins along the flow direction; staggered fin-pitch effects examined. 8000 < Rein < 100,000. Fin dimensions enter through Lb/L and W/La.	CO_2 only; geometry-specific j and friction fits; SST k–ω and REFPROP-derived property tables. Full flow-length simulation is used because local periodicity is unsuitable for strong property variation.
Pidaparti et al. [146]	$Nu = 0.0601Re^{0.7326}P_r^{0.3453}\left(\frac{\rho_b}{\rho_w}\right)^{0.4329}\left(\frac{c_{p,b}}{\bar{c}_p}\right)^{-0.3556}$ $f = 0.0256$	PCHE with discontinuous offset rectangular fins and NACA0020 airfoil fins; CO_2 experiments. Re = 2700–38,000; Pr = 0.8–25; 453 rectangular-fin and 306 airfoil-fin experiments.	Fin-specific correlations; rectangular and airfoil configurations treated separately.
Liu et al. [147]	$Nu = 0.0112Re^{0.9285}Pr^{0.6}\left(\frac{c_{pb}}{c_{pw}}\right)^{-0.1}\left(\frac{\varrho_b}{\varrho_w}\right)^{0.713}, 3000 < Re < 30000$	Straight-channel CO_2–water PCHE precooler; counter-flow semicircular passages, diameter 2 mm and length 295.20 mm; 100 channels on	CO_2 cooling; fit uses CFD data from a model checked against experiments. SST k–ω; equal

		each side. Experiments: p = 7.60–13.25 MPa; T = 310.67–359.68 K; mass flow = 26.53–171.43 kg/h; Re = 2702–15,774. CFD correlation: 3000 < Re < 30,000.	flow split among channels and periodic boundaries. Do not treat the extended CFD Re interval as wholly experimental coverage.
Saeed and Kim [148]	$Nu = 0.050Re^{0.8}Pr^{0.86}$ $f_h = 0.019Re^{-0.0054}, 3000 < Re < 60000, 0.7 < Pr < 1.2$ $f_c = 0.025Re^{0.038}$	PCHE with discontinuous staggered sinusoidal fins and rectangular flow passages; hot/cold Dh = 1.106/1.10 mm, defined at minimum flow area. Hot/cold longitudinal pitches = 9.0/7.24 mm; transverse pitches = 2.35/2.25 mm. Reduced CFD length 100 mm. Table 9, proposed geometry: 3000 ≤ Re ≤ 60,000; 0.7 ≤ Pr ≤ 1.2. Separate hot-side and cold-side friction fits.	Geometry-specific channel-averaged CFD fits; hydraulic diameter uses minimum flow area. SST k–ω with temperature-dependent properties; conjugate heat transfer and periodic channel boundaries. Header losses neglected. Listed coefficients describe the proposed sinusoidal geometry.
Jing et al. [149]	$Nu = 0.1991Re^{0.5952}Pr^{-0.7596}$ $f_h = 0.4294Re^{-0.4373} + 0.000672, 30000 < Re < 200000$ $f_c = 3.032Re^{-0.5341} + 0.000619$	Straight C0 PCHE configuration; counter-flow semicircular channels, diameter 2.4 mm and length 240 mm; CO_2 on both sides. Re = 30,000–200,000. Hot/cold inlet temperatures = 593/423 °C; outlet pressures = 8/13 MPa.	Listed Nu coefficients belong to the hot C0 channel; friction fits are side-specific. They do not describe the ribbed cases. RNG k–ε; periodic top/bottom and adiabatic side boundaries; conjugate heat transfer.
Shiralkar and Griffith [150]	$q_{enset} = 0.116G$	Vertical stainless-steel circular CO_2 test sections in the supporting 1968 MIT report; direct electrical heating. Plain-tube, twisted-tape and visualisation experiments are distinguished in the report. Supporting report: plain-tube IDs 0.245 in. (6.223 mm) and 1/8 in. (3.175 mm), each with a 60 in. (1.524 m) heated length. These are apparatus dimensions, not a confirmed validity envelope for the listed onset equation.	Supporting report is dated June 1968, whereas the appendix cites a 1969 publication. The q = 0.116 G equation has not been located and verified in the supplied report.

Kline et al. [151]	$q_{anset} = 2 \times 10^{-4} G^2 \cdot \left(0.7 + \frac{0.3}{1 + e^{4(D/8-2.35)}}\right)$	Vertical upward CO_2 in electrically heated tubes; IDs 4.6, 8 and 22 mm; corresponding heated lengths 1.20, 1.94 and 2.00 m. Study coverage: inlet p = 7.76 or 8.35 MPa; G = 200–1500 kg/(m²·s); inlet T = 0–40 °C. Diameter-corrected onset law: D = 4.6–22 mm, G = 300–1500 kg/(m²·s), p/pc = 1.13.	Minimum HTD-onset heat flux; exceedance alone does not imply HTD at every inlet temperature. Wall temperature profiles compared with normal heat transfer. At p/pc = 1.05, supporting 8 mm data cover G = 500–1500 kg/(m²·s).
Zhu et al. [152]	$q_{onset} = 5.126 \times 10^{-4} Gi_{pc}$	Heated circular tube; CO_2. ID = 10.0 mm; p = 7.5–21.1 MPa; G = 488–1600 kg/(m²·s); q″ = 74–413 kW/m².	HTD criterion uses the source-defined enthalpy scale ipc; critical q″/(Gipc) = 5.126 × 10⁻⁴.
Luo et al. [153]	$q_{enset} = 1.578 \times 10^{-\circ} G^2 (c_{ppc}/p_{pC})$	Upward flow in heated circular tubes; compiled water and CO_2 datasets. CO_2 database: D = 2–22 mm; p = 7.5–21 MPa; G = 100–2000 kg/(m²·s); q″ = 2.9–436 kW/m². Water database: D = 6–26 mm; p = 22–31 MPa; G = 201–2500 kg/(m²·s); q″ = 129–2328.6 kW/m².	HTD identified by a wall temperature peak before the pseudocritical point, Tb ≤ 0.995 Tpc. it uses ipc = cp,pc/βpc as an effective enthalpy scale. Its coefficient is dimensional; retain the source units.
Zhu et al. [154]	$q_{onset} = 1.75 \times 10^{-4} G^2 \cdot \left(6 + \frac{2}{1 + e^{12(D/14.5-1)}}\right)/7$	Vertical upward CO_2 in a uniformly heated 316 L circular tube; ID 14.5 mm, OD 16 mm, heated length 2.20 m; total test-section length 2.60 m. p = 7.73–8.53 MPa; G = 393.7–940 kg/(m²·s); q″ = 20.66–125.14 kW/m²; inlet T = 4.41–29.8 °C.	Minimum HTD-onset criterion; wall temperature-peak identification. Diameter correction compared with data for D = 4.6–22 mm; extension to tiny passages or untested diameters requires validation.
Li et al. [155]	$q_{onset} = 3.05 \times 10^{-4} Gi_{pc}$	CO_2 natural-circulation rectangular loop, 1.5 m high × 1.0 m wide; 316 L tube ID 4 mm; vertical heated Section 0.80 m; cooler length 0.54 m. p = 7.5–9.0 MPa; G = 78–210 kg/(m²·s); q″ = 5.5–31.8 kW/m²; inlet/outlet fluid T = 28–60 °C.	Natural circulation; uniform direct electrical heating. HTD threshold SBO = q″/(Gipc) = 3.05 × 10⁻⁴; criterion applies to this loop and tested conditions.
Mokry et al. [156]	$Nu_b = 0.0061 Re_b^{0.904} \overline{Pr}_b 0.084 \left(\frac{\rho_w}{\rho_b}\right)^{0.504}$	Vertical bare tube; upward supercritical-water heating.	Water; regression uses normal and improved heat transfer.

		ID = 10 mm; heated length = 4 m; p about 24 MPa; inlet T = 320–350 °C; G = 200–1500 kg/(m²·s); q″ ≤ 1250 kW/m².	
Liao and Zhao [157]	$Nu_b = 0.354Re_b^{0.8}Pr_b^{0.4}\left(\frac{Gr_m}{Re_b^{2.7}}\right)^{0.157}\left(\frac{\rho_w}{\rho_b}\right)^{1.297}\left(\frac{\bar{c_p}}{c_{p,b}}\right)^{0.296}$ for vertical upward flow $Nu_b = 0.643Re_b^{0.8}Pr_b^{0.4}\left(\frac{Gr_m}{Re_b^{2.7}}\right)^{0.186}\left(\frac{\rho_w}{\rho_b}\right)^{2.154}\left(\frac{\bar{c_p}}{c_p\,b}\right)^{0.751}$ for vertical downward flow $Nu = 0.124Re_b^{0.8}Pr_b^{0.4}\left(\frac{Gr}{Re_b^{2.7}}\right)^{0.203}\left(\frac{\rho_w}{\rho_b}\right)^{0.842}\left(\frac{\bar{p}}{\bar{p}_p b}\right)^{0.384}$ for horizontal flow	Circular stainless-steel miniature tubes; IDs 0.70, 1.40 and 2.16 mm; heated length 110 mm; horizontal, vertical upward and vertical downward CO_2 flow. p = 7.4–12 MPa; Tb = 20–110 °C; mass flow = 0.02–0.2 kg/min; Re = 10,000–200,000; Pr = 0.9–10; q″ = 10–200 kW/m²; Tw − Tb = 2–30 K.	Heating close to constant wall temperature; axially averaged Nu. Horizontal fit: $10^{-5} \le Gr/Re_b^2 \le 10^{-2}$; vertical fits: $2 \times 10^{-9} \le Grm/Reb^{2.7} \le 10^{-5}$. Orientation-specific fits.
Kim et al. [158]	Top: $C_1 = 2.56$; $C_2 = 9.89x10^2$ $Nu_{fc} = C_1R_b^{0.8}Pr_b^{0.4}\frac{Q_b^{1/3}}{R_b^{13/24}Pr_b^{1/3}}\left(\frac{\rho_{av}}{\rho_b}\right)^{1/3}\left(\frac{\mu_{av}}{\mu_b}\right)^{-2/3}\left(\frac{k_{av}}{k_b}\right)^{1}$ Bottom: $C_1 = 4.06E-4$; $C_2 = 2.08$; $\frac{1}{Nu_{nc}} = C_2Gr_q^{-1/4}P_b^{-3/20}\left(\frac{\rho_{av}}{\rho_b}\right)^{-1/2}\left(\frac{\mu_{av}}{\mu_b}\right)^{7/20}\left(\frac{c_{p,av}}{c_{p,b}}\right)^{-3/20}\left(\frac{k_{av}}{k_b}\right)^{-3/5}$	Horizontal circular tube, ID 7.75 mm; electrically heated length 0.91 m; upstream unheated entrance length 0.10 m; CO_2. Authors' experiments: inlet p = 7.383–7.735 MPa; inlet T = 24.50–30.07 °C; q″ = 1.2–25.9 kW/m²; G = 52.1–250.5 kg/(m²·s).	Horizontal heating; separate top/bottom semi-empirical mixed-convection models. Retain wall-specific constants and forced/natural-convection decomposition.
Krasnoshchekov and Protopopov [159]	$Nu_b = \frac{(ƒ/8)Re_bPr_b}{1.07 + 12.7\sqrt{ƒ/8}\left(Pr_b^{2/3}-1\right)}\left(\frac{\mu_b}{\mu_w}\right)^{0.11}\left(\frac{\lambda_b}{\lambda_w}\right)^{-0.33}\left(\frac{\tau_p}{c_{p,b}}\right)^{0.35}$	Forced convection in circular tubes; water and CO_2 at supercritical pressure. Ranges reproduced in Pioro et al. (2004), pp. 77–78. $2 \times 10^4 < Reb < 8.6 \times 10^5$; $0.85 < Prb < 65$; $0.90 < \mu b/\mu w < 3.60$; $1.00 < kb/kw < 6.00$; $0.07 < \bar{c}p/cp,b < 4.50$.	Turbulent forced-convection reference with viscosity, conductivity and mean-heat-capacity corrections; Nu_0 uses the friction-factor closure. Survey reports 85% of the compared data within ±15%. These pooled water/CO_2 bounds do not establish validity for enhanced passages or HTD prediction.
Krasnoshchekov [160]	$Nu_b = \frac{(ƒ/8)Re_bPr_b}{1.07 + 12.7\sqrt{ƒ/8}\left(Pr_b^{2/3}-1\right)}\left(\frac{\rho_w}{\rho_b}\right)^{0.3}\left(\frac{\bar{c}_p}{c_{p,b}}\right)^{n}$ $n = 0.4$ for $T_b < T_w < T_{pc}$ or $1.2T_{pc} < T_b < T_w$	Horizontal steel circular tube, ID 4.08 mm and OD 5.00 mm; heated length 51D (208 mm), preceded by an unheated entrance of 49D; turbulent CO_2 heating. p = 7.85 and 9.81 MPa; wall-to-fluid	Horizontal heating; the original source has two authors, Krasnoshchekov and Protopopov. Property-ratio correction with temperature-

	$n = \{0.4 + 0.2(T_w/T_{pc} - 1)$ for $T_b < T_{pc} < T_w$ $n = 0.4 + 0.2(T_w/T_{pc} - 1)[1 - 5(T_b/T_{pc} - 1)]$ for $T_{pc} < T_b < 1.2T_{pc}$	temperature difference up to 500 K; local heat flux up to 2.6 MW/m².	dependent heat-capacity exponent.
Jackson and Fewster [161]	$Nu_b = 0.0183 Re_b^{0.82} \overline{Pr}_b^{0.5} \left(\frac{\rho_w}{\rho_b}\right)^{0.3}$	Forced convection of supercritical-pressure fluids. p = 7.6 MPa; G = 50–460 kg/(m²·s); q″ = 30–330 kW/m².	Circular-tube forced-convection reference; mean-property Pr and wall-to-bulk density correction. Pioro et al. reproduce this form as Equation (15), without an entrance-length or explicit buoyancy correction.
Mokry et al. [162]	$Nu_b = 0.0121 Re_b^{0.86} \overline{Pr}_b^{0.23} \left(\frac{\rho_w}{\rho_b}\right)^{0.59}$	Vertical bare tube; upward CO_2 flow. D = 8 mm; p = 7.57–8.8 MPa; G = 706–3169 kg/(m²·s); q″ = 9–617 kW/m².	Heating.
Gupta et al. [136]	$Nu_b = 0.01 Re_b^{0.89} \overline{Pr}_b^{-0.14} \left(\frac{\rho_w}{\rho_b}\right)^{0.93} \left(\frac{\lambda_W}{\lambda_b}\right)^{0.22} \left(\frac{\mu_w}{\mu_b}\right)^{-1.13}$	Vertical Inconel-600 bare tube; upward CO_2 flow. ID = 8 mm; heated length = 2.208 m; outlet p = 7.4–8.8 MPa; G = 900–3000 kg/(m²·s); inlet T = 20–40 °C; q″ = 15–615 kW/m².	Heating.
Kim et al. [163]	$Nu_b = 0.0182 Re_b^{0.824} \overline{Pr}_b^{0.515} \left(\frac{\rho_w}{\rho_b}\right)^{0.299}$	Vertical circular tube; upward CO_2 flow. ID = 4.4 mm; G = 400–1200 kg/(m²·s); q″ up to 150 kW/m²; p = 7.75, 8.12 and 8.85 MPa.	Heating.
Bae and Kim [164]	$Nu_b = 0.021 Re_b^{0.82} Pr_b^{0.5} \left(\frac{\rho_w}{\rho_b}\right)^{0.3} \left(\frac{\bar{c}_p}{c_{p,b}}\right)^n f(Bu) Bu = \frac{\overline{Gr}_b}{R_b^{2.7} \overline{Pr}_b 0.5}$. $f(Bu) = \begin{cases} (1 + 10^8 Bu)^{-0.43465} \text{ when } 5 \times 10^{-8} < Bu < 7 \times 10^{-7} \\ 0.0185 Bu^{-0.43465} \text{ when } 7 \times 10^{-7} < Bu < 1 \times 10^{-6} \\ 0.75 \text{ when } 1 \times 10^{-6} < Bu < 1 \times 10^{-5} \\ 0.0119\, Bu^{-0.36} \text{ when } 1 \times 10^{-5} < Bu < 3 \times 10^{-5} \\ 32.4 Bu^{0.4} \text{ when } 3 \times 10^{-5} < Bu < 1 \times 10^{-4} \end{cases}$	Vertical upward CO_2 in circular tubes, IDs 4.4 and 9.0 mm, and an annulus formed by an 8 mm OD heater rod centred in a 10 mm ID tube. Inlet p = 7.75, 8.12 and 8.85 MPa; inlet T = 5–27 °C; G = 400, 500, 750, 1000 and 1200 kg/(m²·s); q″ ≤ 150 kW/m². Reported experimental Re = 1.67 × 10⁴–1.61 × 10⁵.	Upward heating in tubes and an annulus; direct electrical tube heating and indirect annular heating. Both normal and deteriorated regimes; 5 × 10^{-8} < Bu < 10^{-4}. Keep the source diameter and averaged-property definitions.
Liu et al. [165]	$Bu = \frac{Gr}{Re_b^{2.625} Pr_W^{0.4}} \left(\frac{\mu_w}{\mu_b}\right) \left(\frac{\rho_b}{\rho_w}\right)^{0.5}$, $Ac = \frac{4q}{Gc_{p,b}} \frac{\beta_b}{Re_b^{0.625}} \left(\frac{\mu_w}{\mu_b}\right) \left(\frac{\rho_b}{\rho_w}\right)^{0.5}$	Uniformly heated vertical circular tubes; new Nu correlation calibrated for upward CO_2 flow, IDs 6 and 10 mm. p = 7.4–10.6 MPa; G = 291.7–1506.5 kg/(m²·s);	Nu correlation is for upward heating; Bu/Ac definitions also assessed using downward-flow data. Definition-specific thresholds: Bu = 1.3 × 10^{-5}; Ac =

		q″ = 4.7–296.0 kW/m²; inlet T = 16.4–49 °C; D = 6 and 10 mm.	3.3 × 10⁻⁶. The fitted Nu model includes an entrance-length correction.
Bishop et al. [166]	$Nu_{b,Bishop} = 0.0069Re_b^{0.9}\overline{Pr}_b^{0.66}\left(\frac{\rho_w}{\rho_b}\right)^{0.43}\left(1+\frac{2.4}{L/D}\right)$	Upward supercritical-water heating in tubes; source experiments also included annuli. The listed relation was fitted to tube data. Survey-reported experimental coverage: p = 22.8–27.6 MPa; Tb = 282–527 °C; G = 651–3662 kg/(m²·s); q″ = 0.31–3.46 MW/m².	Water correlation; mean-property Pr and wall-to-bulk density correction. Survey reports ±15% fit to tube data. Entrance correction uses local axial position x/D, not automatically the total heated length L/D. Do not transfer the water envelope to CO_2 or annular passages.
Liao and Zhao [167]	$Nu_b = 0.124Re_b^{0.8}Pr_b^{0.4}\left(\frac{Gr_b}{Re_b^2}\right)^{0.203}\left(\frac{\rho_w}{\rho_b}\right)^{0.842}\left(\frac{\bar{c}_p}{C_{p,b}}\right)^{0.384}$ $Gr_b = \frac{(\rho_b-\rho_w)\rho_b g D_H^3}{\mu_b^2}$ $\bar{C}_p = \frac{h_w-h_b}{T_w-T_b}$	Horizontal stainless-steel circular mini/micro tubes; CO_2 cooling. IDs = 0.50, 0.70, 1.10, 1.40, 1.55 and 2.16 mm; p = 7.4–12 MPa; T = 20–110 °C; mass flow = 0.02–0.2 kg/min. Re up to 100,000.	Cooling at constant wall temperature; axially averaged Nu. Six diameters are confirmed by the supplied publisher abstract.
Kruizenga et al. [168]	$Nu_b = Nu_{Jack}\left(\frac{\bar{c}_{p,b}}{c_{p,-nc}}\right)^{-0.19}$ $Nu_b = 0.023Re_b^{0.8}Pr_b^{0.4}$	Nine horizontal parallel semicircular channels; turbulent CO_2 experiments and CFD. p = 7.5–10.1 MPa; Re up to 100,000; temperatures spanning Tpc.	Temperatures span the pseudocritical region; supplied abstract reports CFD predictions using near-wall y^+ about 1.
Filonenko [169]	$f = (1.82\log 10Re - 1.64)^{-2}$	Pipe flow. Re = 10^4–5×10^6.	
Petukhov et al. [170]	$f = (1.82\log 10Re - 1.64)^{-2}\left(\frac{\mu_m}{\mu_b}\right)^{0.24}$	Non-isothermal turbulent CO_2 pipe flow. D = 8 mm; p = 7.7 and 8.9 MPa; G = 1000–4100 kg/(m²·s); q″ = 384–1053 kW/m².	
Fang et al. [171]	$f = 0.0127\left[\ln\left(650\left(\frac{\varepsilon}{d_0}\right)^{0.67}+\left(\frac{99000}{Re}\right)^{1.32}+0.066Ch\right)\right]$ Ch = $\frac{P}{G\sqrt{i-i_0}}$	Adiabatic turbulent flow in round pipes; model fitted to water, CO_2 and RP-3 data. CO_2 subset: horizontal tube, ID 6 mm, length 7.50 m. CO_2 adiabatic subset: inlet T = 31–70 °C; inlet	Adiabatic model only; Ch = $p/[G\sqrt{(h-h_0)}]$, where h_0 is the saturated-liquid enthalpy at 0 °C. Include roughness and use consistent SI units. Non-

		p = 7.4–30 MPa; G = 88–165 kg/(m²·s); tube roughness ε = 0.15 mm. Full model database contains 820 adiabatic observations across three fluids.	isothermal data were assessed separately.
Zhang et al. [172]	$f = 2.15\mathrm{Re}^{-0.342}\mathrm{K}^{0.027}$	Vertical CO_2 tubes with IDs 8, 10 and 12 mm; friction ΔP correlated using Re and K. p = 7.5–23 MPa; G = 500–1500 kg/(m²·s); q″ = 15–400 kW/m²; Re = 5.9 × 10^4–7.5 × 10^5; K = 6.4 × 10^{-8}–2.7 × 10^{-6}.	Source-defined K relates thermal expansion to inertia; use its exact definition. f is based on frictional pressure loss, after the measured pressure drop is decomposed into contributions.
Nikitin et al. [67]	$\mathrm{h_{hot}} = 2.52\mathrm{Re}^{0.681}$ $f_{\mathrm{hot}} = 0.04495 - 1.402 \times 10^{-6}\mathrm{Re}$	Zigzag PCHE with CO_2 on both sides; hot side: 144 channels, diameter 1.9 mm, active length 1.0 m; cold side: 66 channels, diameter 1.8 mm, active length 1.1 m. Hot inlet: p = 2.2–3.2 MPa, T = 280–300 °C. Cold inlet: p = 6.5–10.5 MPa, T = 90–108 °C. Equal mass flow on both sides: 40–80 kg/h. Listed hot-side fits: 2800 ≤ Re ≤ 5800.	Listed h is dimensional, in W/(m²·K); it is not Nu. Hot-side pressure is below the critical pressure. h reconstructed using CFD and overall measurements; fit assumes a constant local heat flux and includes a heat-loss correction.
Ngo et al. [173]	$\mathrm{Nu} = 0.1696\mathrm{Re}^{0.629}\mathrm{Pr}^{0.317}$ $f = 0.1924\mathrm{Re}^{-0.091}$	Zigzag-fin CO_2 microchannel exchanger; angle 52°, Dh = 1.09 mm; 96 hot-side and 44 cold-side channels. Longitudinal/transverse pitches = 7.565/3.426 mm; fin width/depth/gap = 0.80/0.94/1.31 mm. Separate S-shaped exchanger also tested. Listed zigzag Nu and combined-side pressure-drop-factor fits: 3500 < Re < 22,000; Nu fit additionally requires 0.75 < Pr < 2.2.	Listed equations are zigzag fits; $f = 0.1924\mathrm{Re}^{-0.091}$ combines both sides. Separate hot/cold fits and separate S-shaped-fin correlations must not be substituted without their own ranges.
Cheng et al. [174]	$\mathrm{Nu} = 0.0188\mathrm{Re}^{0.8742}$ $f = 0.2881\mathrm{Re}^{-0.1322}$	Experimental CO_2–water zigzag PCHE precooler; hot/cold channel diameters 1.5/1.6 mm, pitch angles 115°/150°, and longitudinal pitches 9.0/24.6 mm; plate size 486 × 101 × 2 mm. CO_2 inlet p = 8.07–8.60 MPa; inlet T = 363.4–	CO_2 cooling with laminar water-side flow; reported numbers describe the experiment. The listed Nu/f coefficients duplicate Kim's 40° relation and are not established

		383.4 K; inlet Re = 31,157–52,806. Water inlet p = 0.163–0.204 MPa; inlet T = 293.0–299.7 K; inlet Re = 1084–1947.	here as a new Cheng regression.
Baik et al. [175]	$Nu = 0.8405Re^{0.5704}Pr^{1.08}$ $f = 0.0748Re^{-0.19}$	CO_2–water PCHE precooler near the critical point; experiments and CFD. Experimental coverage: T = 26–43 °C; p = 7.3–8.6 MPa; Re = 15,000–100,000; Pr = 2–33.	Reported test states span subcritical and supercritical conditions.
Saeed et al. [176]	$Nu = 0.475Re^{0.61}P^{0.17}$ $f = 0.13Re^{-0.044}$	CO_2–water PCHE precooler; zigzag channels with 40° fin angle and hydraulic diameter 1.106 mm; 72 periodic units; longitudinal/transverse pitches 9.0/2.35 mm. Table 6, CO_2 correlations: 3000 ≤ Re ≤ 60,000; 2.0 ≤ Pr ≤ 13.	CO_2 cooling; SST k–ω and REFPROP; local segment averages used near Tpc. The Nu expression uses $Pr^{0.17}$, not pressure $P^{0.17}$. Use Table 6 limits; the conclusion reports conflicting limits.
Meshram et al. [177]	$Nu = 87.56(P_L/12)^{-0.178}[(180 - 2\theta)/116]^{-0.9306}$ $f = 0.0375\left(\frac{P_L}{12}\right)^{-0.9639}[(180 - 2\theta)/116]^{-2.409}$ Hot fluid $Nu = 85.95(P_L/12)^{-0.171}[(180 - 2\theta)/116]^{-0.8912}$ $f = 0.0395(P_L/12)^{-0.9479}[(180 - 2\theta)/116]^{-2.239}$ Cold fluid	Straight and zigzag PCHE regenerator channels; fully turbulent CO_2 CFD. Hot fluid: Tb = 470–630 K; cold fluid: Tb = 400–520 K; Re = 5000–32,000 for both sides.	Separate hot-side and cold-side correlations; pitch and bend-angle dependence.

References

1. Pioro, I.L. Current status of research on heat transfer in forced convection of fluids at supercritical pressures. *Nucl. Eng. Des.* **2019**, *354*, 110207. https://doi.org/10.1016/j.nucengdes.2019.110207.
2. Luo, S.; Xu, D.; Song, J.; Liu, J. A review of regenerative cooling technologies for scramjets. *Appl. Therm. Eng.* **2021**, *190*, 116754. https://doi.org/10.1016/j.applthermaleng.2021.116754.
3. Ismail, M.F.; Al-Mahasne, M.M.; Borowski, G.; Alsaqoor, S.; Alenezi, A.; Al-Odienat, A. Optimized low-speed wind energy harvesters: Enhancing piezoelectric and triboelectric performance for urban applications. *J. Ecol. Eng.* **2025**, *26*, 325–340. https://doi.org/10.12911/22998993/205241.
4. Zhang, Z.; Wu, Y.; Jalili, M.; Yang, L.; Wei, S. Pathways to sustainable urban energy systems: Trade-off and synergy between green transition and resilience. *Sustain. Cities Soc.* **2026**, *151*, 107967. https://doi.org/10.1016/j.scs.2026.107967.
5. Jalili, M.; Zhang, Z.; Wei, S.; Yang, L.; Wu, Y. Comparative Policy Pathways for Energy Transition and Carbon Emissions Reduction to 2050: Evidence from Germany, China, and Saudi Arabia. *Pollution* **2026**. *12*, 586–600.
6. Gao, C.; Zou, J.; Ma, Y.; Li, W.; Chen, B.; Hou, Y. Influence of PCHE size and types on thermodynamic and economic performance of supercritical carbon dioxide Brayton cycle for small modular reactors and its optimization. *Ann. Nucl. Energy* **2024**, *207*, 110721. https://doi.org/10.1016/j.anucene.2024.110721.
7. Ma, Y.-N.; Hu, P. Multi-objective optimization design and strength analysis of printed circuit heat exchangers for supercritical CO_2 Brayton cycle. *Appl. Therm. Eng.* **2024**, *250*, 123555. https://doi.org/10.1016/j.applthermaleng.2024.123555.
8. Manda, U.; Peles, Y. Performance evaluation criteria of a star-shaped cross-sectional horizontal microchannel with supercritical carbon dioxide. *Int. Commun. Heat Mass Transf.* **2024**, *157*, 107803. https://doi.org/10.1016/j.icheatmasstransfer.2024.107803.
9. Ghodrati, P.; Khoshvaght-Aliabadi, M. Supercritical CO_2 flow and heat transfer through tapered horizontal mini-tubes: Parametric analysis and optimization study. *Appl. Therm. Eng.* **2024**, *242*, 122512. https://doi.org/10.1016/j.applthermaleng.2024.122512.
10. Manna, R.; Al-Aboushi, A.; Abu Shaban, N.; Nasser, I. Numerical Analysis of Heat Transfer Deterioration of Hydrogen Flowing in a Circular Pipe under Transcritical Boundary Conditions. *Int. J. Heat Technol.* **2024**, *42*, 721–730. https://doi.org/10.18280/ijht.420301.
11. Nasser, I.; Martinez-Sanchis, D.; Haidn, O.; Manfletti, C. Impacts of hydrocarbons impurities on heat transfer deterioration. *Appl. Therm. Eng.* **2024**, *246*, 122894. https://doi.org/10.1016/j.applthermaleng.2024.122894.
12. Mourad, M.H.; El-Sayed, M.A.; Elnabawy, E.; Obaid, A.; Shyha, I. Optimisation of Density and Surface Roughness in Selective Laser Melting of Ti6Al4V, In Proceedings of the 19th CIRP Conference on Intelligent Computation in Manufacturing Engineering, Ischia, Italy, 16–18 July 2025.
13. Elnabawy, E.; Lei, I.F.; Mourad, M.H.; El-Sayed, M.A.; Obaid, A.; Shyha, I. Piezoelectric EBS Nanofibrous Membranes for Low-Power Sensors Applications, In Proceedings of the 19th CIRP Conference on Intelligent Computation in Manufacturing Engineering, Ischia, Italy, 16–18 July 2025.
14. Hamadneh, T.; Falahah, I.A.; Batiha, B.; Alenezi, A.; Ali, M. Optimal hydrothermal scheduling for economic operation of power systems using an improved teaching-learning-based optimization algorithm. *Electr. Eng. Electromechanics* **2026**, 76–84, 121373. https://doi.org/10.20998/2074-272x.2026.5.10.
15. Cheng, L.; Xu, J. Experimental investigation of non-uniform heating effect on flow and heat transfer of supercritical carbon dioxide: An application to solar parabolic trough collector. *Renew. Energy* **2024**, *236*, 121373. https://doi.org/10.1016/j.renene.2024.121373.
16. Zhang, H.; Guo, J.; Cui, X.; Huai, X. Performance analysis of supercritical pressure CO_2 in several enhanced tubes with non-uniform heat flux. *Appl. Therm. Eng.* **2020**, *180*, 115823. https://doi.org/10.1016/j.applthermaleng.2020.115823.
17. Jajja, S.A.; Sequeira, J.M.; Fronk, B.M. Geometry and orientation effects in non-uniformly heated microchannel heat exchangers using supercritical carbon dioxide. *Exp. Therm. Fluid Sci.* **2020**, *112*, 109979. https://doi.org/10.1016/j.expthermflusci.2019.109979.
18. Xu, X.; Teng, L.; Ran, W.; Wang, Y.; Liu, C. A review of heat transfer deterioration mechanisms and mitigation strategies of supercritical CO_2 heat transfer. *Int. J. Heat Fluid Flow* **2024**, *109*, 109534. https://doi.org/10.1016/j.ijheatfluidflow.2024.109534.
19. Wang, Z.; Liu, X.; Chen, J.; Ye, J.; He, J.; Jia, L.; Chen, Y.; Luo, X. An overview of flow instability at supercritical pressure. *Int. J. Heat Mass Transf.* **2024**, *227*, 125533. https://doi.org/10.1016/j.ijheatmasstransfer.2024.125533.
20. Li, Z.; Banuti, D.T.; Ren, J.; Lyu, J.; Wang, H.; Chu, X. A review of microscale physics and macroscale convective heat transfer in supercritical fluids for energy and propulsion systems. *Appl. Therm. Eng.* **2025**, *272*, 126380. https://doi.org/10.1016/j.applthermaleng.2025.126380.

21. Chen, J.; Du, W.; Cheng, K.; Li, X.; Huai, X.; Guo, J.; Lv, P.; Dong, H. Advances in thermal–hydraulic performance and dynamic behavior of supercritical CO_2 in printed circuit heat exchangers: mechanisms, innovations, and future perspectives. *Int. J. Heat Fluid Flow* **2025**, *116*, 109953. https://doi.org/10.1016/j.ijheatfluidflow.2025.109953.
22. Ma, W.; Hu, Z.; Zhang, H.; El-Mesery, H.S.; Workneh, T.S.; Wang, Z. A review of thermal-hydraulic performance in airfoil fin printed circuit heat exchangers. *Renew. Sustain. Energy Rev.* **2025**, *226*, 116349. https://doi.org/10.1016/j.rser.2025.116349.
23. Chai, L.; Tassou, S.A. A review of printed circuit heat exchangers for helium and supercritical CO_2 Brayton cycles. *Therm. Sci. Eng. Prog.* **2020**, *18*, 100543. https://doi.org/10.1016/j.tsep.2020.100543.
24. Kandlikar, S.G.; Grande, W.J. Evolution of Microchannel Flow Passages–Thermohydraulic Performance and Fabrication Technology. *Heat Transf. Eng.* **2003**, *24*, 3–17. https://doi.org/10.1080/01457630304040.
25. Wang, X.; Xiang, M.; Huo, H.; Liu, Q. Numerical study on nonuniform heat transfer of supercritical pressure carbon dioxide during cooling in horizontal circular tube. *Appl. Therm. Eng.* **2018**, *141*, 775–787. https://doi.org/10.1016/j.applthermaleng.2018.06.019.
26. Pu, H.; Li, N.; Dong, M.; Shang, Y.; Du, H.; Hou, C.; Zhang, J. Numerical investigation on turbulent mixed convective heat transfer of CO_2 in a horizontal miniature tube at supercritical pressure. *Int. J. Therm. Sci.* **2023**, *184*, 107992. https://doi.org/10.1016/j.ijthermalsci.2022.107992.
27. Kim, T.H.; Kwon, J.G.; Kim, M.H.; Park, H.S. Experimental investigation on validity of buoyancy parameters to heat transfer of CO_2 at supercritical pressures in a horizontal tube. *Exp. Therm. Fluid Sci.* **2018**, *92*, 222–230. https://doi.org/10.1016/j.expthermflusci.2017.11.024.
28. Wahl, A.; Mertz, R.; Laurien, E.; Starflinger, J. Heat transfer correlation for sCO_2 cooling in a 2 mm tube. *J. Supercrit. Fluids* **2021**, *173*, 105221. https://doi.org/10.1016/j.supflu.2021.105221.
29. Guo, P.; Liu, S.; Yan, J.; Wang, J.; Zhang, Q. Experimental study on heat transfer of supercritical CO2 flowing in a mini tube under heating conditions. *Int. J. Heat Mass Transf.* **2020**, *153*, 119623. https://doi.org/10.1016/j.ijheatmasstransfer.2020.119623.
30. Kim, D.E.; Kim, M.H. Experimental study of the effects of flow acceleration and buoyancy on heat transfer in a supercritical fluid flow in a circular tube. *Nucl. Eng. Des.* **2010**, *240*, 3336–3349. https://doi.org/10.1016/j.nucengdes.2010.07.002.
31. Chen, L.; Zhu, M.; Qing, H.; Zhou, L.; Wang, C.; Zhou, J.; Xu, K.; Xu, J.; Jiang, L.; Su, S.; et al. Mechanism analysis of convective heat transfer of supercritical CO_2 in heated vertical-flow tube. *J. Supercrit. Fluids* **2025**, *222*, 106586. https://doi.org/10.1016/j.supflu.2025.106586.
32. Theologou, K.; Mertz, R.; Starflinger, J. Experimental investigation of the pressure drop of CO_2 flow at supercritical pressures in a heated 4 mm smooth pipe with different orientations. *J. Supercrit. Fluids* **2025**, *215*, 106407. https://doi.org/10.1016/j.supflu.2024.106407.
33. Wang, X.; Yang, L.; Xu, B.; Chen, Z. Experimental study on heat transfer and flow characteristics of supercritical CO_2: In-depth analysis of three heat transfer coefficients. *Int. J. Heat Mass Transf.* **2025**, *241*, 126748. https://doi.org/10.1016/j.ijheatmasstransfer.2025.126748.
34. Wu, Y.; Liu, P.; Huang, L.; Ge, Y.; Chen, L. Heat transfer performance of supercritical CO_2 in a vertical U-tube. *Appl. Therm. Eng.* **2024**, *250*, 123505. https://doi.org/10.1016/j.applthermaleng.2024.123505.
35. So, H.S.; Bae, Y.H.; Shin, J.-H.; Chang, H.-M. A numerical investigation of the thermal characteristics of supercritical carbon dioxide (sCO_2) flowing through mini serpentine channels. *Appl. Therm. Eng.* **2024**, *246*, 123023. https://doi.org/10.1016/j.applthermaleng.2024.123023.
36. Wang, K.; Zhang, X.; Zhang, Z.-P.; Zhang, Z.-D.; Fan, Y.-H.; Min, C.-H.; Rao, Z.-H. Flow and heat transfer characteristics of supercritical CO_2 in serpentine tubes under semi-circumferential heating conditions. *Int. J. Heat Mass Transf.* **2025**, *236*, 126304. https://doi.org/10.1016/j.ijheatmasstransfer.2024.126304.
37. Khoshvaght-Aliabadi, M.; Ghodrati, P.; Salami, M.; Kang, Y. Turbulent supercritical CO_2 flow and cooling heat transfer in vertical alternating flattened tubes. *Int. Commun. Heat Mass Transf.* **2025**, *162*, 108565. https://doi.org/10.1016/j.icheatmasstransfer.2024.108565.
38. Yu, B.; Wang, Y.; Liu, Q.; Shi, W.; Xu, J. Effects of turbulent Prandtl number on supercritical carbon dioxide turbulent flow with high heat flux in vertical round tube. *Appl. Therm. Eng.* **2024**, *249*, 123310. https://doi.org/10.1016/j.applthermaleng.2024.123310.
39. Zhang, H.; Guo, J.; Cui, X.; Huai, X. Heat transfer performance of supercritical pressure CO_2 in a non-uniformly heated horizontal tube. *Int. J. Heat Mass Transf.* **2020**, *155*, 119748. https://doi.org/10.1016/j.ijheatmasstransfer.2020.119748.
40. Yang, W.; Zhang, H.; Yang, J.; Qu, J. Numerical study on fluid flow and heat transfer characteristics of supercritical CO_2 in horizontal tube under various non-uniform heating conditions. *Int. J. Heat Mass Transf.* **2025**, *236*, 126399.

https://doi.org/10.1016/j.ijheatmasstransfer.2024.126399. Corrigendum in *Int. J. Heat Mass Transf.* **2025**, *241*, 126685. https://doi.org/10.1016/j.ijheatmasstransfer.2025.126685.

41. Whitaker, T.A.; Cochran, J.W.; Hochhalter, J.D.; Rao, S.R. Flow regimes and heat transfer mechanisms affecting supercritical transition in microchannels. *Int. J. Heat Mass Transf.* **2024**, *218*, 124749. https://doi.org/10.1016/j.ijheatmasstransfer.2023.124749.
42. Whitaker, T.A.; Rao, S.R. On the continuous nature of phase change in near-critical carbon dioxide. *Int. J. Heat Mass Transf.* **2024**, *225*, 125383.
43. Chen, L.; Zeng, G.; Yang, D.; Yuan, H.; Zang, J.; Huang, Y. Quantitative visualization on boundary heat transfer of supercritical CO_2 mini-channel through-flow (Re=104) via pixelated phase-shifting interferometry. *Int. J. Heat Mass Transf.* **2024**, *223*, 125258. https://doi.org/10.1016/j.ijheatmasstransfer.2024.125258.
44. Bayrak, E.; Ahn, H. Numerical study on mechanisms underlying the heat transfer enhancement of upward supercritical CO_2 flow at low Reynolds numbers near the pseudo-critical region through a microtube. *Int. Commun. Heat Mass Transf.* **2025**, *165*, 108995. https://doi.org/10.1016/j.icheatmasstransfer.2025.108995.
45. Jajja, S.A.; Fronk, B.M. Investigation of near-critical heat transfer in rectangular microchannels with single wall heating using infrared thermography. *Int. J. Heat Mass Transf.* **2021**, *177*, 121470. https://doi.org/10.1016/j.ijheatmasstransfer.2021.121470.
46. Khoshvaght-Aliabadi, M.; Ghodrati, P.; Mahian, O.; Kang, Y.T. Enhancing the performance of supercritical CO_2-cooled heat sink by converging–diverging minichannels. *Appl. Therm. Eng.* **2023**, *234*, 121225. https://doi.org/10.1016/j.applthermaleng.2023.121225.
47. Huang, H.; Zhai, Y.; Li, Z.; Wang, H. Thermo-hydraulic characteristics and structural optimization of supercritical CO_2-cooled microchannel heat sink. *Int. Commun. Heat Mass Transf.* **2024**, *154*, 107438. https://doi.org/10.1016/j.icheatmasstransfer.2024.107438.
48. Kumar, N.; Basu, D.N. Thermalhydraulic assessment and design optimization of incorporating flow obstructors in a supercritical minichannel heat sink. *Appl. Energy* **2023**, *349*, 121666. https://doi.org/10.1016/j.apenergy.2023.121666.
49. Khoshvaght-Aliabadi, M.; Ghodrati, P.; Mortazavi, H.; Kang, Y.T. Numerical analysis of heat transfer and flow characteristics of supercritical CO_2-cooled wavy mini-channel heat sinks. *Appl. Therm. Eng.* **2023**, *226*, 120307. https://doi.org/10.1016/j.applthermaleng.2023.120307.
50. Majmader, F.B.; Hasan, M.J. Heat Transfer and Fluid Flow Characteristics of a Periodically Constricted Microchannel Heat Sink with Supercritical Carbon-Di-Oxide (sCO_2) as a Coolant near Its Critical Point. Int. J. Therm. Sci. 2025, 210, 109609. https://doi.org/10.1016/j.ijthermalsci.2024.109609.
51. Jajja, S.A.; Zada, K.R.; Fronk, B.M. Experimental investigation of supercritical carbon dioxide in horizontal microchannels with non-uniform heat flux boundary conditions. *Int. J. Heat Mass Transf.* **2019**, *130*, 304–319. https://doi.org/10.1016/j.ijheatmasstransfer.2018.10.027.
52. Nabil, M.; Rattner, A.S. Large eddy simulations of high-heat-flux supercritical CO_2 convection in microchannels: Mixed convection and non-uniform heating. *Int. J. Heat Mass Transf.* **2019**, *145*, 118710. https://doi.org/10.1016/j.ijheatmasstransfer.2019.118710.
53. Zhang, Z.-D.; Wang, K.; Liu, Y.-J.; Zhang, X.; Fan, Y.-H.; Min, C.-H. Study on the convective heat transfer characteristics of supercritical CO_2 in mini-channels under unilateral heating conditions for application in a compact solar receiver. *Int. J. Heat Mass Transf.* **2024**, *219*, 124839. https://doi.org/10.1016/j.ijheatmasstransfer.2023.124839.
54. Awais, A.A.; Saeed, M.; Kim, M.-H. Performance enhancement in minichannel heat sinks using supercritical carbon dioxide (sCO_2) as a coolant. *Int. J. Heat Mass Transf.* **2021**, *177*, 121539. https://doi.org/10.1016/j.ijheatmasstransfer.2021.121539.
55. Yuan, D.; Lu, Z.; Zhou, N.; Zhang, Q.; Qin, B. Experimental study of CO_2 heat transfer at supercritical pressure in combined passages of parallel rectangular channels and porous media channels under supersonic mainstreams. *Appl. Therm. Eng.* **2024**, *256*, 124135. https://doi.org/10.1016/j.applthermaleng.2024.124135.
56. Hu, Z.-C. and K. Wang, Effect of channel size on the performance of a PCHE-based supercritical CO_2 thermoacoustic engine. *Appl. Therm. Eng.* **2024**, *236*, 121457**.**
57. Park, J.H.; Kim, M.H. Modeling of local heat transfer on supercritical pressure CO_2 in horizontal semicircular tube. *Int. J. Heat Mass Transf.* **2022**, *184*, 122197. https://doi.org/10.1016/j.ijheatmasstransfer.2021.122197.
58. Li, X.-L.; Li, Y.-F.; Zhang, Z.-D.; Fan, Y.-H.; Wang, J.-Y.; Wang, K.; Min, C.-H. Optimization of a wavy-channel compact solar receiver with supercritical carbon dioxide. *Appl. Therm. Eng.* **2024**, *241*, 122373. https://doi.org/10.1016/j.applthermaleng.2024.122373.

59. Liu, S.-H.; Liu, R.-L.; Huang, Y.-P.; Zhu, X.-L.; Yang, L.; Tang, J.; Han, B.; Xing, T.-Y.; Zhao, X.-B. Experimental study on flow and heat transfer of supercritical carbon dioxide in zigzag channels with bending angle 30° for advanced nuclear systems. *Ann. Nucl. Energy* **2023**, *185*, 109720. https://doi.org/10.1016/j.anucene.2023.109720.
60. Tu, Y.; Zeng, Y. Flow and heat transfer characteristics study of supercritical CO_2 in horizontal semicircular channel for cooling process. *Case Stud. Therm. Eng.* **2020**, *21*, 100691. https://doi.org/10.1016/j.csite.2020.100691.
61. Zhang, X.; Guo, W.; Gao, G.; Xi, W.; Liu, J.; Sunden, B. Numerical investigations of flow and heat transfer characteristics of a regenerative cooling channel using supercritical CO_2 with different cross-section shapes. *Int. J. Therm. Sci.* **2025**, *215*, 109965. https://doi.org/10.1016/j.ijthermalsci.2025.109965.
62. Manda, U.; Mazumdar, S.; Peles, Y. Effects of cross-sectional shape on flow and heat transfer of the laminar flow of supercritical carbon dioxide inside horizontal microchannels. *Int. J. Therm. Sci.* **2024**, *201*, 108992. https://doi.org/10.1016/j.ijthermalsci.2024.108992.
63. Li, Z.; Lu, D.; Lin, M.; Cao, Q. Investigation of the thermal-hydraulic characteristics of SCO_2 in a modified hybrid airfoil channel. *Energy* **2023**, *308*, 132838. https://doi.org/10.1016/j.energy.2024.132838.
64. Li, Z.; Lu, D.; Wang, X.; Cao, Q. Analysis on the flow and heat transfer performance of SCO_2 in airfoil channels with different structural parameters. *Int. J. Heat Mass Transf.* **2024**, *219*, 124846. https://doi.org/10.1016/j.ijheatmasstransfer.2023.124846.
65. Khoshvaght-Aliabadi, M.; Ghodrati, P.; Kang, Y.T. Optimal combination of converging and diverging minichannels in PCHE as precooler under diverse operating conditions of supercritical CO_2. *Energy* **2023**, *272*, 127158. https://doi.org/10.1016/j.energy.2023.127158.
66. Zilio, G.; Moura, M.; dos Santos, F.; Possamai, T.; Mortean, M. Nusselt number analysis of printed circuit heat exchangers with straight and zigzag channels. *Int. J. Heat Fluid Flow* **2024**, *107*, 109395. https://doi.org/10.1016/j.ijheatfluidflow.2024.109395.
67. Nikitin, K.; Kato, Y.; Ngo, L. Printed circuit heat exchanger thermal–hydraulic performance in supercritical CO_2 experimental loop. *Int. J. Refrig.* **2006**, *29*, 807–814. https://doi.org/10.1016/j.ijrefrig.2005.11.005.
68. Ahmed, M.; Ehsan, M.M. Design and Off-design Performance Analysis of a Zigzag Channeled Precooler for Indirect Cooling System of Supercritical CO_2 Recompression Cycle Incorporated with a Flow-Bypass System. *Appl. Therm. Eng.* **2023**, *226*, 120321. https://doi.org/10.1016/j.applthermaleng.2023.120321.
69. Jin, F.; Chen, D.; Hu, L.; Huang, Y.; Bu, S. Numerical study on flow distribution of supercritical CO_2 in multiple channels of printed circuit heat exchanger. *Appl. Therm. Eng.* **2023**, *234*, 121185. https://doi.org/10.1016/j.applthermaleng.2023.121185.
70. Li, L.; Liu, F. Research on topology optimization of supercritical CO_2 PCHE under different physical property parameters. *Int. J. Heat Fluid Flow* **2025**, *116*, 109965. https://doi.org/10.1016/j.ijheatfluidflow.2025.109965.
71. Wang, D.; Zhou, R.; Li, M.; Zhang, K.; Wang, Z.; Li, K.; Chu, H. Study on the influence of tube type and fluid flow channel on cooling heat transfer characteristics of supercritical CO_2 in spirally grooved casing tubes. *Int. J. Heat Fluid Flow* **2025**, *114*, 109804. https://doi.org/10.1016/j.ijheatfluidflow.2025.109804.
72. Liu, J.; Xu, M.; Guo, W.; Xi, W.; Liu, C.; Sunden, B. Flow and heat transfer mechanism of a regenerative cooling channel mounted with pin-fins using supercritical CO_2 as coolant. *Int. J. Therm. Sci.* **2025**, *208*, 109425. https://doi.org/10.1016/j.ijthermalsci.2024.109425.
73. Kumar, N.; Ghosh, S.; Basu, D.N. Thermalhydraulic assessment and performance prediction of supercritical minichannel heat sink with airfoil-shaped obstructions using GA-tuned neural network. *Appl. Therm. Eng.* **2023**, *227*, 120352. https://doi.org/10.1016/j.applthermaleng.2023.120352.
74. Zeng, G.; Chen, L.; Yuan, H.; Huang, Y. Visualization of transient boundary heat transfer of supercritical CO_2 through-flow in mini-channel under top heating. *Int. J. Heat Fluid Flow* **2025**, *116*, 109994. https://doi.org/10.1016/j.ijheatfluidflow.2025.109994.
75. Li, W.; Yu, Z.; Wang, Y.; Li, Y. Heat transfer enhancement of twisted tape inserts in supercritical carbon dioxide flow conditions based on CFD and vortex kinematics. *Therm. Sci. Eng. Prog.* **2022**, *31*, 101285. https://doi.org/10.1016/j.tsep.2022.101285.
76. Li, X.; Li, Z.; Zhai, Y.; Wang, H. Numerical study on the enhancement of local and average heat transfer in supercritical CO_2 horizontal flow by twisted tape inserts. *Int. Commun. Heat Mass Transf.* **2025**, *163*, 108699. https://doi.org/10.1016/j.icheatmasstransfer.2025.108699.
77. Wang, J.; Xiang, P.; Xu, B.; Zhang, Y.; Chen, Z.; Xu, J.; Lei, Y. Vortex-driven heat transfer enhancement in supercritical CO_2: Structural optimization with claw-shaped lattice design for enhanced thermal performance. *Int. Commun. Heat Mass Transf.* **2025**, *167*, 109275. https://doi.org/10.1016/j.icheatmasstransfer.2025.109275.
78. Xiang, P.; Wang, J.; Wang, Y.; Chen, Z.; Kang, Y.; Lei, Y. Mitigation effects of lattice structure arrays on heat transfer deterioration of supercritical CO_2. *Appl. Therm. Eng.* **2024**, *257*, 124171. https://doi.org/10.1016/j.applthermaleng.2024.124171.

79. Liu, J.; Guo, W.; Yin, M.; Xi, W.; Sunden, B. Flow and heat transfer characteristic of regenerative cooling channels using supercritical CO_2 with circular tetrahedral lattice structures. *Case Stud. Therm. Eng.* **2025**, *71*, 106204. https://doi.org/10.1016/j.csite.2025.106204.
80. Xu, M.; Liu, J.; Xi, W.; Liu, C.; Sunden, B. Thermodynamic performance and flow structures analysis of supercritical CO_2 applied in a regenerative cooling channel mounted with mini-ribs. *Case Stud. Therm. Eng.* **2024**, *60*, 104704. https://doi.org/10.1016/j.csite.2024.104704.
81. Zhao, H.; Guo, X.; Guo, W.; Yang, Y.; Lei, X. Experimental study on flow and heat transfer characteristics of supercritical carbon dioxide in 3D printed channels. *Int. J. Heat Fluid Flow* **2026**, *117*, 110014. https://doi.org/10.1016/j.ijheatfluidflow.2025.110014.
82. Liao, Y.; Guo, Z.; Gao, C.; Lu, Y.; Lyu, H.; Zhu, H.; Wu, H.; Guo, W.; Zhao, H.; Wang, S.; et al. The study of corrosion characteristics of lead–bismuth eutectic supercritical carbon dioxide microchannel heat exchanger. *Nucl. Eng. Des.* **2024**, *425*, 113304. https://doi.org/10.1016/j.nucengdes.2024.113304.
83. Fazio, C.; Sobolev, V.; Aerts, A.; Gavrilov, S.; Lambrinou, K.; Schuurmans, P.; Gessi, A.; Agostini, P.; Ciampichetti, A.; Martinelli, L.; et al. *Handbook on Lead-Bismuth Eutectic Alloy and Lead Properties, Materials Compatibility, Thermal-Hydraulics and Technologies—2015 Edition*; Organisation for Economic Co-Operation and Development, Nuclear Energy: Issy-les-Moulineaux, France, 2015.
84. Wen, Z.-X.; Wu, J.-L.; Wang, S.-S.; Cheng, J.-Q.; Li, Q. Numerical study and machine learning on local flow and heat transfer characteristics of supercritical carbon dioxide mixtures in a sinusoidal wavy channel PCHE. *Int. J. Heat Mass Transf.* **2024**, *223*, 125278. https://doi.org/10.1016/j.ijheatmasstransfer.2024.125278.
85. Fu, X.; Cai, S.; Qiu, G.; Sun, J.; Zhao, B.; Li, Q.; Cai, W. Optimization study on PCHE channels for lead–bismuth eutectic and supercritical carbon dioxide coupled flow and heat transfer. *Nucl. Eng. Des.* **2025**, *435*, 113942. https://doi.org/10.1016/j.nucengdes.2025.113942.
86. Li, X.; Su, X.; Gu, L.; Liu, D.; Wang, G.; Wang, X.; Guo, Y. Investigation on thermo-hydraulic characteristic of lead–bismuth eutectic and supercritical carbon dioxide in a straight-channel printed circuit heat exchanger. *Appl. Therm. Eng.* **2024**, *240*, 122294. https://doi.org/10.1016/j.applthermaleng.2023.122294.
87. Wang, X.; Yang, L.; Xu, B.; Chen, Z. Novel model for heat transfer and flow correlations of precooler, preheater and regenerator in supercritical CO_2 Brayton cycle. *Int. J. Heat Mass Transf.* **2025**, *241*, 126739. https://doi.org/10.1016/j.ijheatmasstransfer.2025.126739.
88. Cheng, J.-Q.; Wang, S.-S.; Li, Q.; Dai, L.; Wang, S.; Wen, Z.-X. Flow and heat transfer behavior of supercritical CO_2 in different PCHE channels under rolling motions. *J. Supercrit. Fluids* **2026**, *227*, 106754. https://doi.org/10.1016/j.supflu.2025.106754.
89. Liu, M.; Liu, S.; Xi, D.; Huang, S.; Huang, Y. Analysis of heat transfer mechanism in supercritical fluids from the aspect of pool heating. *Front. Energy Res.* **2023**, *10*, 1042391. https://doi.org/10.3389/fenrg.2022.1042391.
90. Whitaker, T.A.; Webb, B.P.; Rao, S.R. Microscale heat transfer and phase change mechanisms of carbon dioxide at near-critical conditions. *Int. J. Heat Mass Transf.* **2024**, *235*, 126185. https://doi.org/10.1016/j.ijheatmasstransfer.2024.126185.
91. Wang, Q.; Ma, X.; Xu, J.; Li, M.; Wang, Y. The three-regime-model for pseudo-boiling in supercritical pressure. *Int. J. Heat Mass Transf.* **2021**, *181*, 121875. https://doi.org/10.1016/j.ijheatmasstransfer.2021.121875.
92. Chen, L.; Deng, B.-L.; Zhang, X.-R. Experimental investigation of CO_2 thermosyphon flow and heat transfer in the supercritical region. *Int. J. Heat Mass Transf.* **2013**, *64*, 202–211. https://doi.org/10.1016/j.ijheatmasstransfer.2013.03.077.
93. Longmire, N.; Banuti, D. Onset of heat transfer deterioration caused by pseudo-boiling in CO_2 laminar boundary layers. *Int. J. Heat Mass Transf.* **2022**, *193*, 122957. https://doi.org/10.1016/j.ijheatmasstransfer.2022.122957.
94. Xu, J.; Zhang, H.; Zhu, B.; Xie, J. Critical supercritical-boiling-number to determine the onset of heat transfer deterioration for supercritical fluids. *Sol. Energy* **2020**, *195*, 27–36. https://doi.org/10.1016/j.solener.2019.11.036.
95. Liu, Z.; Wang, M.; Tian, W.; Qiu, S.; Su, G. Flow mixing and heat transfer deterioration investigation of supercritical carbon dioxide in wire-wrapped bundles. *Appl. Therm. Eng.* **2024**, *250*, 123569. https://doi.org/10.1016/j.applthermaleng.2024.123569.
96. Cheng, L.; Xu, J.; Wang, Q.; Dong, X. The influence of tube diameter parameters on the flow resistance and heat transfer characteristics of supercritical CO_2 in horizontal tubes. *Appl. Therm. Eng.* **2024**, *241*, 122361. https://doi.org/10.1016/j.applthermaleng.2024.122361.
97. Fan, Y.; Tang, G. Numerical investigation on heat transfer of supercritical carbon dioxide in a vertical tube under circumferentially non-uniform heating. *Appl. Therm. Eng.* **2018**, *138*, 354–364. https://doi.org/10.1016/j.applthermaleng.2018.04.060.
98. Wang, J.; Guan, Z.; Gurgenci, H.; Hooman, K.; Veeraragavan, A.; Kang, X. Computational investigations of heat transfer to supercritical CO_2 in a large horizontal tube. *Energy Convers. Manag.* **2018**, *157*, 536–548. https://doi.org/10.1016/j.enconman.2017.12.046.

99. Li, X.; Yu, X.; Liu, P.; Fan, Y.; Yang, D.; Tang, G. S-CO_2 flow in vertical tubes of large-diameter: Experimental evaluation and numerical exploration for heat transfer deterioration and prevention. *Int. J. Heat Mass Transf.* **2023**, *216*, 124563. https://doi.org/10.1016/j.ijheatmasstransfer.2023.124563.
100. Zhang, S.; Xiao, C.; Gong, D.; Huo, E. The mechanism and onset boundary of flow instability for supercritical CO_2 heated in vertical single-tube: Experimental study. *Int. Commun. Heat Mass Transf.* **2024**, *152*, 107279. https://doi.org/10.1016/j.icheatmasstransfer.2024.107279.
101. Luo, Q.; Zhou, Y.; Huang, Y.; Huang, J.; Hu, W.; Yuan, Y.; Tang, L. Multi-region oscillation characteristics and hazard of supercritical carbon dioxide in parallel channels natural circulation system. *Energy* **2023**, *267*, 126587. https://doi.org/10.1016/j.energy.2022.126587.
102. Wang, Z.; Liu, X.; He, X.; Chen, Y.; Luo, X. Flow instability of supercritical carbon dioxide in Converging–Diverging tube. *Therm. Sci. Eng. Prog.* **2023**, *40*, 101749. https://doi.org/10.1016/j.tsep.2023.101749.
103. Cai, D.; Xu, X.; Zhang, S.; Liu, C.; Dang, C. Experimental investigation on the flow instability of supercritical CO_2 in vertical upward circular tube in trans-critical CO_2 Rankine system. *Appl. Therm. Eng.* **2021**, *183*, 116139. https://doi.org/10.1016/j.applthermaleng.2020.116139.
104. Zhang, S.; Xiao, C.; Gong, D.; Huo, E. The role of buoyancy and thermal acceleration in heat transfer deterioration and thermal oscillation for the CO_2 around pseudo-critical region. *Int. J. Heat Mass Transf.* **2024**, *218*, 124797. https://doi.org/10.1016/j.ijheatmasstransfer.2023.124797.
105. Emerick, B.S.; Starke, A.R.; da Silva, A.K. Pseudo-transient flow path optimization of a solar tower receiver operating with supercritical carbon dioxide. *Appl. Therm. Eng.* **2024**, *252*, 123472. https://doi.org/10.1016/j.applthermaleng.2024.123472.
106. Huang, J.; Zhou, Y.; Huang, Y.; Luo, Q.; Yuan, Y.; Yang, C.; Hu, W. Experimental study of pressure drop oscillation in a supercritical carbon dioxide natural circulation loop. *Int. J. Heat Mass Transf.* **2024**, *220*, 125005. https://doi.org/10.1016/j.ijheatmasstransfer.2023.125005.
107. Draskic, M.; Nelissen, I.M.; Pecnik, R. Dynamic oscillations in the supercritical carbon dioxide natural circulation loop. *Int. J. Heat Mass Transf.* **2025**, *250*, 127206. https://doi.org/10.1016/j.ijheatmasstransfer.2025.127206.
108. Zhang, Z.; Lu, Z.; Fan, D.; Tang, Y.; Xiang, P.; Wang, J.; Luo, J. Investigation of natural convection flow and heat transfer characteristics of liquid/supercritical CO_2 at constant volume. *Int. Commun. Heat Mass Transf.* **2025**, *164*, 108925. https://doi.org/10.1016/j.icheatmasstransfer.2025.108925.
109. Chen, J.; Han, L.-C.; Chen, H.; Cheng, W.-L. Study on heat transfer characteristics and enhancement mechanism of supercritical carbon dioxide in adaptive channels. *Appl. Therm. Eng.* **2024**, *253*, 123761. https://doi.org/10.1016/j.applthermaleng.2024.123761.
110. Wang, X.; Wang, Y.; Xiao, X.; Chen, Z.; Kang, Y.; Lei, Y. Numerical study on heat transfer deterioration of supercritical CO_2 in lattice structure array channel. *Int. J. Heat Mass Transf.* **2024**, *227*, 125600. https://doi.org/10.1016/j.ijheatmasstransfer.2024.125600.
111. Yan, C.; Xu, J.; Wang, S.; Liu, G. Numerical study of convective heat transfer to supercritical CO_2 in vertical heated tubes. *Int. Commun. Heat Mass Transf.* **2022**, *137*, 106242. https://doi.org/10.1016/j.icheatmasstransfer.2022.106242.
112. Dang, C.; Xu, J.; Tan, X.; Cheng, K.; Qin, J.; Liu, G. Performance analysis and optimization of a novel S-CO_2 closed-Brayton-cycle-based thermal management system for scramjets. *Appl. Therm. Eng.* **2024**, *254*, 123879. https://doi.org/10.1016/j.applthermaleng.2024.123879.
113. Zhang, X.-R.; Chen, L.; Yamaguchi, H. Natural convective flow and heat transfer of supercritical CO_2 in a rectangular circulation loop. *Int. J. Heat Mass Transf.* **2010**, *53*, 4112–4122. https://doi.org/10.1016/j.ijheatmasstransfer.2010.05.031.
114. Zhang, Z.-D.; Wang, K.; Liu, Y.-J.; Li, X.-L.; Fan, Y.-H.; Min, C.-H. Flow and heat transfer performance of supercritical CO_2 compact receivers with cylindrical fins under sidewall heating condition. *Int. Commun. Heat Mass Transf.* **2025**, *167*, 109351. https://doi.org/10.1016/j.icheatmasstransfer.2025.109351.
115. Wang, X.; Xu, B.; Chen, Z. Computational assessment for local and total heat transfer characteristics of supercritical CO_2 in horizontal heated Micro-Channel. *Therm. Sci. Eng. Prog.* **2024**, *49*, 102442. https://doi.org/10.1016/j.tsep.2024.102442.
116. Wang, K.; Hu, Z.-C. Experimental investigation of a novel standing-wave thermoacoustic engine based on PCHE and supercritical CO_2. *Energy* **2023**, *282*, 128334. https://doi.org/10.1016/j.energy.2023.128334.
117. Huang, Z.; Shen, X.; Ouyang, H.; Du, Z. Analysis of non-equilibrium condensation characteristics of supercritical carbon dioxide during transcritical flow in the Laval nozzle. *Int. J. Heat Mass Transf.* **2025**, *236*, 126383. https://doi.org/10.1016/j.ijheatmasstransfer.2024.126383.
118. Xi, W.; Yang, D.; Skripov, P.; Chen, L. Quantitative experiment and numerical simulation on sub-critical and supercritical CO_2-N2 multiphase jet flows. *Int. J. Heat Fluid Flow* **2025**, *114*, 109830. https://doi.org/10.1016/j.ijheatfluidflow.2025.109830.

119. Xiong, C.; Xu, B.; Chen, Z. Flow and thermo-hydrodynamic characteristics in supercritical CO_2 lubrication. *Appl. Therm. Eng.* **2024**, *241*, 122399. https://doi.org/10.1016/j.applthermaleng.2024.122399.
120. Winterton, R.H. Where did the Dittus and Boelter equation come from? *Int. J. Heat Mass Transf.* **1998**. *41*, 809–810.
121. Gnielinski, V. Neue Gleichungen für den Wärme-und den Stoffübergang in turbulent durchströmten Rohren und Kanälen. *Forsch. IM Ingenieurwesen.* **1975**, *41*, 8–16.
122. Jackson, J. Models of heat transfer to fluids at supercritical pressure with influences of buoyancy and acceleration. *Appl. Therm. Eng.* **2017**, *124*, 1481–1491. https://doi.org/10.1016/j.applthermaleng.2017.03.146.
123. Shi, H.-Y.; Li, M.-J.; Wang, W.-Q.; Qiu, Y.; Tao, W.-Q. Heat transfer and friction of molten salt and supercritical CO_2 flowing in an airfoil channel of a printed circuit heat exchanger. *Int. J. Heat Mass Transf.* **2020**, *150*, 119006. https://doi.org/10.1016/j.ijheatmasstransfer.2019.119006.
124. Kim, S.G.; Lee, Y.; Ahn, Y.; Lee, J.I. CFD aided approach to design printed circuit heat exchangers for supercritical CO_2 Brayton cycle application. *Ann. Nucl. Energy* **2016**, *92*, 175–185. https://doi.org/10.1016/j.anucene.2016.01.019.
125. Wen, Z.-X.; Wu, J.-L.; Cao, X.-W.; Cheng, J.-Q.; Wang, S.-S.; Li, Q. Machine learning and prediction study on heat transfer of supercritical CO_2 in pseudo-critical zone. *Appl. Therm. Eng.* **2024**, *243*, 122630. https://doi.org/10.1016/j.applthermaleng.2024.122630.
126. Shi, X.; Liu, Y.; Xue, L.; Chen, W.; Chyu, M.K. Prediction of supercritical CO_2 heat transfer behaviors by combining transfer learning and deep learning based on multi-fidelity data. *Int. J. Heat Mass Transf.* **2024**, *218*, 124802. https://doi.org/10.1016/j.ijheatmasstransfer.2023.124802.
127. Li, H.; Song, M.; Liu, X. Interpretable machine learning-based prediction and analysis of supercritical fluid heat transfer characteristics at different boundary conditions. *Energy* **2024**, *308*, 133035. https://doi.org/10.1016/j.energy.2024.133035.
128. Shao, H.; Qi, P.; Deng, K.; Wang, Y.; Li, C.; Liang, Z.; Zhao, Q. Prediction of supercritical carbon dioxide heat transfer performance under ocean rolling condition based on machine learning methods. *Appl. Therm. Eng.* **2026**, *286*, 129306. https://doi.org/10.1016/j.applthermaleng.2025.129306.
129. Ao, C.; Xu, B.; Wang, X.; Chen, Z. Deep learning driven rapid prediction of supercritical CO_2 flow heat transfer characteristics. *Appl. Therm. Eng.* **2025**, *278*, 127274. https://doi.org/10.1016/j.applthermaleng.2025.127274.
130. Grabowski, O.; Searle, M.; Straub, D. *A Methodology for Simulating Supercritical CO_2 Heat Transfer Experiments Using Machine Learning Models*; National Energy Technology Laboratory (NETL): Pittsburgh, PA, USA, 2024.
131. Bringer, R.P.; Smith, J.M. Heat transfer in the critical region. *AIChE J.* **1957**, *3*, 49–55. https://doi.org/10.1002/aic.690030110.
132. Yoon, S.H.; Kim, J.H.; Hwang, Y.W.; Kim, M.S.; Min, K.; Kim, Y. Heat transfer and pressure drop characteristics during the in-tube cooling process of carbon dioxide in the supercritical region. *Int. J. Refrig.* **2003**, *26*, 857–864. https://doi.org/10.1016/s0140-7007(03)00096-3.
133. Oh, H.-K.; Son, C.-H. New correlation to predict the heat transfer coefficient in-tube cooling of supercritical CO_2 in horizontal macro-tubes. *Exp. Therm. Fluid Sci.* **2010**, *34*, 1230–1241. https://doi.org/10.1016/j.expthermflusci.2010.05.002.
134. Kuang, G.; Ohadi, M.; Dessiatoun, S. Semi-Empirical Correlation of Gas Cooling Heat Transfer of Supercritical Carbon Dioxide in Microchannels. *HVAC&R Res.* **2008**, *14*, 861–870. https://doi.org/10.1080/10789669.2008.10391044.
135. Lee, H.-S.; Kim, H.-J.; Yoon, J.-I.; Choi, K.-H.; Son, C.-H. The cooling heat transfer characteristics of the supercritical CO_2 in micro-fin tube. *Heat Mass Transf.* **2013**, *49*, 173–184. https://doi.org/10.1007/s00231-012-1070-2.
136. Gupta, S.; Saltanov, E.; Mokry, S.J.; Pioro, I.; Trevani, L.; McGillivray, D. Developing empirical heat-transfer correlations for supercritical CO_2 flowing in vertical bare tubes. *Nucl. Eng. Des.* **2012**, *261*, 116–131. https://doi.org/10.1016/j.nucengdes.2013.02.048.
137. Huai, X.; Koyama, S. Heat Transfer Characteristics of Supercritical CO_2 Flow in Small-Channeled Structures. *Exp. Heat Transf.* **2007**, *20*, 19–33. https://doi.org/10.1080/08916150600977424.
138. Kim, H.-Y.; Kim, H.-R.; Kang, D.-J.; Song, J.-H.; Bae, Y.-Y. Experimental Investigations on Heat Transfer to Co_2 flowing Upward in a Narrow Annulus at Supercritical Pressures. *Nucl. Eng. Technol.* **2008**, *40*, 155–162. https://doi.org/10.5516/net.2008.40.2.155.
139. Simões, P.C.; Afonso, B.; Fernandes, J.; Mota, J.P. Static mixers as heat exchangers in supercritical fluid extraction processes. *J. Supercrit. Fluids* **2008**, *43*, 477–483. https://doi.org/10.1016/j.supflu.2007.07.015.
140. Bruch, A.; Bontemps, A.; Colasson, S. Experimental investigation of heat transfer of supercritical carbon dioxide flowing in a cooled vertical tube. *Int. J. Heat Mass Transf.* **2009**, *52*, 2589–2598. https://doi.org/10.1016/j.ijheatmasstransfer.2008.12.021.
141. Liu, Z.-B.; He, Y.-L.; Yang, Y.-F.; Fei, J.-Y. Experimental study on heat transfer and pressure drop of supercritical CO_2 cooled in a large tube. *Appl. Therm. Eng.* **2014**, *70*, 307–315. https://doi.org/10.1016/j.applthermaleng.2014.05.024.

142. Li, H.; Kruizenga, A.; Anderson, M.; Corradini, M.; Luo, Y.; Wang, H.; Li, H. Development of a new forced convection heat transfer correlation for CO_2 in both heating and cooling modes at supercritical pressures. *Int. J. Therm. Sci.* **2011**, *50*, 2430–2442. https://doi.org/10.1016/j.ijthermalsci.2011.07.004.
143. Kim, D.E.; Kim, M.-H. Experimental investigation of heat transfer in vertical upward and downward supercritical CO_2 flow in a circular tube. *Int. J. Heat Fluid Flow* **2011**, *32*, 176–191. https://doi.org/10.1016/j.ijheatfluidflow.2010.09.001.
144. Yoon, S.H.; No, H.C.; Kang, G.B. Assessment of straight, zigzag, S-shape, and airfoil PCHEs for intermediate heat exchangers of HTGRs and SFRs. *Nucl. Eng. Des.* **2014**, *270*, 334–343. https://doi.org/10.1016/j.nucengdes.2014.01.006.
145. Chu, W.-X.; Li, X.-H.; Ma, T.; Chen, Y.-T.; Wang, Q.-W. Study on hydraulic and thermal performance of printed circuit heat transfer surface with distributed airfoil fins. *Appl. Therm. Eng.* **2017**, *114*, 1309–1318. https://doi.org/10.1016/j.applthermaleng.2016.11.187.
146. Pidaparti, S.R.; Anderson, M.H.; Ranjan, D. Experimental investigation of thermal-hydraulic performance of discontinuous fin printed circuit heat exchangers for supercritical CO_2 power cycles. *Exp. Therm. Fluid Sci.* **2019**, *106*, 119–129. https://doi.org/10.1016/j.expthermflusci.2019.04.025.
147. Liu, B.; Lu, M.; Shui, B.; Sun, Y.; Wei, W. Thermal-hydraulic performance analysis of printed circuit heat exchanger precooler in the Brayton cycle for supercritical CO_2 waste heat recovery. *Appl. Energy* **2022**, *305*, 117923. https://doi.org/10.1016/j.apenergy.2021.117923.
148. Saeed, M.; Kim, M.-H. Thermal-hydraulic analysis of sinusoidal fin-based printed circuit heat exchangers for supercritical CO_2 Brayton cycle. *Energy Convers. Manag.* **2019**, *193*, 124–139. https://doi.org/10.1016/j.enconman.2019.04.058.
149. Jing, Q.; Xie, Y.; Zhang, D. Thermal hydraulic performance of printed circuit heat exchanger with various channel configurations and arc ribs for SCO_2 Brayton cycle. *Int. J. Heat Mass Transf.* **2020**, *150*, 119272. https://doi.org/10.1016/j.ijheatmasstransfer.2019.119272.
150. Shiralkar, B.S.; Griffith, P. Deterioration in Heat Transfer to Fluids at Supercritical Pressure and High Heat Fluxes. *J. Heat Transf.* **1969**, *91*, 27–36. https://doi.org/10.1115/1.3580115.
151. Kline, N.; Feuerstein, F.; Tavoularis, S. Onset of heat transfer deterioration in vertical pipe flows of CO_2 at supercritical pressures. *Int. J. Heat Mass Transf.* **2018**, *118*, 1056-1068.
152. Zhu, B.; Xu, J.; Wu, X.; Xie, J.; Li, M. Supercritical "boiling" number, a new parameter to distinguish two regimes of carbon dioxide heat transfer in tubes. *Int. J. Therm. Sci.* **2019**, *136*, 254–266. https://doi.org/10.1016/j.ijthermalsci.2018.10.032.
153. Luo, Z.; Fang, X.; Yang, Y.; Chen, W.; Zhang, L. Prediction of "critical heat flux" for supercritical water and CO_2 flowing upward in vertical heated tubes. *Int. J. Heat Mass Transf.* **2020**, *159*, 120115. https://doi.org/10.1016/j.ijheatmasstransfer.2020.120115.
154. Zhu, X.-J.; Zhang, R.-Z.; Du, X.; Yu, X.; Qiu, Q.-G. Experimental study on heat transfer deterioration of supercritical CO_2 in a round tube:A boundary assessment. *Int. Commun. Heat Mass Transf.* **2022**, 106055. https://doi.org/10.1016/j.icheatmasstransfer.2022.106055.
155. Li, Y.; Xin, G.; Yuan, B.; Zhang, S.; Du, W. Experimental investigation on natural circulation heat transfer of supercritical CO_2 in a closed loop. *Int. J. Heat Mass Transf.* **2023**, *200*, 123503. https://doi.org/10.1016/j.ijheatmasstransfer.2022.123503.
156. Mokry, S.; Pioro, I.; Farah, A.; King, K.; Gupta, S.; Peiman, W.; Kirillov, P. Development of supercritical water heat-transfer correlation for vertical bare tubes. *Nucl. Eng. Des.* **2011**, *241*, 1126–1136. https://doi.org/10.1016/j.nucengdes.2010.06.012.
157. Liao, S.; Zhao, T. An experimental investigation of convection heat transfer to supercritical carbon dioxide in miniature tubes. *Int. J. Heat Mass Transf.* **2002**, *45*, 5025–5034. https://doi.org/10.1016/s0017-9310(02)00206-5.
158. Kim, T.H.; Kwon, J.G.; Park, J.H.; Park, H.S.; Kim, M.H. Heat transfer model for horizontal flows of CO_2 at supercritical pressures in terms of mixed convection. *Int. J. Heat Mass Transf.* **2019**, *131*, 1117–1128. https://doi.org/10.1016/j.ijheatmasstransfer.2018.11.075.
159. Krasnoshchekov, E; Protopopov, V. Heat transfer at supercritical region in flow of carbon dioxide and water in tubes. *Therm. Energy* **1959**, 12, 26–30.
160. Krasnoshchekov, E. Experimental study of heat exchagne in carbon dioxide in the supercritical range at high temperature drops. *High Temp.* **1966**, *4*, 375–382.
161. Jackson, J.; Fewster, J. Forced convection data for supercritical pressure fluids. *Heat Transf. Fluid Flow Serv*, **1975**. 21540.
162. Mokry, S; Pioro, I.L.; Duffey, R. Experimental heat transfer to supercritical CO_2 flowing upward in a bare vertical tube. in Proceedings of $SCCO_2$ Power Cycle Symposium. Troy, NY, USA, 29–30 April 2009.
163. Kim, H.; Bae, Y.Y.; Kim, H.Y.; Song, J.H.; Cho, B.H. Experimental Investigation on the Heat Transfer Characteristics in Upward Flow of Supercritical Carbon Dioxide. *Nucl. Technol.* **2008**, *164*, 119–129. https://doi.org/10.13182/nt08-a4013.

164. Bae, Y.-Y.; Kim, H.-Y. Convective heat transfer to CO_2 at a supercritical pressure flowing vertically upward in tubes and an annular channel. *Exp. Therm. Fluid Sci.* **2009**, *33*, 329–339. https://doi.org/10.1016/j.expthermflusci.2008.10.002.
165. Liu, S.; Huang, Y.; Liu, G.; Wang, J.; Leung, L.K. Improvement of buoyancy and acceleration parameters for forced and mixed convective heat transfer to supercritical fluids flowing in vertical tubes. *Int. J. Heat Mass Transf.* **2017**, *106*, 1144–1156. https://doi.org/10.1016/j.ijheatmasstransfer.2016.10.093.
166. Bishop, A; Sandberg, R.; Tong, L. *Forced-Convection Heat Transfer to Water at Near-Critical Temperatures and Supercritical Pressures*; Westinghouse Electric Corp.: Pittsburgh, PA, USA, 1964.
167. Liao, S.M.; Zhao, T.S. Measurements of Heat Transfer Coefficients From Supercritical Carbon Dioxide Flowing in Horizontal Mini/Micro Channels. *J. Heat Transf.* **2002**, *124*, 413–420. https://doi.org/10.1115/1.1423906.
168. Kruizenga, A.; Li, H.; Anderson, M.; Corradini, M. Supercritical Carbon Dioxide Heat Transfer in Horizontal Semicircular Channels. *J. Heat Transf.* **2012**, *134*, 081802. https://doi.org/10.1115/1.4006108.
169. Filonenko, G. Hydraulic resistance in pipes. *TEPLOENERGETIKA*, **1954**, *1*, 40–44.
170. Petukhov, B.S; Kurganov, V.A.; Ankudinov, V.B. Heat transfer and flow resistance in the turbulent pipe flow of a fluid with near-critical state parameters. *Teplofiz. Vysok. Temp.* **1983**, *21*, 92–100.
171. Fang, X.; Xu, L.; Chen, Y.; Chen, W. Correlations for friction factor of turbulent pipe flow under supercritical pressure: Review and a new correlation. *Prog. Nucl. Energy* **2020**, *118*, 103085. https://doi.org/10.1016/j.pnucene.2019.103085.
172. Zhang, H.; Xu, J.; Zhu, X.; Xie, J.; Li, M.; Zhu, B. The K number, a new analogy criterion number to connect pressure drop and heat transfer of sCO_2 in vertical tubes. *Appl. Therm. Eng.* **2021**, *182*, 116078. https://doi.org/10.1016/j.applthermaleng.2020.116078.
173. Ngo, T.L.; Kato, Y.; Nikitin, K.; Ishizuka, T. Heat transfer and pressure drop correlations of microchannel heat exchangers with S-shaped and zigzag fins for carbon dioxide cycles. *Exp. Therm. Fluid Sci.* **2007**, *32*, 560–570. https://doi.org/10.1016/j.expthermflusci.2007.06.006.
174. Cheng, K.; Zhou, J.; Zhang, H.; Huai, X.; Guo, J. Experimental investigation of thermal-hydraulic characteristics of a printed circuit heat exchanger used as a pre-cooler for the supercritical CO_2 Brayton cycle. *Appl. Therm. Eng.* **2020**, *171*, 115116. https://doi.org/10.1016/j.applthermaleng.2020.115116.
175. Baik, S; Kim, S.G.; Lee, J.; Lee, J.I. Study On CO_2–Water Printed Circuit Heat Exchanger Performance Operating Under Various CO_2 Phases For S-CO_2 Power Cycle Application. *Appl. Therm. Eng.* **2017**, *113*, 1536–1546.
176. Saeed, M.; Berrouk, A.S.; Siddiqui, M.S.; Awais, A.A. Numerical investigation of thermal and hydraulic characteristics of sCO_2-water printed circuit heat exchangers with zigzag channels. *Energy Convers. Manag.* **2020**, *224*, 113375. https://doi.org/10.1016/j.enconman.2020.113375.
177. Meshram, A.; Jaiswal, A.K.; Khivsara, S.D.; Ortega, J.D.; Ho, C.; Bapat, R.; Dutta, P. Modeling and analysis of a printed circuit heat exchanger for supercritical CO_2 power cycle applications. *Appl. Therm. Eng.* **2016**, *109*, 861–870. https://doi.org/10.1016/j.applthermaleng.2016.05.033.

Disclaimer/Publisher's Note: The statements, opinions and data contained in all publications are solely those of the individual author(s) and contributor(s) and not of MDPI and/or the editor(s). MDPI and/or the editor(s) disclaim responsibility for any injury to people or property resulting from any ideas, methods, instructions or products referred to in the content.